Proceedings and Results of the

National Tsunami Hazard Mitigation Program
2015 Tsunami Current Modeling Workshop

February 9 - 10, 2015   Portland, Oregon

Published March, 2017

Listing of Papers Included in Volume:

Preface

By Dmitry Nicolsky and Marie Eble, Co-Chairs NTHMP Mapping and Modeling Subcommittee

Verification and validation of numerical tsunami models is crucial to the production of hazard mitigation and public safety products for maritime and coastal communities. Under the auspices of the National Tsunami Hazard Mitigation Program (NTHMP) Mapping and Modeling Subcommittee (MMS), a currents benchmark modeling workshop was held on 9-10 February, 2015 at the Oregon State Office Building in Portland, Oregon. Participants were tasked with verifying the adequacy of models that were represented. The workshop and resulting proceedings were funded by NOAA through an NTHMP grant to the State of California (NOAA Award Number NA14NWS4670040). As the NTHMP MMS designated agency, the California Geological Survey (CGS) received and managed the grant, the scope of which included documenting benchmarking results and delivering a summary report. The NTHMP MMS acknowledges receipt of the ***Proceedings and Results of the National Tsunami Hazard Mitigation Program 2015 Tsunami Current Benchmark Workshop*** as a deliverable from the CGS under the NOAA NTHMP grant award.

More than one dozen numerical models capable of simulating tsunami-induced currents were represented by participants in the NTHMP Current Modeling Workshop. NTHMP MMS recognizes the time and effort put into this work by each modeling group to generate and compile their respective results, and by Dr. Patrick Lynett of the University of Southern California who served as workshop coordinator. In doing so, Dr. Lynett established benchmark problems, compiled the proceedings, and analyzed then presented individual and ensemble results. As a direct result of these efforts, tsunami modelers now have a better awareness of their ability to accurately capture the physics of tsunami currents and, therefore, have a better understanding of how best to use respective simulation tools for hazard assessment in order to develop products that support mitigation efforts. For the dedication of all involved, NTHMP MMS expresses gratitude and appreciation for the success of the NTHMP Current Modeling Workshop.

The recommendations contained in this report will be considered by the NTHMP MMS such that appropriate improvements and guidelines can be developed for state and federal tsunami modelers to ensure the most consistent and accurate products nationally. Consistent with the findings of the proceedings, potential improvements could include use of only numerical models that address complex and chaotic currents, use of an ensemble modeling approach, and/or expert interpretation and identification of expected areas of dangerous currents (e.g. eddies) not captured by the model results.

Additional modeling results, benchmark problems, and data can be found at the NTHMP MMS web-page as digital appendices to this document.

Summary Report of the NTHMP Current Modeling Workshop

Patrick J. Lynett[a] , Kara Gately[b], Dmitry Nicolsky[c], Rick Wilson[d]
[a] University of Southern California, Tsunami Research Center, Los Angeles, CA 90089
[b] NOAA, National Tsunami Warning Center, Tsunami Research Center, Palmer, AK 99645
[c] University of Alaska, Fairbanks, AK 99775
[d] California Geological Survey, Seismic Hazards Mapping Program - Tsunami Projects, Sacramento CA 95814

Address all correspondence to: Patrick Lynett, University of Southern California, Department of Civil and Environmental Engineering, Los Angeles, CA 90089. Phone: 213-740-3133; email: plynett@usc.edu

1   Introduction and Purpose of the Workshop

To help produce accurate and consistent maritime hazard products, the FY13-17 National Tsunami Hazard Mitigation Program (NTHMP) Strategic Plan includes a requirement of the Mapping and Modeling Subcommittee to also develop and run a benchmarking workshop to evaluate the numerical tsunami modeling of currents. As a result of this 2-day workshop held on March 9 and 10, 2015, in Portland, Oregon, it is anticipated that modelers have a better awareness of their ability to accurately capture the physics of tsunami currents, and therefore a better understanding of how to use these simulation tools for hazard assessment and mitigation efforts.

For this workshop, five different benchmarking datasets were organized. These datasets were selected based on characteristics such as: 1) geometric complexity; 2) currents that are shear/separation driven (and thus are de-coupled from the incident wave forcing); 3) tidal coupling; and 4) interaction with the built environment. While tsunami simulation models have generally been well validated against wave height and runup, comparisons with speed data are much less common. As model results are increasingly being used to estimate or indicate damage to coastal infrastructure, understanding the accuracy and precision of speed predictions becomes increasingly important.

2   Benchmark Problems

2.1 Benchmark Problem #1: Steady Flow over Submerged Obstacle

This experiment is based in Lloyd and Stansby (1997) (L&S). While there are many controlled experimental datasets looking at the wake behind a cylinder, there are very few that examine the wake behind a sloping obstacle in the context of shallow water flow. As the obstacle (the island) remains submerged at all times, the wake is physically generated through a spatially variable bottom stress (i.e. gradients in bottom friction). The aim of this benchmark is to test a model's ability to generate a separation region and the resulting oscillatory wake for an idealized and simplified case.

Test case SB4_02 in the Lloyd and Stansby Part II (L&S) paper is used (See Table 1). The steady discharge velocity is $U = 0.115 \, m/s$, water depth is $h = 0.054 \, m$, and the Reynolds number of the mean flow is $Re = 6210$. The ratio of the water depth to the island height (h/h_i in the L&S paper) = 1.10. The information provided in the Part I paper is used to generate the bathymetry.

4

Specifically, a conical island is placed on a flat bottom, where the water depth is 0.054 m on the flat bottom. The side slopes of the conical island are ~8 degrees, and the ratio of the water depth to the island height (h/h_i in the L&S paper) = 1.10. The height of the island is 0.049 m and the diameter at the base of the island is 0.75 m. The island does not end in a point; the top section of the island is flattened. Figure 1 shows a plot of the described configuration.

Figure 1: Generated bathymetry described by the experiment performed by Lloyd and Stansby (1997) Part I.

For this benchmark, the horizontal components of velocity at two different locations behind the island are compared. Modelers are to provide results for at least three different numerical configurations:

1. Simulation result with dissipation sub-models included, using the roughness information included in the paper to best determine the friction factor. In the paper, the friction factor is estimated to be 0.006 (as a dimensionless pipe-flow-like drag coefficient) or a Mannings n value of 0.01 s/m$^{1/3}$. If a RE-dependent friction factor formulation is employed, then a roughness height, k_s, of ~1.5e^{-6} m should be used.
2. Simulation results with optimized agreement based on tuning of dissipation model coefficients (e.g. friction factor). Note that this simulation can be skipped if the modelers do not wish to optimize their comparisons.
3. Simulation result with all dissipation sub-models not included (e.g. a physically inviscid simulation). The purpose of this test is to understand the relative importance of physical vs numerical dissipation for this class of comparison.

2.2 Benchmark Problem #2: Tsunami Currents in Hilo Harbor

This benchmark is based on a field dataset from the 2011 Japan tsunami in Hilo Harbor, Hawaii. While modelers will of course aim to achieve the best agreement with the measured data, this is not the primary goal of this exercise. The aim of this benchmark is to understand the importance of model resolution and numerics on the prediction of tsunami currents. Some of the questions that modelers tried to answer are:

1. What level of precision can we expect from a model with regard to modeling currents on real bathymetry?
2. Will a model converge with respect to speed predictions and model resolution?
3. What is the variation across different models, using the same wave forcing, resolution, and bottom friction?

To attempt to most clearly answer these questions, this field case will be somewhat idealized, or reduced in complexity, to give the modeling results the best chance of an "apples-to-apples" comparison of shallow water, tsunami currents. For this benchmark, free surface elevation (from tide stations) and velocity information (from the Acoustic Doppler Current Profiler (ADCPs)) are compared. Data for this benchmark test has been provided by Randy LeVeque and Kwok Fai Cheung, who have both examined this location (Arcos and LeVeque (2015) and Cheung et al. (2013)).

Figure 2 shows a plot of the bathymetry data from Hilo Harbor, Hawaii. The data is provided in (lat, long) on a 1/3 arcsec grid. Note that shown on this figure are also the simulation control point (white dot), the two ADCP locations (black dots) and the tidal station (blue dot). As mentioned above, this problem has been "reduced" in an attempt to isolate differences in the employed incident wave forcing. For the bathymetry data, this "reduction" manifests as a flattening of the bathymetry at a depth of 30 meters; in the offshore portion of the bathymetry grid, there are no depths greater than 30 m.

Figure 2: Bathymetry data from Hilo Harbor, Hawaii. Also shown on this figure are the simulation control point (white dot), the two ADCP locations (black dots) and the tidal station (blue dot).

For the incident wave case, modelers are asked to drive their simulations with an offshore *simulated* free surface elevation time series (the "control point"). The location of this time series is (lat, long) = [19.7576, 204.93]. Modelers may force their simulations in whichever way is convenient (e.g. through upper grid boundary, or with an internal source generator in the northern

part of the domain), but should check with their modeled time series at the control point to ensure that they are generating the proper offshore wave condition. Note that the above simplification will lead to a physical mismatch between the simulated and actual data; as the incident wave will vary spatially (albeit weakly) as it approaches the harbor. Modelers are of course encouraged to simulate the complete problem with their models (from source to harbor with nesting), but this is optional.

The first comparison for the free surface elevation case is to check the water surface elevation at the tidal station:

- Hilo Tide Station: [lat, long]=(19.7308, 204.9447)

Modelers may have to shift the simulated and tidal data such that the leading numerical wave arrives at the proper time, and this same time shift has to be used in the velocity comparisons. The official locations of the ADCPs are:

- HA1125, Harbor Entrance: [lat, long] = (19.7452, 204.9180)
- HA1126, Inside Harbor: [lat, long] = (19.7417, 204.9300)

Modelers were requested to provide results for at least three different numerical configurations:

1. Simulation result at ~20 m resolution (2/3 arcsec, de-sample the input bathymetry), using a Mannings n coefficient of 0.025 (or approximate equivalent if using a different bottom stress model)
2. Simulation result at ~10 m (1/3 arcsec) resolution using a Mannings n coefficient of 0.025 (or approximate equivalent if using a different bottom stress model)
3. Simulation result at 5 m resolution (1/6 arcsec, or the lowest resolution possible; use bi-linear interpolation), using a Mannings n coefficient of 0.025 (or approximate equivalent if using a different bottom stress model)

Modelers were encouraged to compare simulation results both locally (required by the benchmark) as well as to examine statistical measures of spatial variability between the different resolutions.

2.3 Benchmark Problem #3: Tsunami Currents in Tauranga Harbor

A field dataset from the 2011 Japan tsunami in Tauranga Harbor, New Zealand (Borrero et al. 2013) is used for this benchmark. The unique component of this benchmark test is to attempt to include the effects of the tides. At the ADCP measurement location, the speed component of the tsunami signal is comparable to the speed of the tidal component, indicating the possibility of a non-linear superposition of the two components. For this benchmark, free surface elevation (from tide stations) and velocity information (from and ADCP) are compared. Figure 3 shows a plot of the bathymetry data from Tauranga Harbor, New Zealand. This dataset has been rotated into longshore and cross-shore coordinates, to facilitate the incident wave forcing along the top domain boundary.

Figure 3: Bathymetry data from Tauranga Harbor, New Zealand.

For the incident wave, modelers were asked to drive their simulations with the most offshore *measured* free surface elevation data. This data location is the ABeacon tide gage. This tide gage is located at the 25 m depth. Three separate time series from this gage were provided to the modelers:

1. Tsunami-only signal. This can be used by modelers who do not wish to include the effects of tides.
2. Tide-only signal. This can be used by modelers to ensure that they are modeling the tides, and the tidally-generating currents, correctly
3. Complete signal. This should be used to drive tsunami+tide simulations

The first comparison will be to check the water surface elevation at the numerous tidal stations. The stations we will focus on here are:

- A Beacon: [lat, long]=(-37.60287, 176.17781); [x, y]= (2.724e4, 1.846e4)
- Tug Berth: [lat, long]=(-37.6407, 176.1809) ; [x, y]= (3.085e4, 1.512e4)
- Sulphur Point: [lat, long]=(-37.6596, 176.1755) ; [x, y]= (2.724e4, 1.846e4)
- Moturiki: [lat, long]=(-37.6307, 176.18377) ; [x, y]= (3.005e4, 1.61e4)

Where the above coordinates are given in geographical coordinates as well as the x-y coordinate system of the rotated bathymetry data, as shown in Figure 3. If modelers choose to not include the tidal component in their simulation, then only the data from water surface elevation for the tsunami-only signal should be compared.

The official location of the ADCP is:

- ADCP: [lat, long] = (-37.6307, 176.18377), [x, y]=(2.925e4, 1.466e4)

However, the actual location varies in time, as the ADCP is chain anchored. Thus, the velocity measurement location likely changes during the tsunami event, with a maximum radius of ~40m around the official location.

2.4 Benchmark Problem #4: Flow through a City Building Layout

This experiment consists of a single long-period wave (NOT a solitary wave) propagating up a piecewise linear slope and onto a small-scale model of the town of Seaside, Oregon. Free surface information was recorded via resistance-type wave gauges and sonic wave gages. Velocity information was recorded via Acoustic Doppler Velocity Meter (ADV's) (Park et al. 2013). For this benchmark, free surface, velocity, and momentum flux information recorded throughout the tank is compared.

Figure 4 shows a plot of the bathymetry data from a small-scale model of Seaside, Oregon. For this experiment the water depth at the wavemaker was 0.97m. The generated wave for this problem is not a solitary wave. It is a custom-made wave meant to maximize the stroke of the wavemaker, while generating a long period wave. Note that due to this generation approach, the wave is not permanent, like a solitary wave. Numerically, the wave can be generated using two different methods:

1. The wavemaker displacement time series can be used if a moving wall boundary condition is available in the numerical model.
2. The time series of incident wave elevation at $X = 5m$ can be used to force the numerical model at $X = 5m$. Note that this is a synthetic time series, based on simulation with a moving wall boundary condition.

Figure 4: Bathymetry data from a small-scale model of the town of Seaside, Oregon.

Data from Wave Gage 3 (WG3) (see Park et al. 2013 for location) was provided to be compared with the numerical model output. Comparisons at this particular location were be used to ensure that the generated waves in the model are correct, in terms of amplitude, period, and arrival time. Overland flow depth, cross-shore (x-direction) velocity, and cross-shore specific momentum flux data comparison is the primary comparison of this benchmark exercise. Here, we compare flow depth (H), velocity (u), and specific momentum flux (Hu^2) at four locations: B1, B4, B6 and B9. These four locations are discussed in depth in the journal article mentioned above.

2.5 Benchmark Problem #5: Solitary Wave Propagation over a Complex Shelf

This experiment consists of a single solitary wave propagating up a triangular shaped shelf with an island feature located at the offshore point of the shelf. Free surface information was recorded via resistance-type wave gauges and sonic wave gages. Velocity information was recorded via ADV's. Note that is the same test case as used during the 2009 Inundation Science & Engineering Cooperative (ISEC) Workshop. For this benchmark, free surface, velocity, and turbulence information recorded throughout the tank are compared.

Figure 5 shows a plot of the bathymetry data from this experiment setup. The water depth at the wave maker is 0.78m and the solitary wave height at the wave maker is 0.39m. Free surface elevation measurements recorded at the following locations are compared with the numerical model output:

1. Recorded at $y = 0$ (centerline of basin) at following x-locations: $X = 7.5m, 13.0m, 21.0m$
2. Recorded at $y = 5.0$ at following x-locations: $X = 7.5m, 13.0m, 21.0m$
3. Recorded at $x = 25$ at following y-locations: $Y = 0.0m, 5.0m, 10.0m$

Figure 5: Bathymetry data from a small-scale model of the town of Seaside, Oregon.

Velocity and turbulence measurements recorded at the following locations are also compared with the numerical model output:

1. Recorded at $x = 13m, y = 0m, z = 0.75m$ (3 cm below still water level). Mean and Root Mean Square (RMS) turbulence fluctuations for the three velocity components are provided.
2. Recorded at $x = 21m, y = 0m, z = 0.77m$ (1 cm below still water level). Mean and RMS turbulence fluctuations for the three velocity components are provided.
3. Recorded at $x = 21m, y = -5m, z = 0.77m$ (1 cm below still water level). Mean and RMS turbulence fluctuations for the three velocity components are provided.

3 Overview of Models Tested

Table 1 presents a list of attendees and their respective models for the 2015 NTHMP currents workshop. To ensure the models being tested captured the basic physics and relative accuracy of currents, benchmark problems #1 and #2 were required of all modelers participating in the workshop. Additional details and references about each model are provided in the individual model chapters included in this report, with the exceptions of the models of Knight (ATFM), Arikawa (CADMAS-SURF), Sampath (Neutrino − SPH), who elected not to contribute to this documentation of the meeting. All presentations are provided as digital files, and can be found here:
http://coastal.usc.edu/currents_workshop/agenda.html. Summary details of each model, such as equations solved and numerical accuracy can also be found in Table 1.

**Table 1. Summary of models presented at the workshop.**

Model Name	Equations Solved [Spatial Dimensions]	Numerical Approach	Numerical Treatment of Convection Terms	Numerical Accuracy of Other Gradient Terms	Numerical Treatment of Time Integration
ALASKA GI'-T	Nonlinear Shallow Water (NSW) [2D]	FD	Upwind (1st-order accurate)	Centered (2nd-order accurate)	Semi-implicit (1st-order accurate)
NAMI DANCE	Nonlinear Shallow Water (NSW) [2D]	FD	Upwind (1st-order accurate)	Centered (2nd-order accurate)	Explicit (2nd-order accurate)
MOST	Nonlinear Shallow Water (NSW) [2D]	FD	Centered (2nd-order accurate)	Centered (2nd-order accurate)	Explicit (1st-order accurate)
Cliffs	Nonlinear Shallow Water (NSW) [2D]	FD	Centered (2nd-order accurate)	Centered (2nd-order accurate)	Explicit (1st-order accurate)
GeoClaw	Nonlinear Shallow Water (NSW) [2D]	FV	Limiter-based (1st-order near shocks, 2nd-order when smooth)	Centered (2nd-order accurate)	Explicit (2nd-order accurate)
GeoClaw -AECOM	Nonlinear Shallow Water (NSW) [2D]	FV	Limiter-based (1st-order near shocks, 2nd-order when smooth)	Centered (2nd-order accurate)	Explicit (2nd-order accurate)
Tsunami-HySEA	Nonlinear Shallow Water (NSW) [2D]	FV	Limiter-based (2nd-order near shocks, 3rd-order when smooth)	Centered (2nd-order accurate)	Explicit (3rd-order accurate)
pCOULWAVE	Highly Nonlinear Boussinesq-type [2D]	FV	Limiter-based (2nd-order near shocks, 4th-order when smooth)	Centered (4th-order accurate)	Semi-implicit (4th-order accurate)
FUNWAVE-TVD	Highly Nonlinear Boussinesq-type [2D]	FV / FD	Limiter-based (2nd-order near shocks, 5th-order when smooth)	Centered (4th-order accurate)	Explicit (3rd-order accurate)
BOSZ	Weakly Nonlinear Boussinesq-type [2D]	FV	Limiter-based (2nd-order near shocks, 5th-order when smooth)	Centered (5th-order accurate)	Explicit (2nd-order accurate)
NEOWAVE	One-Layer, Non-Hydrostatic [2D]	FD	Upwind (1st-order near shocks, 2nd-order when smooth)	Centered (2nd-order accurate)	Semi-implicit (2nd-order accurate)
TSUNAMI3D	Navier-Stokes [3D]	FD	Upwind (1st-order accurate)	Centered (2nd-order accurate)	Explicit (2nd-order accurate)
SCHISM	Navier-Stokes, Hydrostatic [3D]	FE / FV	Limiter-based (1st-order near shocks, 2nd-order when smooth)	Centered (2nd-order accurate)	Semi-implicit (2nd-order accurate)

Note that in the "Numerical Approach" column, FD= Finite Difference, FV=Finite Volume, FE=Finite Element

4   Inter-comparison of Model Results

4.1 Benchmark Problem #1: Steady Flow over Submerged Obstacle

As mentioned in the background section above, modelers were requested to simulate BM#1 using a number of different dissipation (bottom friction) models. The desired outcome from these simulations is the prediction of a vortex sheet in the lee of the obstacle, with similar shedding frequency and eddy strength as observed in the experiments. An example of the numerical results and experimental data is provided in Figure 6.
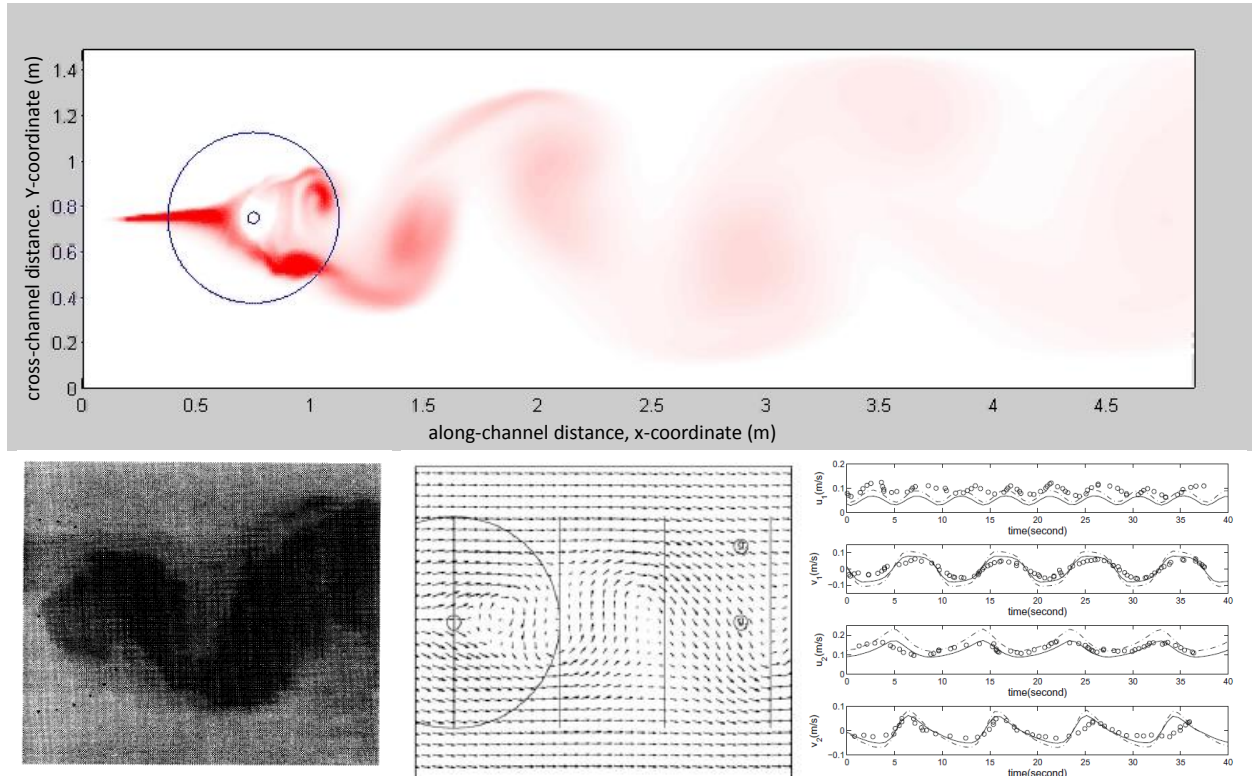
Figure 6: Summary of numerical and experimental data from BM#1: top plot shows a numerical simulation including scalar dye transport to visualize the vortex sheet; lower left plot is a dye visualization from the experiment; lower middle plot shows the PIV-extracted surface velocity field from the experiment as well as the location of the two time series to be compared by the models; lower right plot shows the experimental data at the two time series locations (dots) as well as example numerical predictions (lines).

In general, simulations with all bottom friction turned off generated a chaotic and irregular vortex sheet, with very little resemblance to the experimental results. This is a reasonable and expected outcome; as the generation of the vortex sheet and properties of the wake are strongly dependent on the interplay between bottom stress and the inertia of the flow, and poor description of the bottom stress should lead to a poor description of the resulting wake. Thus, the focus of discussion here will be on the numerical results provided with the "optimum" bottom friction coefficient, where here "optimum" is a subjective term with definition left to the discretion of the modeler. Indeed, it is expected that different modelers expended different levels of effort to achieve what they perceived to be the best agreement with the experimental data. Furthermore, the measures to

be discussed in this section, used to assess model accuracy, were not provided to the modelers prior to their submission of "optimum" results.

A summary of the model resolutions and dissipation models used by all the modelers is given in Table 2. The minimum spatial resolutions found in the results are typically near 1 cm, with values as high as 2.5 cm. Clearly, the most common submodel used to approximate bottom stress is the Mannings equation. While the recommended Mannings "n", as provided in the original experimental papers, is $0.01 \text{ s/m}^{1/3}$, the majority of modelers found that a larger friction coefficient was required. The most common and median "n" value found in the results is $0.015 \text{ s/m}^{1/3}$ and employed values ranged from $0.01\text{-}0.02 \text{ s/m}^{1/3}$. With the expectation that the strength of numerical dissipation is proportional to the grid resolution (i.e. the finer the grid, the smaller the numerical dissipation – of course this is strongly dependent on the numerical scheme), it is possible that, in a statistical sense, relatively small friction factors might be associated with relatively coarse grid sizes. Put more simply, physical dissipation plays a larger role as numerical dissipation plays a smaller one. Looking at the modeling results that used the Mannings equation for bottom friction, assessment of this potential trend is straightforward. While there is a correlation between grid size and Mannings "n", it is very weak (R^2=0.08). Thus, when comparing the different modeling results, variable numerical dissipation due to different grid resolutions is a second-order effect.

Other than the Mannings equation for bottom friction, four modelers used a traditional quadratic friction law. Among those four results, three used a constant friction factor and one used a characteristic roughness height. When using a roughness height approach, the local friction factor is dependent on the local Reynolds number, and is therefore both temporally and spatially variable. For those using a constant friction factor, values ranged from 0.006-0.012; the recommended friction factor as provided in the original experimental papers is 0.006. For the single model which used a roughness height, friction factors ranged from 0.004-0.012 during the simulation.

In addition to dissipation through bottom friction, a few modelers also included dissipation through various horizontal and vertical eddy viscosity models. Due to the limited usage of such approaches within the models tested, and a lack of similar dissipation models used, the sensitivity and effect of such models will not be addressed here. In summary, we have a comprehensive set of numerical models used by the international tsunami community, with various physical and numerical properties. Next, we seek to understand how these various properties are related to model accuracy, and try to identify which of these properties are most relevant to accurate model of complex, tsunami-induced coastal currents.

Table 2. Summary of numerical and physical parameters used for the BM#1 simulations.

Model Name	Spatial Grid Size (m)	Bottom Stress Model	Bottom Stress Parameter	Other Turbulence Closure Models Used
ALASKA GI'-T	0.01	Manning Friction Coefficient	$n=0.012$ s/m$^{1/3}$	
NAMI DANCE	0.01	Manning Friction Coefficient	$n=0.010$ s/m$^{1/3}$	
MOST	0.01	Manning Friction Coefficient	on bottom, $n=0.010$ s/m$^{1/3}$ on island, $n=0.017$ s/m$^{1/3}$	
Cliffs	0.025	Manning Friction Coefficient	$n=0.015$ s/m$^{1/3}$	
GeoClaw	variable, from 0.01-0.076	Manning Friction Coefficient	on bottom, $n=0.000$ s/m$^{1/3}$ on island, $n=0.015$ s/m$^{1/3}$	
GeoClaw -AECOM	0.0076	Manning Friction Coefficient	on bottom, $n=0.000$ s/m$^{1/3}$ on island, $n=0.015$ s/m$^{1/3}$	
Tsunami-HySEA	0.0152	Quadratic Drag Friction Law	$C_D=0.006$	
pCOULWAVE	0.015	Roughness height model to determine C_D based on Moody Diagram, Quadratic Drag Friction Law	$k_S=0.015$ mm (C_D varies from 0.004 to 0.012 during simulation, function of Reynolds Number)	Smagorinsky model for horizontal mixing, Elder's model for vertical mixing, and backscatter model
FUNWAVE-TVD	0.01	Quadratic Drag Friction Law	$C_D=0.012$	
BOSZ	0.015	Manning Friction Coefficient	$n=0.020$ s/m$^{1/3}$	
NEOWAVE	0.01	Manning Friction Coefficient	$n=0.010$ s/m$^{1/3}$	
TSUNAMI3D	0.01 in x 0.0027 in z	No bottom stress sub-model used, no-slip boundary condition employed, numerically resolved boundary shear	Not applicable	kinematic viscosity = 1×10^{-6} m^2/s
SCHISM	0.012	Quadratic Drag Friction Law	$C_D=0.006$	k-ε turbulence closure scheme

As a reminder, the experimental data used to compare these models consists of horizontal velocity component time series at two locations; thus there are four separate time series to examine. To understand each model's ability to recreate the experimental data, two primary measures will be used. First, the magnitude of the fluctuation of the each component will be analyzed. To calculate this fluctuation, a zero-crossing technique is employed to first identify each of the individual oscillations in a de-meaned time series. For each oscillation, or segment of the time series between two successive zero-up crossing locations, the total fluctuation (or height) is calculated. Thus, for each time series, we have a set of fluctuations, and a mean fluctuation and a standard deviation of the fluctuations is determined. To interpret these statistical values, the mean fluctuation represents the "best estimate" from the time series while the standard deviation provides a measure of the chaotic nature of the flow.

When performing these calculations on the experimental data, it is found that this data has a significant standard deviation, on the order of 10-20% of the mean fluctuation value. This implies that variation in eddy strength during shedding is indeed a physical property of this flow and bathymetry configuration. It is expected that these physical variations are due to small perturbations in the inlet flow profile and irregularities in the bathymetry, leading to small asymmetries in the shear layers around the obstacle, and finally creating relatively large changes in the wake immediately behind the obstacle. We note this here because the large majority of the models used during this exercise do not include any perturbations in the inlet flow or bathymetrical profile. Therefore any standard deviation of fluctuation found in the modeling results, and indeed the initial development of the vortex sheet itself, must be driven by numerical errors or gridding asymmetries. Among the models tested here, there was a wide variation in the time required to develop a vortex street, and this is likewise due to differences in numerical errors and gridding. To overcome this physical disconnect, a model might introduce random, small bathymetry perturbations, include a backscatter model, or use a turbulence closure model that requires some initial random seeding of turbulence. Finally, however, we remark that with geophysical scale simulations using measured bathymetry, the natural variability in bathymetry would likely introduce spatial perturbations in the flow sufficient to initiate vortex street-like instabilities.

Figure 7 shows the modeled velocity component fluctuations scaled by the respective experimental values. While there are a couple large-error outliers for each velocity component comparison, most models provide agreement with the experimental mean fluctuations to within 50% for all components. On the other hand, few models, less than 1/3 of the group, yield an error of 25% for each component, and only half of these models are accurate to within 10%. Also shown in this figure is the standard deviation of the fluctuations, for both the data (given by the horizontal dashed lines) and the models (given by the vertical solid lines). Looking at the data, it is evident that all velocity components, except the V-component at time series location#1, exhibit standard deviations of 15% of the mean fluctuation. To interpret the modeled accuracy of the standard deviation, the vertical length of the modeled deviation should be equal to the vertical distance between the data deviations (vertical distance between the dashed lines). While it is noted that no specific measure of standard deviation accuracy is provided here, it is quite clear that there is little skill in capturing this parameter amongst the models tested. However, this is arguably reasonable, as only two of the models (Model#8 with a backscatter model and Model#13 with a k-ε turbulence closure) contain physics that might permit prediction of such a statistic.

16

To summarize the data presented in Figure 7, the error for each model, averaged across the four velocity component time series, is shown in Figure 8. Also shown in this figure is the summary standard deviation, also averaged across the four time series. In the bottom plot of Figure 8 are shown the same statistical values for the time period of oscillation (i.e. the length of time between two successive zero-crossings). Clearly, there are models which perform substantially better than others in the measure for this benchmark, and model accuracy appears to be related to model complexity, where we consider complexity to be related to both numerical scheme and the physics included in the model equations. To this end, three model classes are defined:

- Class I: Models solving the nonlinear shallow water wave equations, with all types of numerical approaches; the first seven models listed in Table 1: ALASKA GI'-T, NAMI DANCE, MOST, Cliffs, GeoClaw, GeoClaw-AECOM, and Tsunami-HySEA
- Class II: Models solving a set of weakly dispersive equations using an analytical solution to the vertical kinematics, with all types of numerical approaches; Models pCOULWAVE, FUNWAVE-TCD, and BOSZ
- Class III: Models solving a set of equations where the vertical structure of the flow is not specified a-priori and can be hydrostatic or non-hydrostatic with respect to gravity waves, with all types of numerical approaches; Models NEOWAVE, TSUNAMI3D, and SCHISM

The average model accuracy in each of these "Classes" will now be examined. It is emphasized that the conclusions drawn by comparing these groups of models may not pertain to any individual model.

For Class I models tested here, the mean error in predicted fluctuation, averaged across the four time series, is 42%. Interestingly, the Class I mean standard deviation of the fluctuation is very close to the observed value; however, none of the models in this group contain the physics to capture this phenomenon, and thus this is a fortuitous numerical error. The error in predicted fluctuation in the Class II models is 45% of that found in Class I, and therefore there is clearly an accuracy gain when moving from Class I to Class II, for this benchmark, within the tested models. Moving to the last group, Class III, there is again a reduction in the error of 22% from Class II and 57% from Class I. In the model-averaged sense, neither Class II nor Class III yields a reasonable prediction of the standard deviation of the fluctuation.

Examining the error in the shedding period, shown in the lower plot in Figure 8, similar conclusions can be drawn. There is a clear decrease in error when moving from Class I to Class II models; however Class II and Class III models perform similarly. Additionally, the errors seen in this shedding period analysis are considerably less than those in the speed analysis, in the relative sense. This conclusion would imply that, for this flow and obstacle configuration, the effect of bottom roughness impacts the strength of the eddies to a greater degree than it impacts the shedding frequency. We reiterate that while the above inter-Class comparisons are valid, there exist individual model violations of these comparisons, where, for example certain Class I models perform better than Class II or Class III models. Thus, the conclusions draw here are meant to represent the abilities of the tsunami modeling community as a whole, as all of the models used in the exercise are currently used for operational, planning, and/or research applications.

Figure 7: Data-scaled modeled mean fluctuation (blue dots) and standard deviation of fluctuation (vertical black lines) for each model for U at location #1 (a), V at location#1 (b), U at location #2 (c), V at location#2 (d). The red-dashed horizontal lines show the standard deviation in the data.
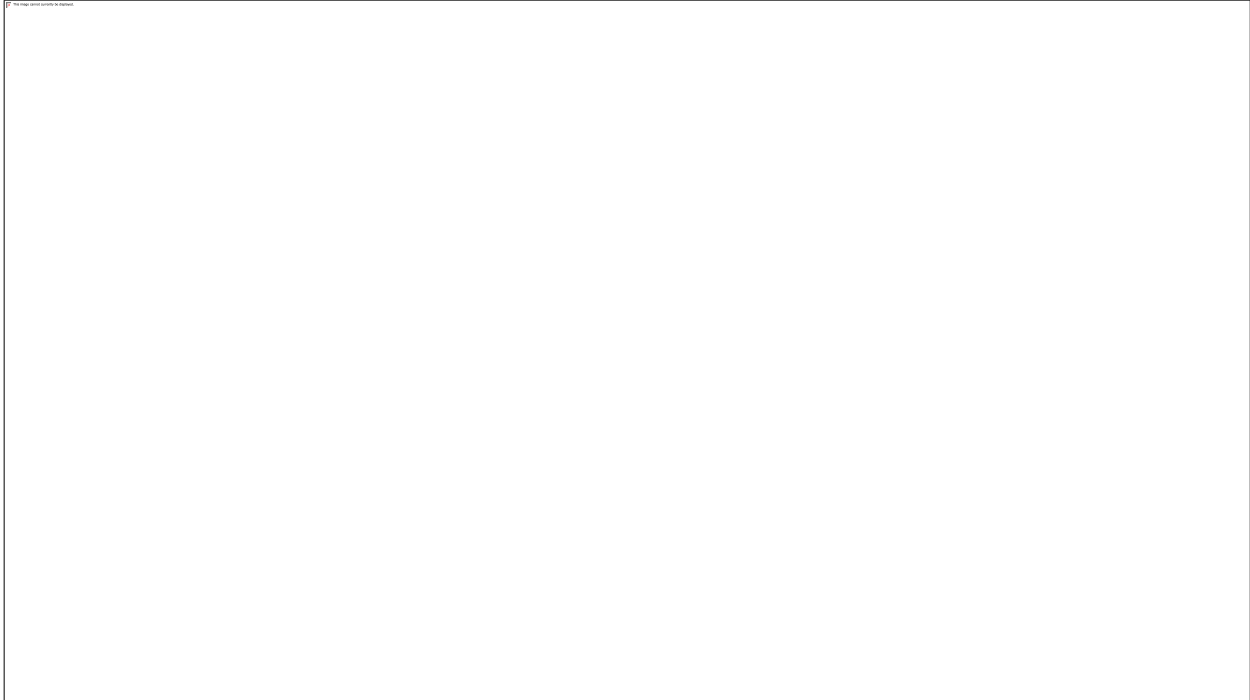
Figure 8: Error in component-averaged modeled velocity, as a fraction of the experimental value, for the mean fluctuation (top) and period of oscillation (bottom). The data is presented in the same format as Figure 7.

While using the fluctuation of speed components provides a method to assess a model's ability to predict the total range of speed, it does not necessarily assist in the understanding of whether a model is providing an accurate prediction of the kinetic energy of the flow, which may be more relevant for estimating hydrodynamic forces. To this end, we seek a statistical measure proportional to the square of the velocity. A time-averaged velocity squared, determined for each of the four velocity time series components, is calculated and plotted in Figure 9. What is immediately obvious from these comparisons is that the fraction errors here and considerably larger than those found in the previous comparison. At both locations, all models tend to under predict the U-components and all but two models over-predict the V-components. Such a broad and consistent trend in model errors either implies that there is an inconsistency between the experimental and numerical parameters (e.g. incorrect location or different upstream boundary conditions) or a fundamental deficiency in the numerical models examined here. While the former possibility may be statistically justified (due to the large majority of models showing this strong bias), the realization that one of the fully-3D models (Model 13) provides an high accuracy prediction of all four of these component-square values provides a strong argument to the latter possibility.

It is reiterated here that the modeled errors in these quantities for most of the models are large, with the exception of the U_2^2 component, for which most models are within 30% accuracy (all under-predict). More than half of the models under-predict U_1^2 by 75%, 10 of the 13 models over-predict V_1^2 by 100% including three that over-predict by 200%, and 6 of the 13 models over-predict V_2^2 by 50%. The implications of such errors are particularly significant when one considers on-going attempts to use model results to estimate drag-like loads on structures. In these studies, both the magnitude and direction of the speed is important.

The average of these errors in the four components is provided in Figure 10 for each model. Only two models provide an average error in the component speed squared of less than 50%. The majority of models have an error between 50% and 100%, and there is a high-error outlier with an averaged error of 200%. Clearly, the models included here, with only a couple exceptions, struggle with this comparison, indicating that great care must be taken when trying to utilize model results for force estimations. Discussion within the tsunami community is required in order to justify some level of "required accuracy" in order for a specific model to be used in structural loading calculations. For example, setting an accuracy requirement of 100% (or 1.0 in Figure 10) would be inclusive, but a threshold this large and the associated safety-factors (or similar conservatism) that would be needed to reliably use the model output may regularly lead to over-design. On the other hand, specifying an accuracy requirement of 25% might reduce the need to add large safety factors, but would also imply only one of the tested models is acceptable. Since specification of an accuracy requirement based on the number of models that presently met the requirement is illogical, the tsunami community, with input from other engineers who would use the output for structural design, should decide on a target accuracy for BM#1 comparisons. Models should be able to meet this target accuracy, while also demonstrating numerical convergence with the use of a reasonable bottom friction coefficient.

Figure 9: Data-scaled modeled time-averaged speed squared (blue dots) and the square of the modeled mean speed (smaller green dots) for each model for U at location #1 (a), V at location#1 (b), U at location #2 (c), V at location#2 (d). The red horizontal line in each plot is data line (where, ideally, the blue dots would align), and the green horizontal dashed line is the square of the experimental mean speed (where, ideally, the green dots would align).

Figure 10: Error in component-averaged modeled velocity squared, as a fraction of the experimental value.

4.2 Benchmark Problem #2: Tsunami Currents in Hilo Harbor

While the instrumentation observations in Hilo Harbor during the 2011 tsunami make this location unique in its number of closely located measurements, it is still difficult to use this case as a benchmark for demonstrating model accuracy. The reasons for this are two-fold. First, the ADCP time series data is sampled every six minutes, and every data point represents a six-minute average of the vertical profile of the current. The velocity field under a tsunami, particularly inside a harbor, can change quickly with studies suggesting that a sample rate of a minute is necessary to resolve nearshore currents (e.g. Lynett et al., 2012); potentially sub-minute if the flow is effected by eddies. Thus, there exists averaging-driven imprecision and possibly significant aliasing in the Hilo ADCP measurements due to the relatively coarse, discrete sampling; this effect is potentially much more significant, in a relative sense, than errors found in tide gage data and even runup measurements. Secondly, and with the ADCP imprecision in mind, this is a field-data case for which the initial condition and propagation over half of the Pacific includes uncertainty and error. Combining the far-field uncertainty and relatively large near-field imprecision leads to a situation where quantitative accuracy measures, as would be needed for a rigorous benchmark, become meaningless. This is a remarkable statement in light of the fact that Hilo Harbor is, as mentioned, possibly the best instrumented location for tsunami-induced currents, and therefore implies higher resolution sampling of nearshore tsunami-induced currents is a great need.

The comparisons presented in this section will be divided into two parts: first, analysis of time series measurements at the tide gage and ADCP locations will be presented, followed by an examination of the spatial properties of the model output. Direct inter-model comparisons with

time series data is difficult. The reason for this is that, typically, after the first few waves, model differences begin to accumulate, often taking the form of apparent phase errors. For example, two models may predict similar wave shapes, but with arrival time differences of minutes. With existing data and models, it is generally impossible to operationally predict precise arrival times of crests after the leading waves, due to model and data errors. For this reason, the time series comparisons presented here will focus on the envelope, where the envelope is defined as the line that connects the individual crests (or troughs) in the measured or modeled time series. Here, for the tide gage elevation data, a crest is defined as the maximum elevation of a discrete "wave", where a wave is defined as the data between two successive zero-up crossings.

Figure 10 provides a summary of the inter-model and model-data comparisons for the tide gage. Not that for this and all comparisons in this section, no individual models are directly compared with the data; only the inter-model means are shown with data. The top panel of Figure 10 shows each model-predicted ocean surface elevation time series, as well as the mean envelopes of crest and trough elevation. The middle plot again shows these modeled mean envelopes, but also shows the corresponding values from the tide gage. Note that there is a gap in the data starting near 10.3 hours after the earthquake; the gage did not function properly during this time. In the lower plot, the inter-model standard deviation and the model-mean accuracy in the crest envelope are summarized, as a function of time. Both are provided in relative terms, where the model deviation is scaled by the model-mean envelope, and the model error is scaled by the tide gage envelope. Examining the trend in inter-model standard deviation, we see that for the first four wave crests, the standard deviation remains low, shifting between 20-30% of the mean. After this time, however, the variation grows and fluctuates between 30-80% for the remainder of the time series. Trends in the mean-model error do not exhibit any clear temporal behavior, and are characterized by large (80%) errors both early and late in the examined time series. In a time-averaged sense, both the relative inter-model standard deviation and the mean model error have similar values of 20% during the first hour of the event, and then grow to 40% during the next three hours. These values may represent a precision threshold, and could be used to interpret potential errors in, for example, real-time model results.

In the same format as the elevations shown in Figure 10, Figure 11 provides a summary of the velocity time series comparisons measured at the ADCP locations HA25 (entrance channel) and HA26 (inside breakwater). To match the sampling method of the ADCP's, the numerical time series are filtered using a 6-minute moving average. The individual times series from all the models are given in the top panels in Figure 11, as well as the model-mean envelope from these results. From the individual model time series, we see that there is inter-model phase agreement for the first three or four speed peaks, but after this, phase correlation degrades quickly. This observation is in contrast with the modeled elevation time series shown in Figure 10, where inter-model phase correlation persists for the 4.5 hours of time displayed. The inter-model mean envelopes are shown in the middle plots with the ADCP envelope, and errors and inter-model variations are given in the bottom plots. First, looking at the intermodal variation, it is clear that this measure has a similar behavior with comparable values at the two locations, starting at a relatively low 20-30% for the first hour, and then exhibiting a general trend of increase, but with values jumping between 20-100%. Throughout the event, the inter-model standard deviation in the speed envelope is between 0.1-0.3 m/s; this is an impressively low value in the context of

predicted current speeds, and indicates that an ensemble-based speed envelope may be a stable statistic.

From the model error curves, a counter-intuitive result of large errors at HA25 and relatively small errors at HA26 is found. At HA25, there are a number of times when the model-mean speed envelope predicts a speed greater than twice the measured value, as seen by model errors of 1.0 or greater in Figure 11. At HA26 on the other hand, for much of the compared record, the model error remains below 50% and is quite comparable to the inter-model variation. This is somewhat unexpected as the location of HA26 near to the tip of the harbor breakwater is more likely to be affected by eddies, to be discussed in more detail later, which should make for a much more challenging model-data comparison. However, as mentioned earlier, the model error should not be considered a significant comparison, due to the imprecision in the velocity data. With that said, maximum absolute errors in the mean-model envelope are near 0.5 m/s throughout the event, and thus this value may be interpreted as an ensemble-based model velocity accuracy for advisory level events.

While time series comparisons are useful for understanding how errors and variations evolve temporally, they do not assist in the understanding of how quickly flow properties change spatially. To examine spatial variability, we use maximum predicted speed surfaces from each of the numerical models. Each surface provides the maximum speed predicted at each grid point throughout the simulation. Figure 12a) gives the inter-model mean maximum speed surface; to create this surface, each of the individual model surfaces is interpolated to the same spatial grid, and then the mean value at each point is determined from the stack of model surfaces. The greatest speeds are found in the area near to the tip of the breakwater, and along the coast where the depths are shallow; in these areas the model mean speeds are in excess of 4 m/s.

With the stack of individual model surfaces, the inter-model standard deviation of maximum speed can also be calculated at each grid point. These values are shown in Figure 12 b). The largest standard deviations are also seen near the tip of the breakwater, and are associated with eddies of different strength taking different paths in the different models. The area affected by eddies is very clear with this statistic. The maximum deviations in the eddy area are near 2 m/s, and represent 50-150% of the model-mean speed. This model comparison indicates that it is reasonable to expect large differences between models in areas affected by eddies, and thus velocity predictions from any single model in such locations must be carefully and conservatively interpreted. Statistically, the large inter-model deviations imply that individual models are unreliable, and ensemble means of the maximum speeds are strongly preferred.

There are two additional important observations from the speed deviation in Figure 12b). First, in areas not affected by eddies, the models show excellent convergence with inter-model standard deviations less than 0.2 m/s, often representing 10-20% of the mean speed. Thus, where currents are coupled with the wave (and not de-coupled in the form of eddies), models converge precisely. Second, deviations along the immediate shoreline and in areas of inundation are large. While not the focus of this study, this observation points out that speed predictions for overland flow, among the models tested here, are highly divergent. As model predictions for overland flow speed are being increasingly used for structural loading calculations, additional study is needed to quantify errors and variability in inundation velocities.

The properties of a modeled eddy (e.g. tangential speed, radial speed gradient) are dependent on the magnitude of the shear in the eddy generation area, or separation area. Numerically, this shear magnitude may be limited by the numerical resolution, as relatively coarse resolutions are unable to resolve strong velocity gradients. Thus, there may be a strong connection between the numerical signature of an eddy and the numerical resolution. Figures 12 c-e) show the relative inter-model deviations, scaled by the inter-model mean speed, for three different resolutions. Clearly, the speed deviations grow with decreasing resolution. The reason for this appears to be that, as resolution decreases, models have a tendency to generate eddies with a larger radial velocity gradient. A larger radial velocity gradient equates to rapid spatial changes in fluid speed, and increased sensitivity to the precise path of the eddy. A troublesome conclusion for modeling follows: in eddy areas, many models will increasingly diverge with decreasing resolution, at least through the horizontal resolutions tested here (down to 5 m). A clear example of how this divergence may manifest is shown in Figure 13. This figure provides vertical vorticity snapshots at the same time from the same numerical model, but using two different resolutions. The eddies in the finer resolution snapshot appear smaller with stronger vorticity, in line with the discussion above. Also, the large eddy located in the harbor entrance takes two different paths in the two simulations. In the 10-m resolution simulation, the eddy passes through the HA25 ADCP location, but in the 5-m simulation the eddy stays to the south of the ADCP. This is an example of the trouble with in-situ point measurements of tsunami currents in areas with eddies, and is another argument for the use of ensemble means for speed predictions, based on many realizations of potential eddies.

An alternative to multi-model or multi-realization ensembles is to spatially average the output from a single model, i.e. attempt to average out the local impact of an eddy. Such an approach would have the disadvantage of smoothing peak speeds associated with an eddy, but might provide numerically convergent results with a single model. Figure 14 displays an attempt at spatial averaging. Here, we spatially average across two lengthscales: (1) an "eddy scale" which here is estimated to be 100 m based on simulation output and (2) ten times the "eddy scale" or 1 km. A box with side length equal to the lengthscales are used for the averaging area, and are shown in the top plot of Figure 14. The box-average maximum speed for each of the individual models are plotted for both box sizes. For each model, the box-average for the 20-m and 10-m resolutions are shown, scaled by the box-average from the 5-m resolution result. Thus, if the 10-m (or 20-m) resolution box-average has numerically converged, it would plot at 1.0 along the vertical scale. Clearly, using the "eddy scale" as the averaging lengthscale does not lead to a set of models that demonstrates convergence at 10-m resolution. It is not until one uses a much larger averaging lengthscale, here 1 km, that we see broad convergence across the tested models at 10-m resolution. Averaging model speed predictions over a 1 km^2 area, while suitable for demonstrating a form of individual model convergence, yields output of very limited use for hazard assessment, where local maximum might govern hazardous conditions and damage potential.

Following the analysis above, an ensemble mean of maximum speed is likely to be the most robust and informative modeling product, with significant and decision-impacting benefits over single model, deterministic predictions. The ensemble produced in this paper used many different models; however it is certainly possible to generate a spectrum of realizations with a single numerical model using a distribution of perturbations to initial conditions, bathymetry, bottom

roughness, etc. Some research would be needed to specify an appropriate set of perturbations. If an ensemble was available, it is not obvious what the most useful way to present the statistical information would be. Certainly means and deviations could be provided, but this might require expert-level judgement to use in decision making. An alternative would be a "threshold map", and example of which is shown in Figure 15. This map provides the "chance" that any location might experience a maximum current greater than a set threshold (the threshold is 2 m/s in Figure 15). The "chance" is based on how many of the models in the ensemble predict a speed greater than the threshold. The advantage of such a map is that if provides both a speed magnitude and confidence together allowing for discussions of risk informed decisions.
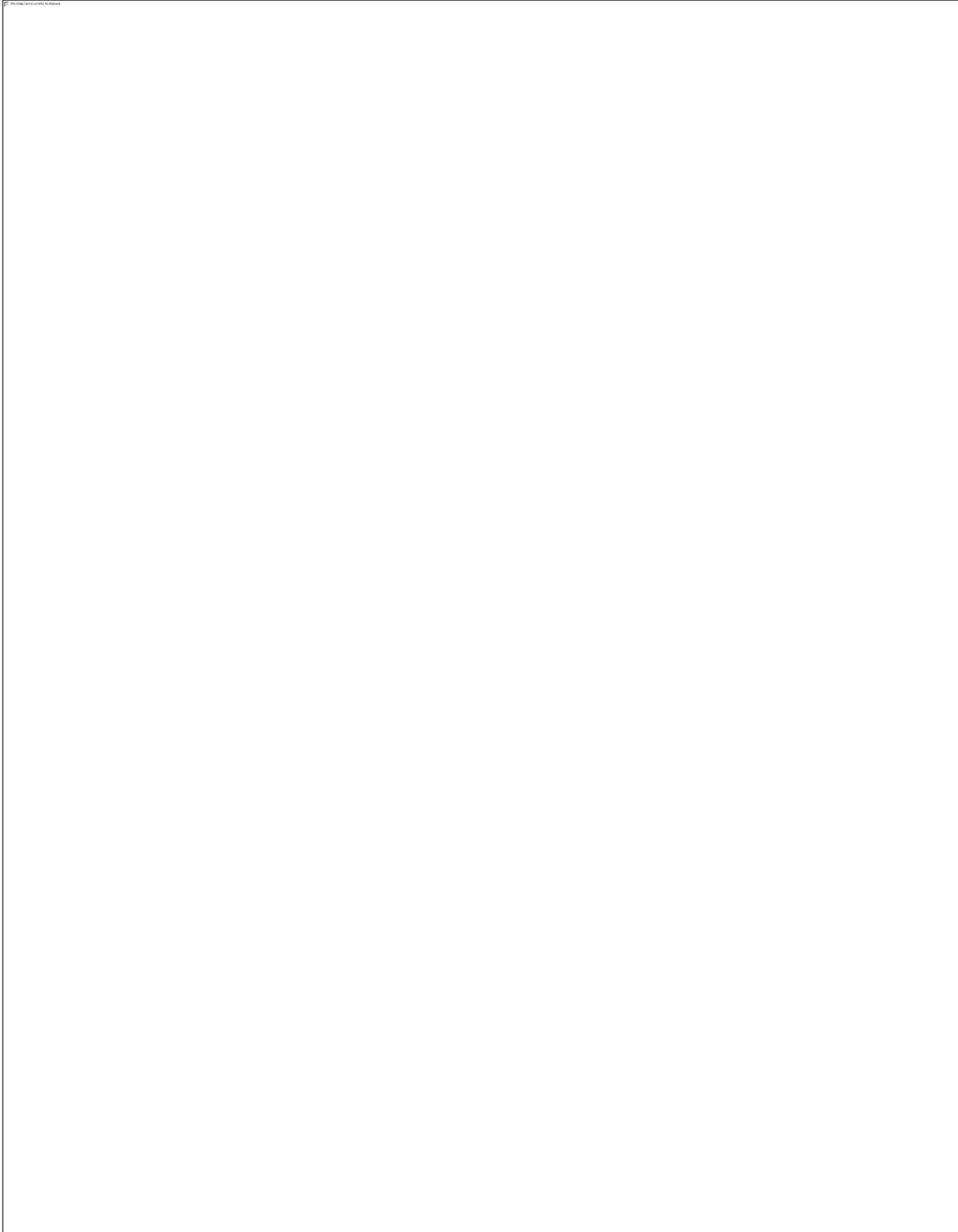
Figure 10: Inter-model variability and error for ocean surface elevation measured at the tide gage location. Top plot a): Predictions from all models (thin solid lines), inter-model mean crest envelope (thick solid line), and inter-model mean trough envelope (thick dashed line). Middle plot b): Comparison of inter-model envelope to measured tide station data envelope; also shown in the time series from the measured data. Bottom plot c): mean inter-model error (solid line) and intermodal standard deviation (dashed line) for the crest envelope.

Figure 11: Inter-model variability and error for ocean current speed measured at the ADPC location HA25 (left column) and HA26 (right column). Top row plots a) and b): Predictions from all models (thin solid lines) and inter-model mean speed envelope (thick solid line). Middle row plots c) and d): Comparison of inter-model envelope to measured ADCP data envelope; also shown in the time series from the measured data. Bottom row plots e) and f): mean inter-model error (blue line) and intermodal standard deviation (green line) for the speed envelope.

Figure 12: Summary of inter-model spatial statistics. Top left a): Inter-model mean of predicted maximum speed as taken from the 5-m resolution runs. Bottom left b): Inter-model standard deviation of predicted maximum speed as taken from the 5-m resolution runs. Right column: Inter-model standard deviation of predicted maximum speed as taken from the 5-m resolution runs (c), 10-m resolution runs (d), and 20-m resolution runs (e).

Figure 13: Snapshots of vertical vorticity at the same simulation time for the same numerical model, with 10-m resolution (a) and 5-m resolution (b). Note that the locations of the ADCP's are shown by the black dots.

Figure 14: The effect of spatial-averaging on model convergence, with the top plot indicating the locations of the "small box" and the "large box" as referenced in the two lower subplots. The two lower subplots show the box-averaged maximum speeds for each model at 20- and 10-m resolutions, scaled by the box-averaged speed from each model's 5-m resolution simulation; middle subplot for the small box, and lower subplot for the large box. Note that two model results are missing; one due to the use of different boundary conditions with different resolutions, and the other due to an inability to perform a 5-m resolution simulation.

Figure 15: Example of a current-threshold plot, where the color at each location gives the fraction of models that predicted a maximum current greater than 2 m/s at that particular location.

5   Conclusions and Recommendations for Future Work

While the datasets used in this benchmarking activity have shortcomings, they do contain the physical processes relevant to a reasonable prediction of nearshore, tsunami-induced currents. For example, BM#1 is a relatively small-scale experiment, with Reynolds numbers below typical geophysical conditions and uniformity in bathymetry and flow conditions that would not be expected in the field. However, similar to the solitary wave runup experiments that have become a validation keystone for inundation models, BM#1 represents a canonical and fundamental test case that all models should be able to reproduce. An ability to simulate bottom-driven spatial velocity shear and the resulting coherent structures created as flow oscillates is integral for predicting flow complexity in shallow water.

While the tsunami community would benefit from a re-examination of the BM#1 experiments, perhaps at a larger scale with state-of-the-art measurement techniques, the existing data represents an ideal case to compare tsunami models. There is strong de-coupling of the currents with the mean flow, and this de-coupling is driven by bottom shear without the presence of vertical walls and shorelines, which may be numerically troublesome for depth-averaged models. With the results from all the benchmarks in mind, it is reasonable to set the following BM#1 accuracy benchmarks required of models to be used for speed predictions:

- Models must demonstrate numerical convergence with the use of a reasonable bottom friction coefficient.
- If the model is to be used for nearshore speed predictions including ports and harbors, then the ratio of mean modeled fluctuation to mean measured fluctuation must be between 0.5-1.5 for all four velocity components included in BM#1 (comparisons shown in Figure 7).
- If the model is to be used for momentum flux calculations, then a mean absolute error in speed^2 below 0.5 (comparisons shown in Figure 10).

BM#1 represents a starting point to ensure that speed predictions in complex nearshore flows are reasonable. Additional accuracy tests should be added in the future, in both the form of laboratory and field datasets. Of primary importance for a field benchmark dataset is high temporal and spatial resolution, for which existing data is deficient. Additionally, a separate class of overland flow focused accuracy benchmarks, perhaps starting with BM#4, must be developed. Indications from this study are that velocity predictions during inundation exhibit very large inter-model variability.

Analysis of BM#2 demonstrated the variability of field-scale currents in the presence of eddies. Indications are that no single model can provide a converged result, as changes in resolution lead to small changes in boundaries and resolvable shear, which then leads to large variability in the evolution of eddies and the predicted maximum currents. Likewise, the chaotic nature of eddies is physically fundamental, possibly making during-event interpretation of point measurements (e.g. ADCP) challenging. The presented analysis leads to a clear argument for the use of ensemble modeling for currents in areas affected by eddies. Ensembles can be generated with multiple models or multiple realizations with a single model. While ensembles are not always available or financially practical, the current practice of using single (or a select few) realizations with a single model must at least be accompanied by careful and conservative expert interpretation and identification of where potential eddies could form and move in the nearshore region.

References

1. Arcos, M.E.M., LeVeque, R.J. (2015). Validating Velocities in the GeoClaw Tsunami Model using Observations Near Hawaii from the 2011 Tohoku Tsunami. Pure Appl. Geophys., 172 (3–4), doi:10.1007/s00024-014-0980-y

2. Borrero, J., Bell, R., Csato, C., DeLange, W., Greer, D., Goring, D., Pickett, V. and Power, W. (2012) Observations, Effects and Real Time Assessment of the March 11, 2011 Tohoku-oki Tsunami in New Zealand, Pure and Applied Geophysics,

3. Cheung KF, Bai Y., Yamazaki Y. (2013) Surges around the Hawaiian Islands from the 2011 Tohoku tsunami. J Geophys Res 118:5703-5719, DOI 10.1002/jgrc.20413.

4. Lloyd, P.M., Stansby, P.K., (1997). Shallow water flow around model conical island of small slope. II: Submerged. Journal of Hydraulic Engineering, ASCE 123 (12), 1068-1077.

5. Lloyd, P.M., Stansby, P.K., (1997). Shallow water flow around model conical island of small slope. II: Submerged. Journal of Hydraulic Engineering, ASCE 123 (12), 1057-1067.

6. Park, H., Cox, D., Lynett, P., Wiebe, D., and Shin, S. (2013) "Tsunami Inundation Modeling in Constructed Environments: A Physical and Numerical Comparison of Free-Surface Elevation, Velocity, and Momentum Flux." Coastal Engineering, v. 79, pp. 9-21, doi: 10.1016/j.coastaleng.2013.04.002.

ALASKA GI'-T Benchmark Results

Dmitry J. Nicolsky [a]

[a] University of Alaska Fairbanks, Geophysical Institute, 903 Koyokuk Drive, Fairbanks, AK 99775-7320

Abstract. A robust numerical model ALASKA GI'-T is applied to simulate tsunami currents in the framework of non-linear shallow water theory. The numerical code adopts a staggered leapfrog finite-difference scheme to solve the shallow water equations formulated for depth-averaged water fluxes in spherical coordinates. For large scale problems, the developed algorithm is efficiently parallelized employing a domain decomposition technique. The numerical model is benchmarked using the laboratory measurements and field observations. In all conducted tests the calculated numerical solution agrees with the measurements. We summarize results of numerical benchmarking of the model, its strengths and limits with regards to reproduction of fundamental features of tsunami currents.

Address all correspondence to: D.J. Nicolsky, University of Alaska Fairbanks, Geophysical Institute, 903 Koyokuk Drive, Fairbanks, AK 99775-7320; Tel: +1 907-474-7397; E-mail: djnicolsky@alaska.edu

1 Model Background

A numerical model for simulation of tsunami propagation and runup - ALASKA GI'-T - is developed at the Geophysical Institute, University of Alaska Fairbanks. The ALASKA GI'-T model stems from the method TUNAMI by Imamura (1995), however while validating the original tsunami runup algorithm, the numerical scheme of TUNAMI was significantly modified. Currently, the ALASKA GI'-T model is used to predict propagation and runup of hypothetical tsunamis along the Alaska shore (Suleimani *et al.,* 2013; Nicolsky *et al.,* in press).

The ALASKA GI'-T model is tested against analytical predictions, laboratory measurements, and field observations (Nicolsky *et al.,* 2011; NTHMP, 2012). In computer experiments modeling propagation and runup of a solitary wave on a canonical beach and on conically shaped island, numerical calculations were reported to be within established errors proposed by (Synolakis *et al.,* 2007). To test the model against field observation, Nicolsky *et al.* (2011) performed simulation of the 1993 Okushiri tsunami. The computed runup around Okushiri island is within the variability of field observations. However, the local extreme runup, e.g. in the narrow gully near the village of Monai, is sensitive to the near shore interpolation of bathymetry/topography. The computer simulation of the 1993 Okushiri tsunami also captured the overland flow at the cape Aonae, where the maximum destruction was reported. No adjustments to the original code of the ALASKA GI'-T model were performed to complete the following benchmark problems.

2 Model Equations

Nonlinear shallow water theory is commonly used to predict propagation of long waves in the ocean and inundation of coastal areas (Synolakis and Bernard, 2006). The water depth η and the horizontal water velocity $\boldsymbol{u}$ are described in the spherical coordinates by the mass and linear momentum conservation principles:

$$\frac{\partial}{\partial t}\eta + \nabla\cdot(\eta\,\mathbf{u}) = 0, \tag{1}$$

$$\frac{\partial}{\partial t}(\eta\,\mathbf{u}) + \nabla\cdot(\eta\,\mathbf{u}\mathbf{u}) + g\eta\,\nabla\xi + f\eta(\mathbf{e}_r\times\mathbf{u}) + \eta\boldsymbol{\tau} = 0, \tag{2}$$

Here, $\xi = h + \eta$, is the water level, h is the bathymetry, g is the acceleration of gravity, f is the Coriolis parameter, and $\mathbf{e}_r$ is the outward unit normal vector on the sphere. The term τ represents the bottom friction:

$$\boldsymbol{\tau} = \frac{\nu}{2\eta}\mathbf{u}\|\mathbf{u}\|, \qquad n^2 = \frac{\nu}{2g}\eta^{1/3}.$$

The constants ν and n are called the friction coefficient and Manning's roughness, respectively. The above system of equations is supplemented by the initial and boundary conditions. The initial water displacement is assumed to be equal to a coseismic uplift and subsidence of the sea floor, while the either a non-reflective boundary condition or a solid wall boundary condition is assumed around the edges of the computational domain.

3 Numerical Solution Method

The system of equations (1) and (2) is approximated in spherical coordinates by finite differences on Arakawa C-grid (Arakawa and Lamb, 1977). The spatial derivatives are discretized by central difference and upwind difference schemes and a semi-implicitly first order scheme in time (Kowalik and Murty, 1993). For the sake of brevity and clarity we outline the numerical scheme for a 1-D version of equations (1-2) in Cartesian coordinates and with centers of the grid cells at $x_i = i\Delta x$. We also assume that there is no Coriolis force, and hence the computational system of equations yields

$$\eta_i^{n+1} - \eta_i^n + \gamma\left(U_{i+1/2}^n - U_{i-1/2}^n\right) = 0,$$
$$U_{i+1/2}^{n+1} - U_{i+1/2}^n + \gamma\left[\alpha_{i+1/2}^n\left(U_{i+3/2}^n u_{i+3/2}^n - u_{i+1/2}^n U_{i+1/2}^n\right) + \left(1 - \alpha_{i+1/2}^n\right)\left(U_{i+1/2}^n u_{i+1/2}^n - u_{i-1/2}^n U_{i-1/2}^n\right)\right]$$
$$+ g\gamma\eta_{i+1/2}^{n+1}\left(\xi_{i+1}^{n+1} - \xi_i^{n+1}\right) + \mathrm{T}_{i+1/2}^{n+1} = 0,$$

where $\xi_i^n = h_i + \eta_i^n$, and $\eta_{i+1/2}^n = \left(\eta_{i+1}^n + \eta_i^n\right)/2$. In the above equations, the subscript marks an index of the cell, while the superscript is related to the time step $t_n = n\Delta t$; $\gamma = \Delta t/\Delta x$. Since we employ the C-grid, the water depth η_i, the water level ξ_i, and the bathymetry h_i are defined at grid cell centers $\{1,...,n\}$, while the depth averaged water flux $U_{i+1/2}$ and water velocity $u_{i+1./2}$ are defined at the cell boundaries $\{1/2, 3/2, ..., n-1/2\}$. The water flux $U_{i+1/2}^n$ is related to the water velocity $u_{i+1./2}^n$ by $U_{i+1/2}^n = u_{i+1./2}^n\left(\eta_i^n + \eta_{i+1}^n\right)/2$. In the above formula the coefficient α_i^n is equal to one if $U_{i-1/2}^n$ is positive, otherwise it is zero. The bottom friction term $T_{i+1/2} = (\eta\tau)_{i+1/2}$ is discretized according to a semi-implicit scheme by Goto *et al.* (1997):

$$\mathrm{T}_i^{n+1} = \Delta t\, g\, \frac{\mu^2}{(\eta_{i+1/2}^{n+1})^{4/3}}\, \frac{\left(U_i^{n+1} + U_i^n\right)}{2}\left|u_i^n\right|.$$

To implement the wetting/drying scheme, we check the water level at the center and boundaries between two adjacent cells. When at the center of the *i-th* cell $\eta_i < \delta = 10^{-3}\, O(\eta)$, it is then assumed that this cell is dry and η_i is set to zero. We introduce the notion of left and right cell boundaries. The cell boundary $i + 1/2$ is called left if the bathymetry/topography at cell $i+1$ is lower than at cell i, i.e. $h_i \geq h_{i+1}$. Otherwise, the cell boundary is called the right one. For brevity, we formulate

36

inequalities representing the conditions only for left cell boundaries. The inequalities associated with right cell boundaries are similarly formulated by taking into account the left-right symmetry. The water can flow across the left cell boundary if either $\xi_{i+1} \geq \xi_i$, or there is some water, i.e. $\eta_i \geq \delta$ on the upper side to flow to the lower side. The reader is referred to Nicolsky *et al.* (2011) for further details about the drying/wetting algorithm and its benchmarking. The discretized equations are coded in FORTRAN using the Portable, Extensible Toolkit for Scientific computations (Balay *et al.*, 2004) and the MPI standard (Gropp *et al.*, 1999).

4   Benchmark Problem Comparisons

4.1 Benchmark Problem #1: Steady Flow over Submerged Obstacle

The information provided by workshop organizers was used to generate the bathymetry at the 0.01 m grid resolution. Some special attention was devoted to ensure that the generated bathymetry and the boundary conditions are point-wise symmetrical in the longshore direction. The Manning's roughness *n* was uniformly applied for the entire bathymetry and for each value of roughness *n*, the inflow water flow was calibrated such that the water depth in front of the island on the flat bottom is 0.054 m. The water flow was gradually increased from zero to the specified value of U = 0.115 m/s.

At the beginning of each numerical experiment the initial flow around the obstacle was symmetrical with a slight water level depression on the lee side of the island. The vortex street is generated in all considered experiments with the Manning's roughness $0 \leq n \leq 0.02$. The time of the first vortex appearance depends on the value of Manning's roughness *n*; for larger values of *n* the vortex appears later in the numerical experiments. Numerical experiments with coarser and finer spatial resolutions revealed that the vortex street dynamics do not significantly change on the grid resolution and the time step value.

Time series of the *u*- and *v*- components of the flow velocity are recorded on the lee side of the island at two specified locations. In all computer experiments, after the appearance of the first vortex, the computed velocities show a clear periodic signal, see figure 1. The period of oscillations depends on the Manning's roughness *n*. At point 1, the computed *u*-component of the velocity underestimates the laboratory measurements, while the computed *v*-component shows a good agreement with the recorded amplitude and period of oscillations. A good agreement between the measured and computed flow velocities is also obtained at point 2.

Figure 1. Experimental data (dots) and numerical simulation (solid line, not shown) for a) U velocity component at time series location 1, b) V velocity component at time series location 1, c) U velocity component at time series location 2, and d) V velocity component at time series location 2.

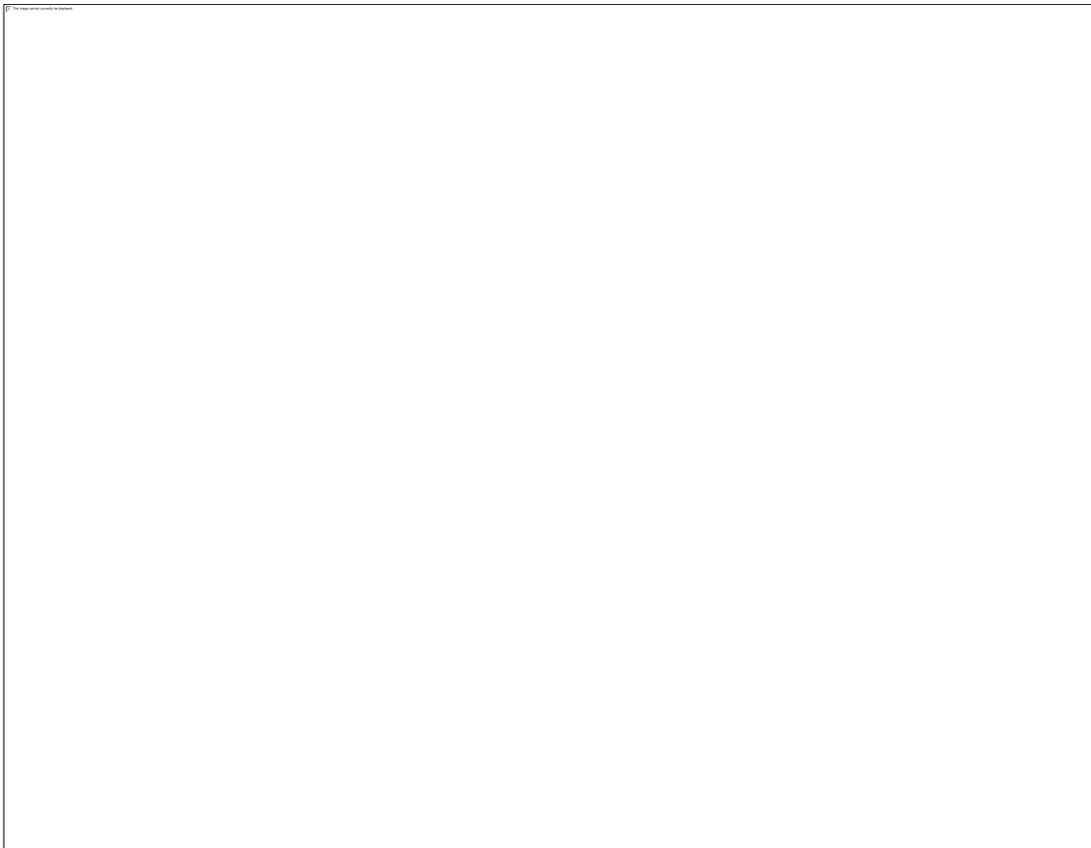## 4.2 Benchmark Problem #2: Tsunami Currents in Hilo Harbor

The information provided by workshop organizers was used to generate the digital elevation model of the Hilo Harbor at the specified grid resolutions of 5, 10, and 20 m. Along the "wet" boundary of the computational grid, a non-reflective boundary condition was prescribed. To simulate an incident wave, an internal wave maker was positioned along the northwest part of the domain. The wave maker length was adjusted in order to match the modeled and observed water level dynamics at the control point.

The top plot in figure 2 illustrates the comparison of the modeled and observed 2011 Tohoku tsunami dynamics at the tide gauge. We note that the first three wave crests/troughs mutually agree with each other. The later waves in the computer experiment overestimate the observations. One of the possible explanations might be that the height of the incident wave is overestimated at the control point.

During all computer experiments, the water level was recorded at two ADCP buoys in the Hilo Harbor. The comparison of the modeled and observed water velocities is shown in the center and bottom plots in figure 2. The modeled u- and v-components of the water velocity favorably

compare with their observed counterparts. However, because of the coarse time sampling of the tsunami currents during the Tohoku 2011 event, some peak velocities might be missing in the recorded data.

In addition to the comparison of the water velocities at the buoys, maximum tsunami current maps were computed for each numerical experiment at 5, 10, and 20 m grid resolution. Figure 3 shows the maximum tsunami current velocity map for the resolution of 10 m. The comparison of the 20-m, 10-m, and 5-m resolution maps show that with the decrease of the grid resolution, finer details of the flow pattern appear at the tip of the breakwater and some jetties. In all conducted numerical experiments, it appears that no eddies were shed from the tip of breakwaters. We recall that following the benchmark description, a uniform Manning's roughness n=0.025 was assumed for the entire computational domain. The numerical results appear to be converges at the resolution of 10 m.

Figure 2. Measured data (dashed line) and numerical simulation (solid line) at the harbor tide gage (top), HA25 ADCP (middle), and HA26 ADCP (bottom).

Figure 3. Maximum predicted fluid speed during entire duration of the 10-m resolution simulation.

4.4 Benchmark Problem #4: Flow through a City Building Layout

The information provided by workshop organizers was used to generate the digital elevation model of the small-scale model of the town of Seaside, Oregon at the 0.04 m resolution. The time series of incident wave elevation at x=5 m was used to force the numerical model at x=5 m.

Numerical experiments for values of the Manning's roughness n=0.005, 0.01, and 0.02 were conducted. In all cases the comparison of the modeled and recorded water level dynamics at the control point x=18.618 m reveal that the simulated wave reproduce the observed wave very well. The modeled incident wave height was only 0.01 m less than the measured one. The largest differences between the numerical and laboratory experiments occur during the inundation stage. Figure 4 illustrates the comparison of the modeled and observed flow depth dynamics at the series of gauge B1, B4, B6, and B9.

The modeled flow somewhat underestimates the maximum observed water level at gauge B1, captures the maximum water level at gauges B4 and B6, and again underestimates the maximum observed water level at gauge B9. At all gauges B1, B4, and B6 the simulate flow dynamics is in good agreement with the laboratory measurements. We note that the modeled flow reaches all points earlier than it is observed in the laboratory experiment.

Figure 5 illustrates that the comparison of the modeled and observed water flow velocities at the gauges. We indicate that the records of the computed water velocities likely lack the water velocity readings in a short period of time when the flow reaches a sensor. Nevertheless, the modeled water velocities qualitatively agree with the available laboratory measurements, with the computed velocities slightly underestimating the measurements. A main difference between the computer experiment is in timing of the inundation at gauge B9. Namely, the simulated water flow quicker reaches gauge B9 for the smaller Manning's roughness values, see the last plot in figure 5.

Figure 4. Comparison of the simulated and observed flow depth dynamics at gauges B1, B4, B6, and B9. The dashed line corresponds to the laboratory measurements. The colored solid lines are associated with numerical experiments, in which the Manning's roughness *n* was assumed to be 0.005, 0.01, and 0.02.

Figure 5. Comparison of the simulated and observed water velocity at gauges B1, B4, B6, and B9. The dashed line corresponds to the laboratory measurements. The colored solid lines are associated with numerical experiments, in which the Manning's roughness *n* was assumed to be 0.005, 0.01, and 0.02.

5   Conclusions

A numerical model ALASKA GI'-T is verified and validated using a set of benchmark problems (BPs) developed for the 2015 NTHMP/MMS Workshop: Tsunami Currents in Portland, OR. In particular, the numerical solution is tested against the laboratory measurements (BP 1 & BP 4) and field observations (BP 2). In all considered benchmark problems, the simulated and observed water level dynamics agree with each other. Results of BP 1 and 4 show that the Manning's roughness coefficient exerts some controls on the flow dynamics. In case of BP 2, computer experiments reveal that the numerical simulations converge at the resolution of 10 m. No apparent eddies were shed from the tip of breakwater in the computer experiments for BP 2. Finally, we mention that no adjustments to the original code of the ALASKA GI'-T model were performed to complete the benchmark problems.

6   Acknowledgments

References

1. Arakawa, A., Lamb, V., 1977. Computational design of the basic dynamical processes of the UCLA general circulation model. In: Methods in Computational Physics. Vol. 17. Academic Press, pp. 174–267.

2. Balay, S., Buschelman, K., Eijkhout, V., Gropp, W. D., Kaushik, D., Knepley, M. G., McInnes, L. C., Smith, B. F., Zhang, H., 2004. PETSc Users Manual. Tech. Rep. ANL-95/11 - Revision 2.1.5, Argonne National Laboratory.

3. Goto, C., Ogawa, Y., Shuto, N., Imamura, F., 1997. Numerical method of tsunami simulation with the leap-frog scheme. Manuals and Guides 35, UNESCO: IUGG/IOC TIME Project.

4. Gropp, W., Lusk, E., Skjellum, A., 1999. Using MPI: Portable Parallel Programming with the Message-Passing Interface. The MIT press, 406 pp..

5. Imamura, F., 1995. Tsunami numerical simulation with the staggered leap-frog scheme. Tech. rep., School Disaster Control Research Center, Tohoku University, Manuscript for TUNAMI code, 33 pp..

6. Kowalik, Z., Murty, T., 1993. Numerical modeling of ocean dynamics.World Scientific, 481 pp..

7. National Tsunami Hazard Mapping Program (NTHMP), 2012, Proceedings and results of the 2011 NTHMP Model Benchmarking Workshop: Boulder, CO, U.S. Department of Commerce/NOAA/NTHMP, NOAA Special Report, 436 p. http://nthmp.tsunami.gov

8. Nicolsky, D. J., Suleimani, E., and Hansen, R., 2011, Pure and Applied Geophysics, Validation and verification of a numerical model for tsunami propagation and runup, 168:1199–1222, doi 10.1007/s00024-010-0231-9.

9. Nicolsky, D.J., Suleimani, E.N., Freymueller, J.T., and Koehler, R.D., in press, Tsunami inundation maps of Fox Island communities including Dutch Harbor and Akutan, Alaska: Alaska Division of Geological & Geophysical Surveys Report of Investigation.

10. Suleimani, E.N., Nicolsky, D.J., and Koehler, R.D., 2013, Tsunami inundation maps of Sitka, Alaska: Alaska Division of Geological & Geophysical Surveys Report of Investigation 2013-3, 76 p., 1 sheet, scale 1:250,000. doi:10.14509/26671

11. Synolakis, C., and Bernard, E., 2006, Tsunami science before and beyond Boxing Day 2004:Philosophical Transactions of the Royal Society A, v. 364, n. 1845, p. 2231–2265.

12. Synolakis, C., Bernard, E., Titov, V., Kânoğlu, U., and González, F.: Standards, criteria, and procedures for NOAA evaluation of tsunami numerical models., OAR PMEL-135 Special Report, NOAA/OAR/PMEL, Seattle, Washington,, 55 pp.., 2007.

NAMI DANCE Benchmark Results

Ahmet Cevdet Yalçıner,[a] Andrey Zaytsev[b], Utku Kânoğlu[c], Gozde Guney Dogan[a], Deniz Velioğlu[a], Rozita Kian[a], Betul Aytore[a], Naeimeh Sharghivand[c]

[a] Middle East Technical University, Department of Civil Engineering, Ocean Engineering Research Center, Dumlupinar Boulevard, No:1 Cankaya, Ankara, Turkey, 06800

[b] Special Research Bureau for Automation of Marine Researches, Far Eastern Branch of Russian Academy of Sciences, 693013 Russia Uzhno-Sakhalinsk Gorkiy str. 25

[c] Middle East Technical University, Department of Engineering Sciences, Dumlupinar Boulevard No:1, Cankaya, Ankara, Turkey, 06800

Abstract. The numerical model NAMI DANCE, which solves nonlinear shallow water equations, is applied to the benchmark problems provided by NTHMP Mapping & Modeling Benchmarking Workshop. NTHMP benchmark problem set not only includes experimental problems but also geophysical scales problems. Comparisons of numerical estimates and measurements as required by benchmark problems are presented. The fairly good agreements between numerical and benchmark data are obtained.

Address all correspondence to: Ahmet Cevdet Yalciner, Middle East Technical University, Department of Civil Engineering, Ocean Engineering Research Laboratory, Dumlupinar Boulevard No:1 Cankaya, Ankara, Turkey, 06800; Tel: +90 312-210-54-96; Fax: +90 312-210-54-95; E-mail: yalciner@metu.edu.tr

1   Model Background

NAMI DANCE is a computational tool developed by Profs Andrey Zaytsev, Ahmet Yalciner, Anton Chernov, Efim Pelinovsky, and Andrey Kurkin especially for tsunami modeling. It provides numerical modeling and efficient visualization of tsunami generation, propagation, and inundation mechanisms. It is developed in C++ programming language using leap-frog scheme numerical solution procedure, which is employed in TUNAMI-N2 (Imamura, 1989; Shuto, Goto and Imamura, 1990). NAMI DANCE computes all necessary tsunami parameters. It can also provides 3D plots of sea state at selected time intervals from different camera position and light conditions, and also animates the tsunami propagation from source to target including inundation. NAMI DANCE has been applied to analytical, experimental and field benchmark problems as outlined in Synolakis et al. (2008) (Ozer and Yalciner, 2011; Sozdinler, Yalciner, and Zaytsev, 2014; Sozdinler et al., 2015; Yalciner et al., 2007b) and also applied to hindcast tsunami events (Dilmen et al., 2014; Heidarzadeh, Krastel, and Yalciner, 2014; Yalciner et al., 2007a, 2014a,b; Zahibo et al., 2003).

2   Model Equations

In the theory of long waves, the vertical motion of water particles has no effect on the pressure distribution. Based upon this approximation and neglecting the vertical acceleration, the equations of mass conservation and momentum in three-dimensional (two-spatial, one-temporal) problem are expressed by the following set of equations:

$$\frac{\partial h}{\partial t} + \frac{\partial u}{\partial x} + \frac{\partial v}{\partial y} + \frac{\partial w}{\partial z} = 0,$$

$$\frac{\partial u}{\partial t} + u\frac{\partial u}{\partial x} + v\frac{\partial u}{\partial y} + w\frac{\partial u}{\partial z} + \frac{1}{\rho}\frac{\partial p}{\partial x} + \frac{1}{\rho}\left(\frac{\partial t_{xx}}{\partial x} + \frac{\partial t_{xy}}{\partial y} + \frac{\partial t_{xz}}{\partial z}\right) = 0,$$

$$\frac{\partial v}{\partial t} + u\frac{\partial v}{\partial x} + v\frac{\partial v}{\partial y} + w\frac{\partial v}{\partial z} + \frac{1}{\rho}\frac{\partial p}{\partial y} + \frac{1}{\rho}\left(\frac{\partial t_{xy}}{\partial x} + \frac{\partial t_{yy}}{\partial y} + \frac{\partial t_{yz}}{\partial z}\right) = 0,$$

$$g + \frac{1}{\rho}\frac{\partial \rho}{\partial z} = 0, \tag{2.1}$$

where x and y are the horizontal axes, z is the vertical axis, t is time, h is the still water depth, η is the vertical displacement of water surface above the still water surface, u, v and w are the water particle velocities in the x, y and z directions respectively, g is the gravitational acceleration, and τ_{ij} is the normal or tangential shear stress in the i direction on the j normal plane.

The equation of momentum in the z-direction with the dynamic condition at a surface ($p = 0$) yields the hydrostatic pressure $p = \rho g(h - z)$. Then, wave propagation problems can be solved by using the governing equations –Eqs. (2.1)– and employing boundary conditions. The dynamic and kinetic conditions at surface and bottom are given as follows:

$$p = 0, \qquad\qquad\qquad \text{at } z = \eta, \tag{2.2}$$

$$w = \frac{\partial h}{\partial t} + u\frac{\partial h}{\partial x} + v\frac{\partial h}{\partial y}, \qquad\qquad \text{at } z = \eta, \tag{2.3}$$

$$w = -u\frac{\partial h}{\partial x} - v\frac{\partial h}{\partial y}, \qquad\qquad \text{at } z = -h. \tag{2.4}$$

Now, Eqs. (2.1) can be integrated from the bottom to the surface using Leibniz rule. For example, the first term of the momentum equation in the x-direction is rewritten as follows:

$$\int_{-h}^{h} \frac{\partial u}{\partial t} dz = \frac{\partial}{\partial t} \int_{-h}^{h} u\,dz - u\frac{\partial h}{\partial t}\bigg|_{z=h} + u\frac{\partial(-h)}{\partial t}\bigg|_{z=-h}. \tag{2.5}$$

With dynamic and kinetic conditions –Eqs. (2.2)-(2.4)– and Leibniz rule Eq. (2.5), the following two dimensional equations, so called nonlinear shallow-water wave equations, can be obtained using discharge fluxes:

$$\frac{\partial h}{\partial t} + \frac{\partial M}{\partial x} + \frac{\partial N}{\partial y} = 0,$$

$$\frac{\partial M}{\partial t} + \frac{\partial}{\partial x}\left(\frac{M^2}{D}\right) + \frac{\partial}{\partial y}\left(\frac{MN}{D}\right) + gD\frac{\partial h}{\partial x} + \frac{t_x}{\rho} = A\left(\frac{\partial^2 M}{\partial x^2} + \frac{\partial^2 M}{\partial y^2}\right),$$

$$\frac{\partial N}{\partial t} + \frac{\partial}{\partial x}\left(\frac{MN}{D}\right) + \frac{\partial}{\partial y}\left(\frac{N^2}{D}\right) + gD\frac{\partial h}{\partial y} + \frac{t_y}{r} = A\left(\frac{\partial^2 N}{\partial x^2} + \frac{\partial^2 N}{\partial y^2}\right), \qquad (2.6)$$

where D is the total water depth given by $h+\eta$, τ_x and τ_y are the bottom frictions in the x- and y- directions respectively, A is the horizontal eddy viscosity which is assumed to be constant in space, the shear stress on a surface wave is neglected. M and N are the discharge fluxes in the x- and y- directions, which are given by,

$$M = \int_{-h}^{h} u\,dz = u(h+h) = uD \quad \text{and} \qquad\qquad\qquad (2.7)$$

The bottom friction is generally expressed as follows, in an analogy to the uniform flow,

$$\frac{t_x}{r} = \frac{1}{2g}\frac{f}{D^2}M\sqrt{M^2 + N^2} \quad \text{and} \quad \frac{t_y}{r} = \frac{1}{2g}\frac{f}{D^2}N\sqrt{M^2 + N^2}. \qquad (2.8)$$

where f is the friction coefficient. Without any detailed discussion of the value of f it is preferred to use Manning's roughness n. The friction coefficient f and Manning's roughness n are related by

$$n = \sqrt{\frac{fD^{1/3}}{2g}}. \qquad (2.9)$$

This implies that f becomes rather large when the total depth D is small as n remains almost constant. Thus, the bottom friction terms are expressed by

$$\frac{t_x}{r} = \frac{n^2}{D^{7/3}}M\sqrt{M^2 + N^2} \quad \text{and} \quad \frac{t_y}{r} = \frac{n^2}{D^{7/3}}N\sqrt{M^2 + N^2}. \qquad (2.10)$$

Throughout the present model, the expression of bottom friction in Eq. (2.10) is being used. n should be selected depending on the condition of the bottom surface. For the propagation of tsunami in the shallow water, the horizontal eddy turbulence could be negligible compared to the bottom friction except for run-up on the land. The following equations are therefore given as the fundamental equations in the model.

$$\frac{\partial h}{\partial t} + \frac{\partial M}{\partial x} + \frac{\partial N}{\partial y} = 0,$$

$$\frac{\partial M}{\partial t} + \frac{\partial}{\partial x}\left(\frac{M^2}{D}\right) + \frac{\partial}{\partial y}\left(\frac{MN}{D}\right) + gD\frac{\partial h}{\partial x} + \frac{n^2}{D^{7/3}}M\sqrt{M^2 + N^2} = 0,$$

$$\frac{\partial N}{\partial t} + \frac{\partial}{\partial x}\left(\frac{MN}{D}\right) + \frac{\partial}{\partial y}\left(\frac{N^2}{D}\right) + gD\frac{\partial h}{\partial y} + \frac{n^2}{D^{7/3}}N\sqrt{M^2 + N^2} = 0. \qquad (2.11)$$

Finally, using the governing equations briefly described above, NAMI DANCE takes input tsunami source from either defined rupture or pre-determined wave form and computes its propagation,

coastal amplification, and coastal inundation. NAMI DANCE also provides certain quantities such as arrival time of initial wave and maximum wave, and distribution of water surface elevations (sea state), current velocities with its direction and fluxes. Distribution of maximum water elevations, maximum current velocities and directions, maximum flow depths, and maximum fluxes computed during simulation, Froude Number and time histories of water surface fluctuations at selected gauge locations can also be presented.

3   Numerical Solution Method

In order to deal with discrete values in numerical computations using Finite Difference Method, $\eta(x,y,t)$, $M(x,y,t)$, and $N(x,y,t)$ are expressed using the structure of the staggered leap-frog scheme. The discretization of water surface elevation and fluxes are in the following form:

$$h(x,y,t) = h(i\mathrm{D}x, j\mathrm{D}y, n\mathrm{D}t) = h_{i,j}^{n},$$

$$M(x,y,t) = M\{(i + \tfrac{1}{2})\mathrm{D}x\}, j\mathrm{D}y, (n + \tfrac{1}{2})\mathrm{D}t\} = M_{i+\frac{1}{2},j}^{n+\frac{1}{2}},$$

$$N(x,y,t) = N\{i\mathrm{D}x\}, (j + \tfrac{1}{2})\mathrm{D}y, (n + \tfrac{1}{2})\mathrm{D}t\} = N_{i,j+\frac{1}{2}}^{n+\frac{1}{2}}, \qquad (3.1)$$

where Δx and Δy are the grid sizes in x- and y-directions respectively, Δt is the time step. The points for water depth h are the same as those for water elevation, η. But the points for fluxes are at mid-point in respective direction and at mid time step. Details of numerical scheme are given in Shuto, Goto, and Imamura (1990). NAMI DANCE could employ in Cartesian or spherical coordinate system with or without nonlinear terms. The equations in spherical coordinates with Coriolis and dispersion are given in Dao and Tkalich (2007).

4   Benchmark Problem Comparisons

4.1 Benchmark Problem #1: Steady Flow over Submerged Obstacle

Benchmark Problem 1 is modeled with the grid size and time step as Δx=0.01m and Δt=0.005sec respectively. Manning's roughness coefficient is taken as 0.01. In the simulations the flow at the tip of the cone is controlled by limiting the flow depth with 0.015m, which provided weak turbulence at the top of the cone. The numerical results are plotted with experimental data in Figure 1 for the velocity components at the horizontal plane in the direction of flow (*u*) and in the perpendicular direction to the flow (*v*) at two different gauge locations.

Figure 4. Experimental data (dots) and numerical simulation (solid line, not shown) for a) U velocity component at time series location 1, b) V velocity component at time series location 1, c) U velocity component at time series location 2, and d) V velocity component at time series location 2.

4.2 Benchmark Problem #2: Tsunami Currents in Hilo Harbor

Numerical modelling of benchmark problem 2 was carried out at 5m, 10m and 20m grids resolutions using the Manning's coefficient of 0 and 0.015. The time series of the wave is inputted either from upper border. The results of simulations with different spatial grid resolutions and different Manning's coefficients are compared to identify grid resolution and friction effect. It was observed that 10m-grid resolution represents measured data reasonably well. The computed and measured time series of water surface elevations are compared at the tide gauge location for Manning's roughness coefficient of 0 and 0.015 at 10m-grid resolution in Figure 2. Figure 2 also shows comparison of computed and measured E-W and N-S velocity components respectively, with Manning's roughness coefficient of 0 and 0.015 at 10m-grid resolution.
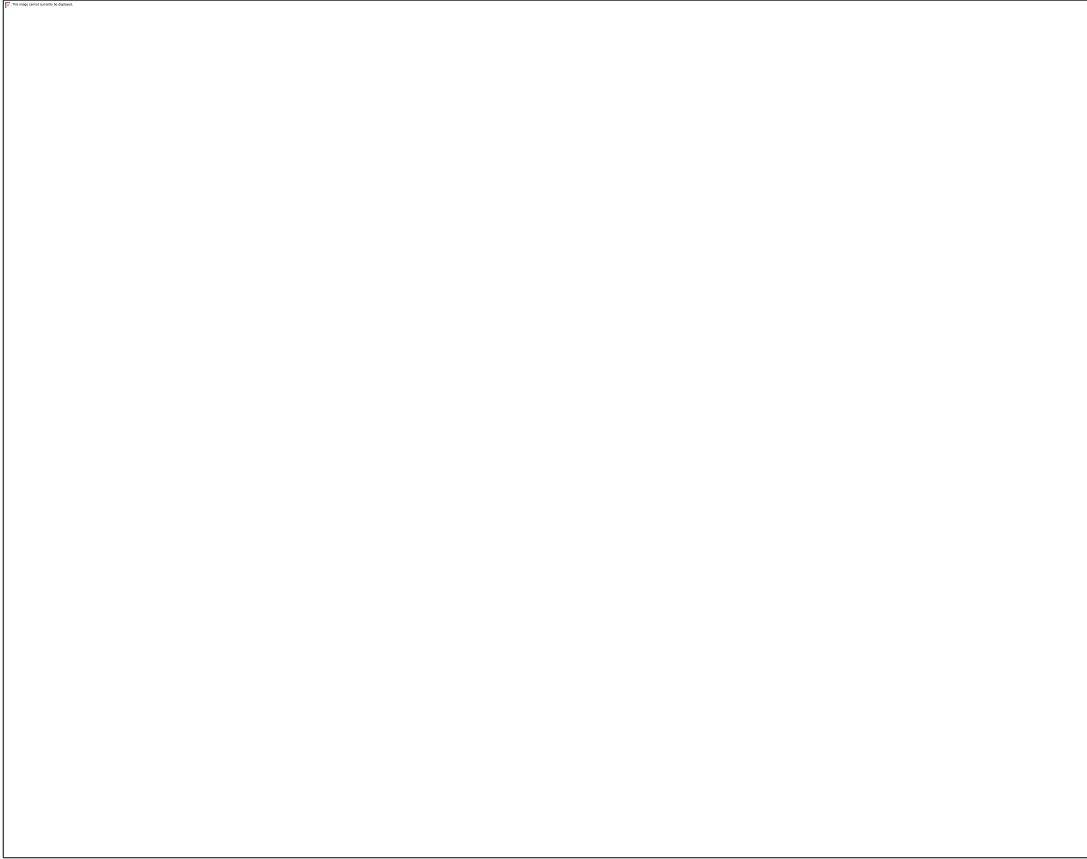
Figure 5. Measured data (dashed line) and numerical simulation (solid line) at the harbor tide gage (top), HA25 ADCP (middle), and HA26 ADCP (bottom).

Figure 6. Maximum predicted fluid speed (m/s) during entire duration of the 10-m resolution simulation.

4.3 Benchmark Problem #3: Tsunami Currents in Tauranga Harbor

The recording the Japan 2011 tsunami in Tauranga Harbor, New Zealand is presented in this benchmark problem. The unique feature of this benchmark problem is to attempt to include the tide effect. The speed component of the tsunami signal is comparable to the speed of the tidal component at the ADCP measurement location, indicating the possibility of a not-linear superposition of the two components. The free surface elevation (from tide stations) and velocity information (from ADCP) are computed. In the simulations the grid size and time step are selected as 30m and 0.25sec respectively. The comparisons of computed and measured water surface elevations at Tug Berth, Sulfur and Moturiki locations, and the current speed and current velocity components in E-W and S-N directions at ADCP location are presented in Figures 4-9.
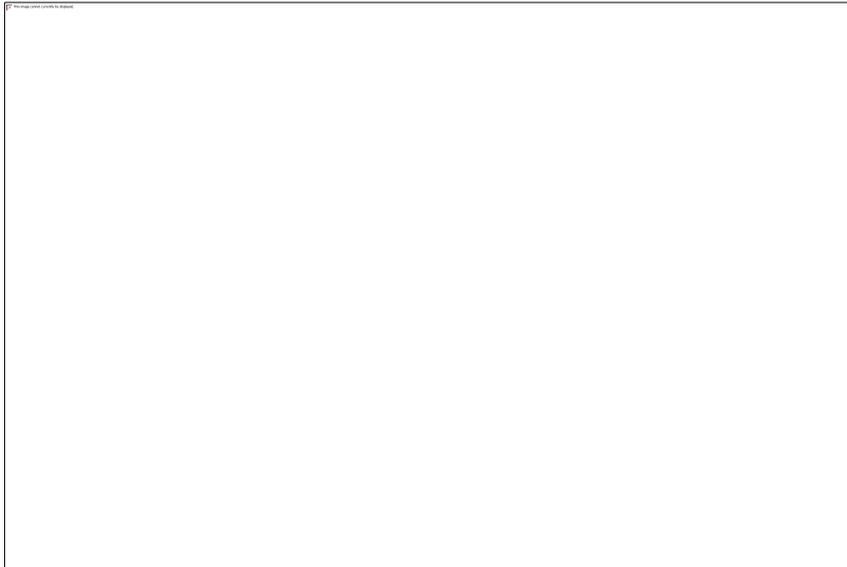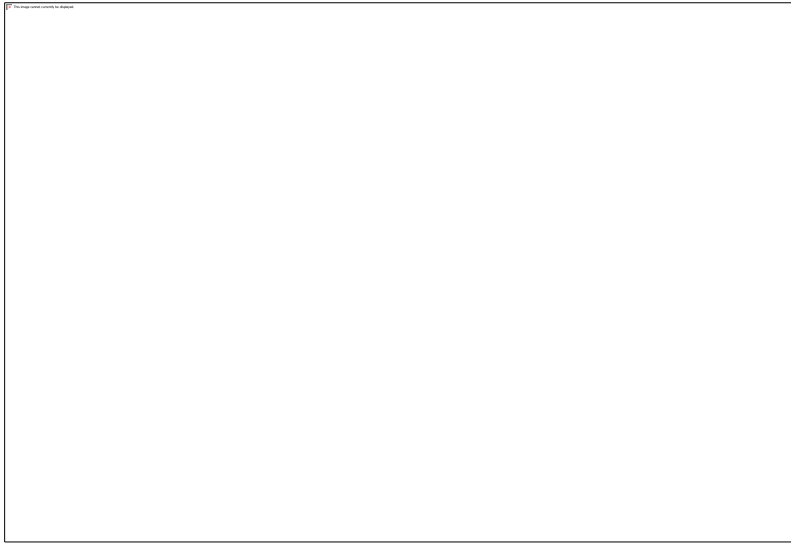
Figure 4. Comparison of computed (red) and measured (black) water surface elevations at Tug Berth for detided tsunami signal (top) and tided (total) signal (bottom) as boundary condition.
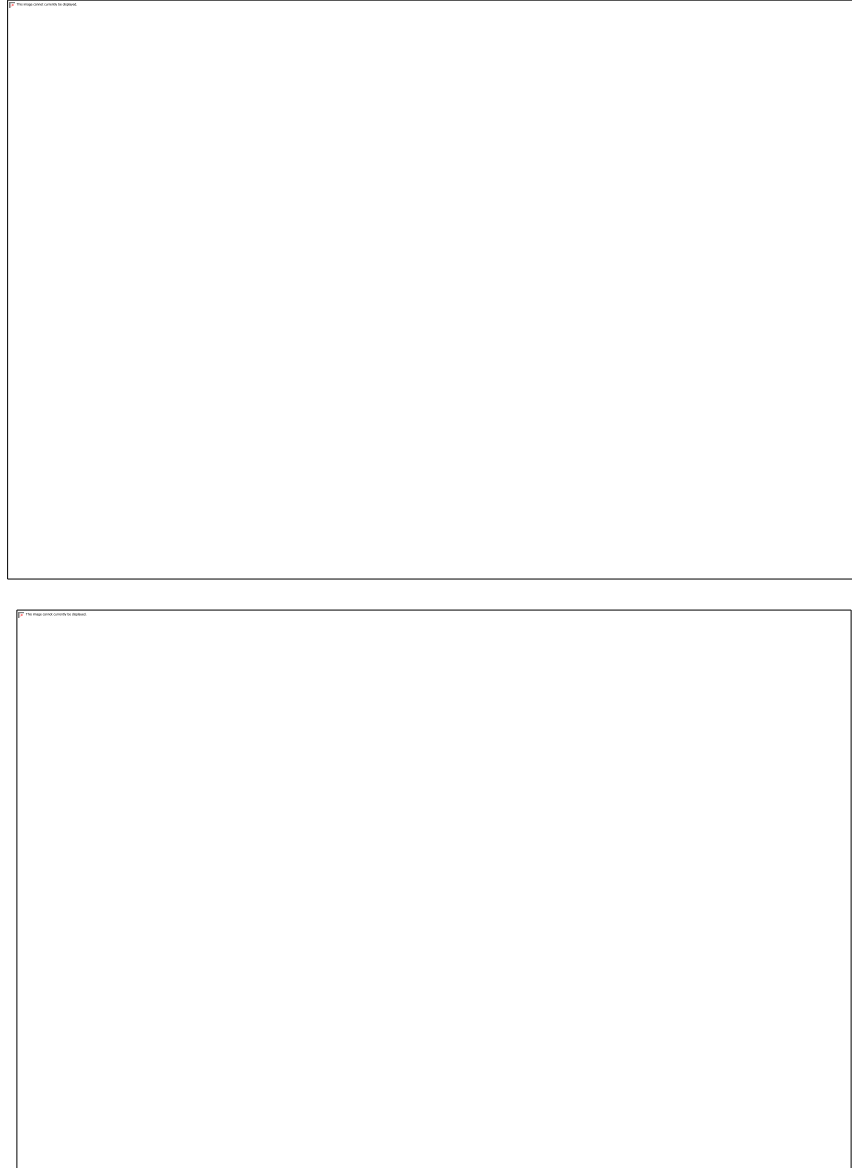
Figure 5. Comparison of computed (red) and measured (black) water surface elevations at Sulfur for detided tsunami signal (top) and tided (total) signal (bottom) as boundary condition.
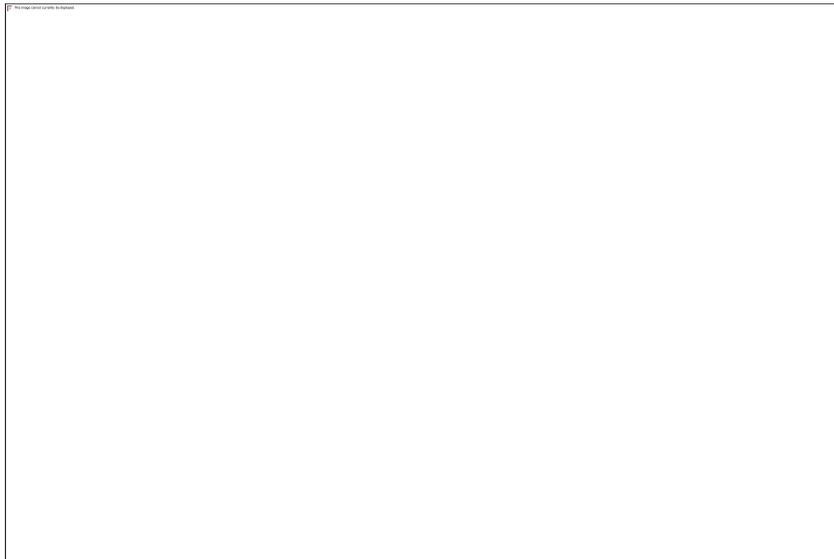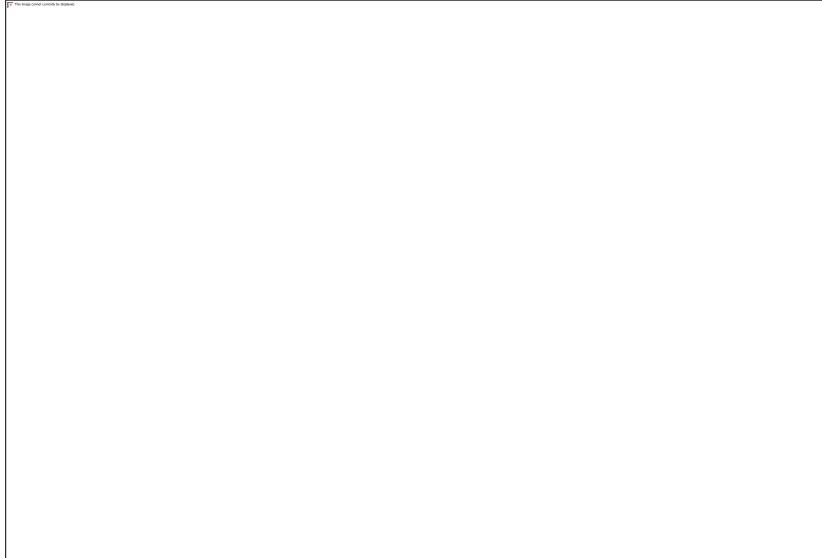
Figure 6. Comparison of computed (red) and measured (black) water surface elevations at Moturiki for detided tsunami signal (top) and tided (total) signal (bottom) as boundary condition.
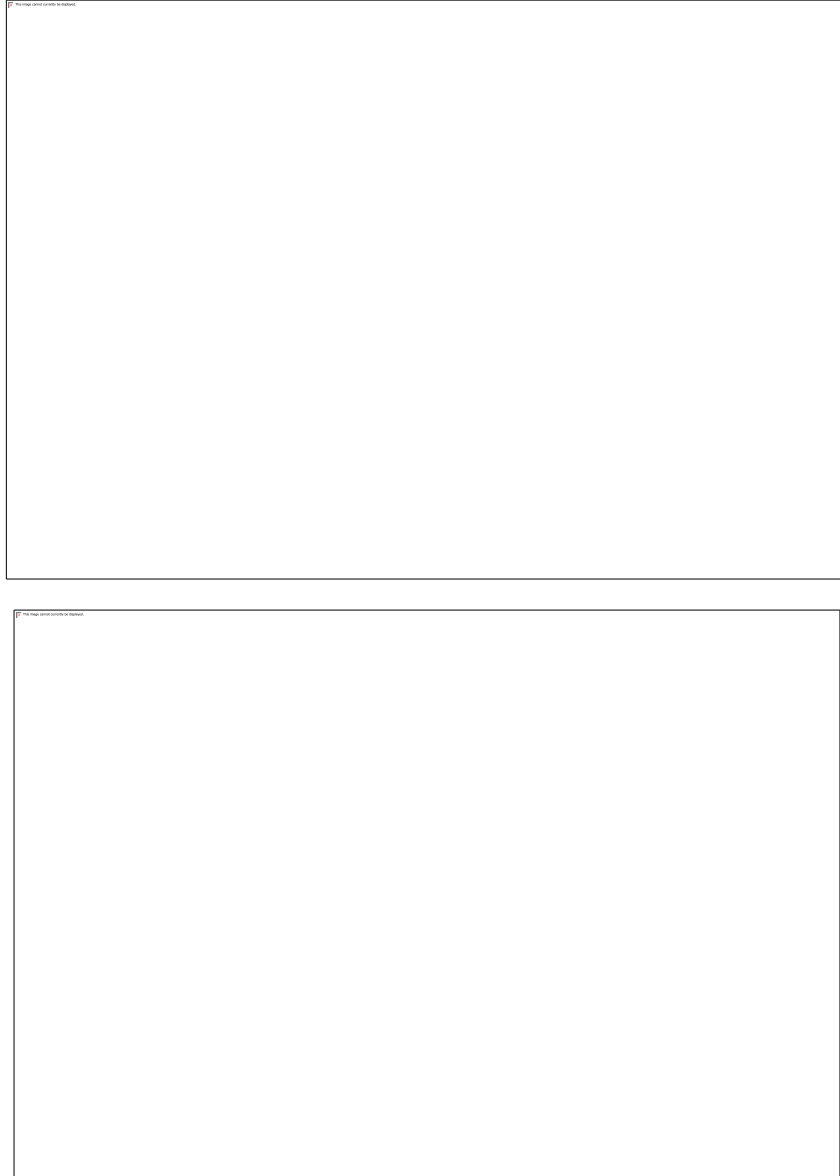
Figure 7. Comparison of computed (red) and measured (black) current speeds at ADCP for detided tsunami signal (top) and tided (total) signal (bottom) as boundary condition.

Figure 8. Comparison of computed (red) and measured (black) velocity component in the E-W direction at ADCP location tided (total) signal as boundary condition.

Figure 9. Comparison of computed and measured component in N-S direction at ADCP tided (total) signal as boundary condition.

4.4 Benchmark Problem #4 Flow through a City Building Layout

This experiment of a single long-period wave propagating up a piecewise linear slope and onto a small-scale model of the town of Seaside, Oregon is presented as benchmark problem. The time series of water surface elevation is inputted from the location from the border (X=18.7m). In the numerical modeling, the grid size and time step are selected as 0.1m and 0.001sec respectively. In Figures 10-13, the comparisons between computed and measured values of flow depth (H), cross

56

shore velocity (u) are given and resultant momentum flux (Hu^2) are compared at the gauge locations B1, B4, B6, and B9.
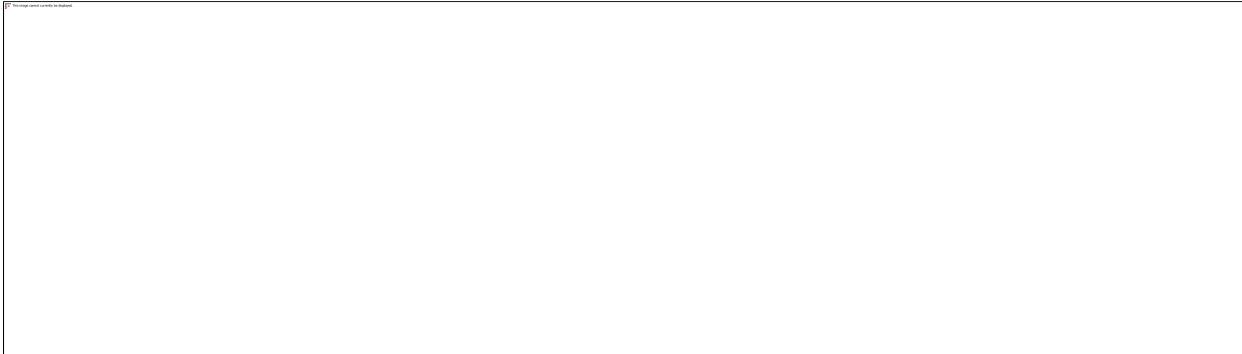
Figure 10. Comparison of computed and measured flow depth (left) and cross shore velocity (center) at gauge B1. Corresponding momentum flux values calculated based on numerical and measured values are compared (right).
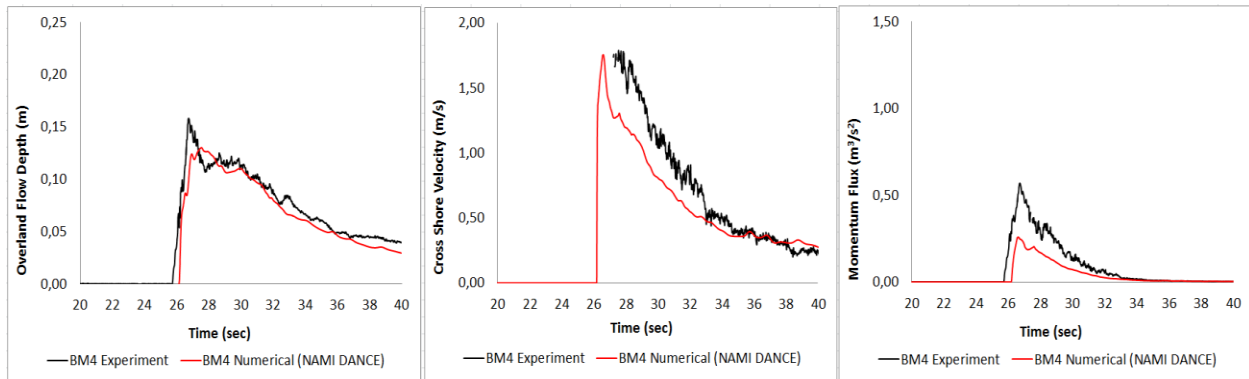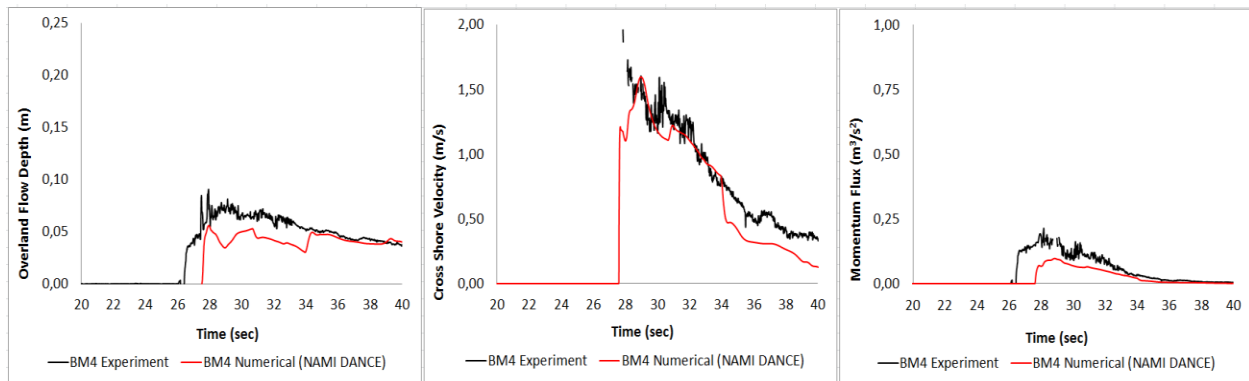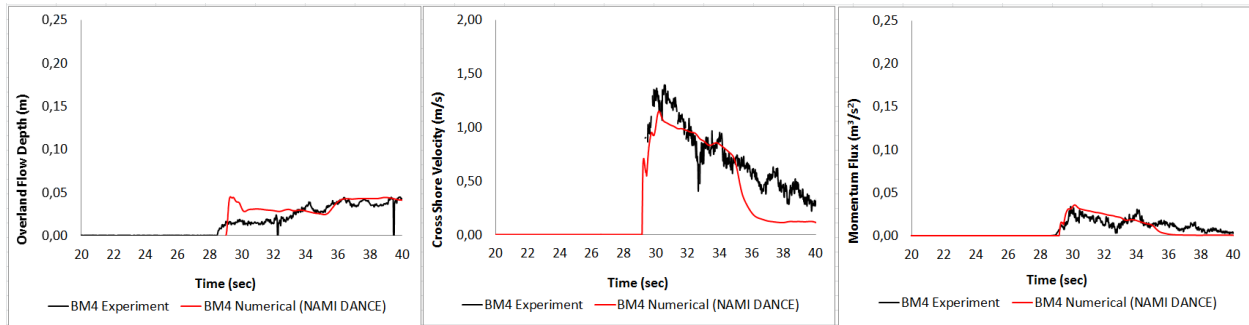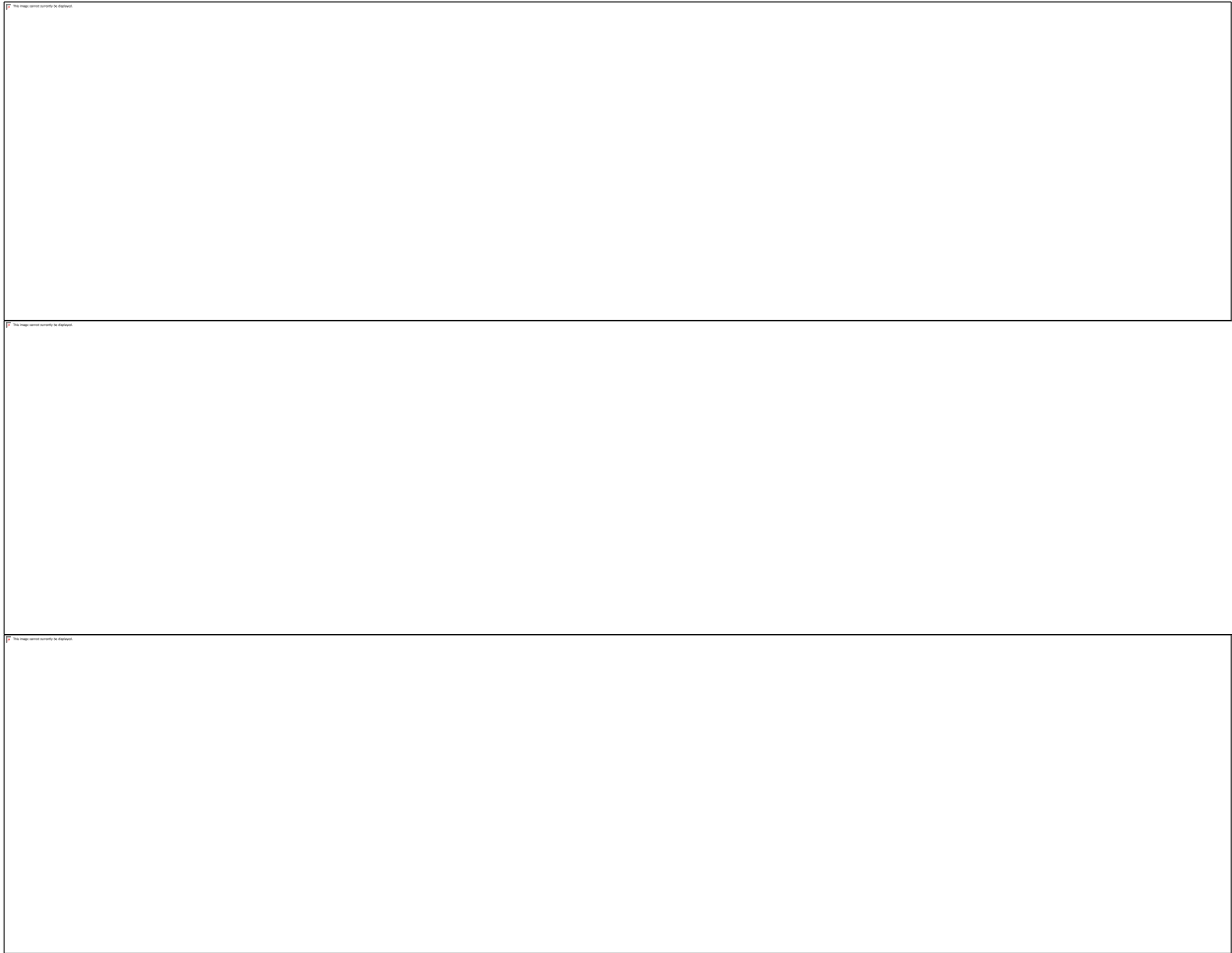

Figure 11. Comparison of computed and measured flow depth (left) and cross shore velocity (center) at gauge B4. Corresponding momentum flux values calculated based on numerical and measured values are compared (right).

Figure 12. Comparison of computed and measured flow depth (left) and cross shore velocity (center) at gauge B6. Corresponding momentum flux values calculated based on numerical and measured values are compared (right).

Figure 13. Comparison of computed and measured flow depth (left) and cross shore velocity (center) at gauge B9. Corresponding momentum flux values calculated based on numerical and measured values are compared (right).

## 4.5 Benchmark Problem #5: Solitary Wave Propagation over a Complex Shelf

This benchmark is on the experiment of a single solitary wave propagating up a triangular shaped shelf with an island feature located at the offshore point of the shelf. Free surface information was recorded via resistance-type wave gauges and sonic wave gages. Velocity information was recorded via ADV's. In the simulations the grid size and time step are selected as 0.05m and 0.0005sec respectively. The simulation duration is selected as 30sec. The time series of the wave height is provided to the numerical model from $X=7.5$ from the left border. The computed and measured free surface elevations and mean velocities are presented in (Figures 14-16). The fairly good agreement is observed in majority of the comparisons. The red curves are numerical and black curves are experimental data.

58

Figure 14. Comparison of computed (red) and measured (black) water surface elevations at gauges 2, 3, 6, 7, and 9 (top to bottom).

Figure 15. Comparison of computed (red) and measured (black) mean velocity component u at gauges 2, 3, and 10.
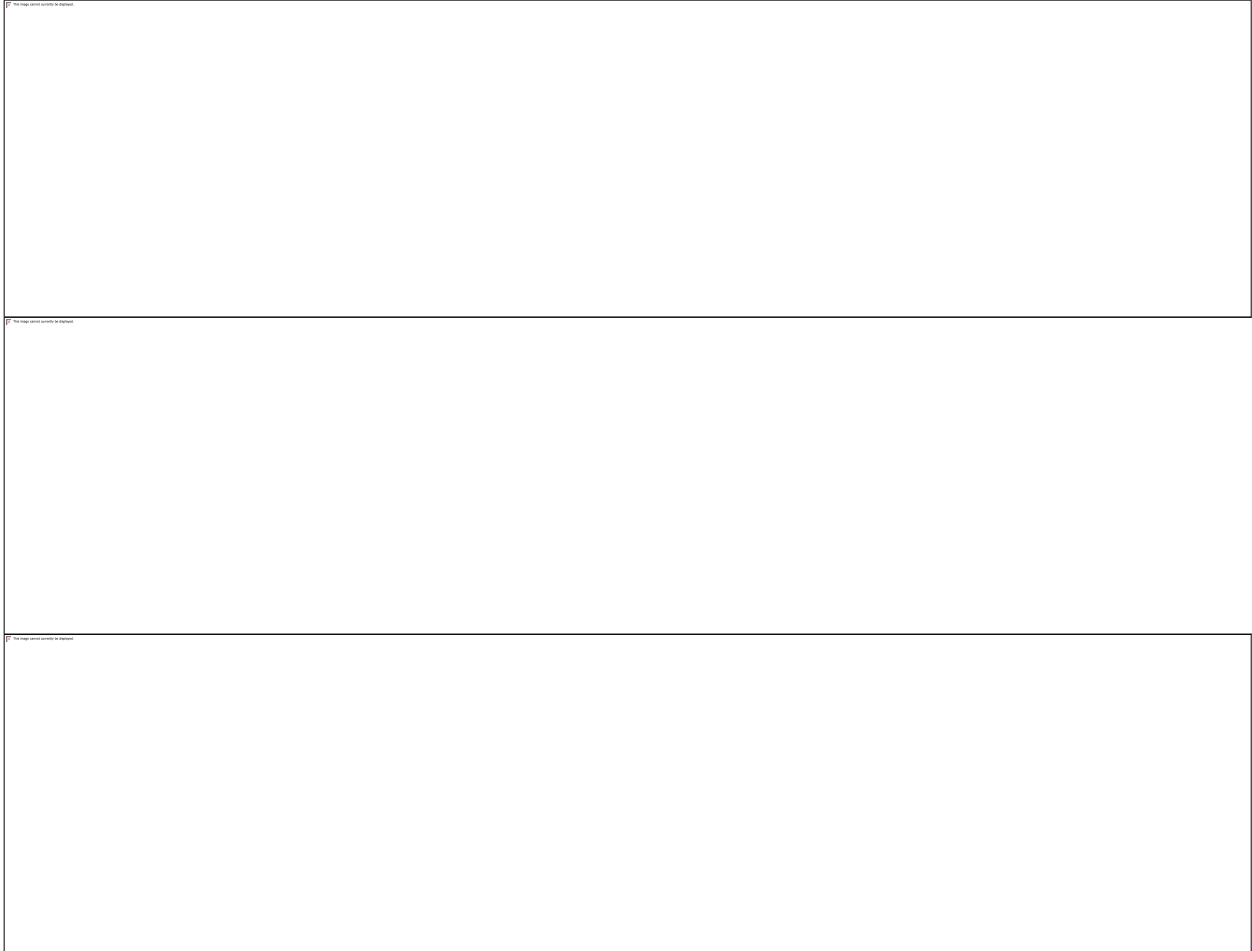
Figure 16. Comparison of computed and measured mean velocity component *v* at gauges 2, 3, and 10.

6　Acknowledgments

References

1. Dao, M. H., & Tkalich, P. (2007). Tsunami propagation modelling − a sensitivity study, Natural Hazards Earth System Sciences, 7, 741−754.

2. Dilmen, D. I., Kemec, S., Yalciner, A. C., Düzgün, S., & Zaytsev, A. (2014). Development of a tsunami inundation map in detecting tsunami risk in Gulf of Fethiye, Turkey. Pure and Applied Geophysics, 172, 921–929. DOI 10.1007/s00024-014-0936-2

3. Heidarzadeh, M., Krastel, S., & Yalciner, A. C. (2014). The state-of-the-art numerical tools for modeling landslide tsunamis: A short review. In S. Krastel et al. (eds.) Submarine Mass Movements and Their Consequences (pp. 483–495). Advances in Natural and Technological Hazards Research 37, Springer International Publishing, Switzerland.

4. Imamura, F. (1989). Tsunami Numerical Simulation with the staggered leap-frog scheme (Numerical code of TUNAMI-N1), School of Civil Engineering, Asian Inst. Tech. and Disaster Control Research Center, Tohoku University

5. Ozer, C., & Yalciner, A. C. (2011). Sensitivity study of hydrodynamic parameters during numerical simulations of tsunami inundation. Pure and Applied Geophysics, Publisher :Springer Basel AG Editor(s): Kenji Satake, Utku Kanoglu, Alexander Rabinovich, Netherlands, 168 (11), 2083–2095.

6. Shuto, N., Goto, C., & Imamura, F. (1990). Numerical simulation as a means of warning for near field tsunamis. Coastal Engineering in Japan. 33, No: 2, 173–193.

7. Sozdinler, C. O., Yalciner, A. C., & Zaytsev, A. (2014). Investigation of tsunami hydrodynamic parameters in inundation zones with different structural layouts. Pure and Applied Geophysics, 172(3-4), 931–952. DOI 10.1007/s00024-014-0947-z

8. Sozdinler, C. O., Yalciner, A. C., Zaytsev, A., Suppasri, A., & Imamura, F. (2015). Investigation of hydrodynamic parameters and the effects of breakwaters during the 2011 Great East Japan Tsunami in Kamaishi Bay. Pure and Applied Geophysics, 2015 Springer Basel DOI 10.1007/s00024-015-1051-8

9. Synolakis, C. E., Bernard, E. N., Titov, V. V., Kânoğlu, U., González, F. (2008). Validation and verification of tsunami numerical models. Pure Applied Geophysics, 165, 2197–2228. DOI 10.1007/s00024- 004-0427-y

10. Yalciner, A. C., Pelinovsky, E., Zaytsev, A., Kurkin, A., Ozer, C., & Karakus, H. (2007a). Modeling and visualization of tsunamis: Mediterranean examples. Tsunami and Nonlinear Waves (Ed: Anjan Kundu), Springer, 2007, 2731–2839.

11. Yalciner, A. C., Synolakis, C. E., Gonzaeles, M., & Kanoglu, U. (2007b). Joint Workshop on Improvements of Tsunami Models, Inundation Map and Test Sites of EU TRANSFER Project, June 11-14, 2007, Fethiye, Turkey

12. Yalciner, A. C., Zaytsev, A., Aytore, B., Insel, I., Heidarzadeh, M., Kian, R., Imamura, F. (2014a). A Possible Submarine Landslide and Associated Tsunami at the Northwest Nile Delta, Mediterranean Sea. Oceanography, 27(2), 68–75.

13. Yalciner, A. C., Gülkan, P., Dilmen, D. I., Aytore, B., Ayca, A., Insel, I., & Zaytsev, A. (2014b). Evaluation of tsunami scenarios for western Peloponnese, Greece. Bollettino di Geofisica Teorica ed Applicata, 55(2), 485–500.

14. Zahibo, N., Pelinovsky, E., Kurkin, A., & Kozelkov A. (2003). Estimation of far-field tsunami potential for the Caribbean Coast based on numerical simulation. Science Tsunami Hazards, 21(4), 202–222.

MOST Benchmark Results

Diego Arcas [a,b]

[a]NOAA Center for Tsunami Research, 7600 Sand Point Way NE, Seattle, WA 98115
[b]University of Washington, JISAO, 3737 Brooklyn Ave. NE, Seattle, WA 98105

Abstract. The Method Of Splitting Tsunamis (MOST) code was adapted and used to simulate all proposed benchmark problems. For problems in a laboratory setting (Problems 1,4 and 5), the computational routine was extracted from the operational code, and was slightly modified to implement boundary and initial conditions exactly as defined in the problem statement. Benchmark problems 1 and 3 were optimized following the recommendations suggested in the problem statements. All other problems were modeled according to the suggested parameter values with minimal to no modifications. Modeled velocity values obtained in almost all problems are in good agreement with the observed data, particularly in the mandatory problems (Problems 1 and 2). Excellent agreement is obtained with the observed data provided for problem 3 and satisfactory amplitude and velocity values are obtained in problems 4 and 5, although a noticeable discrepancy in arrival time is present in some areas of the domain for these two problems. The results obtained in problems 1 and 2 indicate that the current operational version of MOST can adequately forecast tsunami currents, particularly in areas of low vorticity. The model solution in areas of active vortex formation shows high sensitivity to initial and boundary conditions. Modeled velocity results in these areas should be interpreted with caution.

Address all correspondence to: Diego Arcas, Pacific Marine Environmental Laboratory, NOAA Center for Tsunami Research, 7600 Sand Point Way NE, Seattle, WA 98115; Tel: +1 206-526-6216; Fax: +1 206-526-6485; E-mail: diego.arcas@noaa.gov

1   Model Background

The MOST code was originally developed by Titov (1997) at the University of Southern California and was shortly after, adopted by the NOAA Center for Tsunami Research (NCTR) to develop operational, real-time modeling capabilities for NOAA's Tsunami Warning Centers. The code has been validated extensively against laboratory experiments, observational data from real events and analytical solutions (Titov and Synolakis,1995), (Titov and Synolakis 1998). It has also been used to successfully model the benchmark problems proposed in the previous NTHMP inundation benchmarking workshop (Tolkova, 2012). During the past ten years, the MOST code has consistently been used successfully to forecast more than 20 real tsunami events in real time (Wei et al., 2008).

The MOST model provides solutions to the Nonlinear Shallow Water (NSW) equations, including generation, propagation and inundation onto dry land. The operational use of the code in forecasting operations relies, however, in the linearity of the solutions in deep water, (where the wave amplitude is much smaller than the depth) to linearly construct an initial condition based on a pre-computed database of propagation simulations from unit sources (Gica, 2008). Propagation results from the resulting initial condition will conform to observations made by DART® buoys in proximity to the generation area. Nonlinear calculations are performed in real-time and only include shallow coastal areas where nonlinear effects are likely to play a significant role in wave evolution and inundation.

2   Model Equations

The operational version of MOST uses a set of three nested bathymetric and topographic grids to solve wave propagation and inundation in coastal areas. The most external grid has the largest coverage and lowest resolution. The most internal one, where inundation is computed, has the smallest coverage but highest resolution. The extent of a typical external grid covers a rectangular area, several hundred of kilometers in the zonal and meridional directions. Due to the large extent of the external grid, the MOST code uses the NSW equations in spherical coordinates to simulate wave dynamics in the external and intermediate grids, while it solves the Cartesian version of the same equations in the internal grid, which covers a much more reduced geographical extent.
Since three of the five benchmark problems presented in this study require modeling in small scale laboratory settings, and the geographical area covered by the other two full-scale problems is relative small, the Cartesian version of the NSW equations, in a single grid, was implemented for all benchmark problems. Therefore the system solved by MOST in this study is:

$$h_t + (uh)_x + (vh)_y = 0 \qquad\qquad\qquad\text{1.a}$$

$$u_t + uu_x + vu_y + gh_x + C_f g \frac{u|\vec{V}|}{h^{4/3}} = gd_x \qquad\qquad\qquad\text{1.b}$$

$$v_t + uv_x + vv_y + gh_y + C_f g \frac{v|\vec{V}|}{h^{4/3}} = gd_y \qquad\qquad\qquad\text{1.c}$$

Where u and v are the velocity vector $(\vec{V})$ components in the x and y directions respectively, d is the undisturbed water depth, h is the perturbed water depth and C_f is the Manning friction coefficient. Therefore, the only physical bottom dissipation model in the system is a Manning friction term, which, due to the depth-integrated nature of the equations, will act to slow down the entire water-column.

3   Numerical Solution Method

The model uses an explicit scheme to discretize the NSW equations, which requires the limitation of the CFL number to a value smaller than one everywhere on the grid, effectively limiting the size of the computational time step for stability purposes.
The algorithm is based on the method of fractional steps (Yanenko, 1971; Durran, 1999). This method reduces the solution of the 2-D problem, to that of two consecutive 1-D problems in each spatial direction, transforming system (1) into the two systems:

$$h_t + (hu)_x = 0 \qquad\qquad\qquad\text{2.a}$$

$$u_t + u(u)_x + gh_x + C_f g \frac{u|\vec{V}|}{h^{4/3}} = gd_x \qquad\qquad\qquad\text{2.b}$$

$$v_t + u(v)_x = 0 \qquad\qquad\qquad\text{2.c}$$

and

$$h_t + (hv)_x = 0 \qquad\qquad\qquad\qquad \text{3.a}$$

$$v_t + vv_y + gh_y + C_f g \frac{v|\vec{V}|}{h^{4/3}} = gd_y \qquad\qquad\qquad\qquad \text{3.b}$$

$$u_t + vu_y = 0 \qquad\qquad\qquad\qquad \text{3.c}$$

These two resulting systems are transformed into characteristic form before discretization, by applying the following variable transformation:

$$\boxed{} , \boxed{} , \boxed{} , \boxed{} , v = v', \boxed{}$$

System 2 becomes:

$$p_t + \lambda_1 p_x = gd_x - C_f g \frac{u|\vec{V}|}{h^{4/3}}$$

$$q_t + \lambda_2 q_x = gd_y - C_f g \frac{u|\vec{V}|}{h^{4/3}}$$

$$v'_t + \lambda_3 v'_x = 0$$

A similar system in the y-direction results from the transformation of system 3 to characteristic form. These two final systems are discretized using a coastal second order in space, first order in time differencing scheme described in Burwell et al., 2007. Burwell's work also describes in detail the numerical sources of error associated with the discretization scheme of the code. In general terms their study concluded that for a specific spatial harmonic, numerical dissipation in MOST will depend on grid resolution and time step size. Numerical dissipation in MOST will be largest when the CFL number is close to a critical value of 0.7, reducing its severity as CFL values move towards either 1 or 0. Reducing CFL has the advantage that it minimizes dissipation for a larger range of wavenumbers, however, a larger number of time steps are necessary to model a specific length of time.

The use of a central difference scheme in interior grid points requires special treatment of nodes at the wet/dry boundary. To handle this situation, the code creates an auxiliary grid node at the shoreline by horizontally projecting the water level at the last wet node onto a linearly sloping beach. This auxiliary node is used as the right (alt. left) neighboring node in the central discretization of the last wet node. The variability in the position of the new auxiliary point requires the use of variable grid spacing in the discretization scheme and some modification to this approach if the position of the auxiliary point violates CFL. Once the last wet node has been computed, the auxiliary point is eliminated. The updated water elevation and velocity values at the last wet node determine whether flooding progresses to the neighboring dry node or water recedes causing the last wet node to become dry.

4 Benchmark Problem Comparisons

4.1 Benchmark Problem #1: Steady Flow over Submerged Obstacle

Three different friction configurations were used in the simulation of Benchmark problem 1: constant friction throughout the domain, no friction and variable friction. The same grid was used for all cases, with numerical influx and outflow boundary conditions implemented along the left and right vertical walls of the domain respectively, and reflective boundary conditions along the two horizontal walls. Although part of the domain upstream from the obstacle could have been shortened without significant impact on the results, computational times were short enough that simulations were performed in the full domain. The grid used in all setups, therefore, covers the entire laboratory domain specified by the bathymetric data provided with the problem, the spatial step used in both the x and y directions was 0.01 m for a total grid size of 985 x 153 nodes. Simulations were run for a total of 240 s, which in most cases proved to be more than sufficient time for the initial transient response to vanish and the system to settle onto a periodic steady state. A time series interval of approximately 80 s was extracted from the steady state signal of the two velocity components at the two specified sample points.

The first case was modeled using a Manning coefficient of 0.01 $s/m^{1/3}$ as specified in the problem statement. After transients vanished, the flow settled onto a quasi-periodic state with active vortex shedding and an irregular Karman vortex street forming in the wake of the obstacle. The second setup was the inviscid case (Manning coefficient=0.0). Results of the simulation show the flow settling onto a steady state with two main recirculating vortices behind the obstacle and minor vortex shedding from the tip of the obstacle closest to the water surface. The third case was optimized using a Manning friction coefficient of 0.01 $s/m^{1/3}$ everywhere on the channel and 0.0173 $s/m^{1/3}$ on the surface of the obstacle. After the flow settles onto a periodic state, a symmetric and periodic vortex shedding pattern in the wake of the obstacle is observed. Time series from this optimized case were extracted, plotted against observations and shown in Figure 1. Dominant period, average amplitude and mean values were computed with the third configuration for different combinations of Manning coefficients in the channel and on the obstacle. All cases showed good agreement with observations, with the selected optimized case showing the best correlation. Mean values of the horizontal velocity component at sample point 1, however, seemed to be consistently underestimated for all combinations of Manning coefficients.

Figure 7. Experimental data (dots) and numerical simulation (solid line, not shown) for a) U velocity component at time series location 1, b) V velocity component at time series location 1, c) U velocity component at time series location 2, and d) V velocity component at time series location 2.

4.2 Benchmark Problem #2: Tsunami Currents in Hilo Harbor

The code setup for problem 4 was very similar to that of the standard operational code, with the only difference that the simulation was performed on a single grid, in Cartesian coordinates. Boundary conditions along grid edges are open boundary, with influx conditions not directly imposed but interpolated from a predefined external grid file. The simulation was forced along the northern grid boundary with the provided time series at the Control Point shifted to by -15.6 min to account for the wave travel time from the boundary of the grid to the Control Point location. This causes some distortion to the wave amplitude signal as it travels from the northern boundary to the Control Point, however, this distortion is minimized by the fact that all depths equal to or deeper than 30 m in the provided Digital Elevation Model (DEM) were set to 30 m, effectively flattening the sea floor along the path of the input waveform between the northern grid boundary and the Control Point. As requested, three cases were simulated using this configuration at approximately 20 m, 10 m and 5 m resolution, all using the prescribed Manning coefficient of n=0.025.

The computed water elevation time series at the Control Point and tide gauge location were compared with provided data for all three cases. In addition, the two velocity components at the

two ADCP locations HA1125 and HA1126 were compared with recorded values and maximum elevation and current speed values in the entire grid were plotted and inspected against one another at all three resolutions for convergence. Results of all three simulations show excellent agreement between computed and provided time series at the Control Point, and satisfactory agreement with recorded tide gauge free surface elevation and ADCP velocity values. Results from all three simulations showed almost negligible variability in the water elevation solution at different grid resolutions, indicating solution convergence. The velocity solution exhibited a small, but slightly larger variability among all three resolutions, than in the case of water elevation. These results seem to indicate that for this particular problem, both the water elevation and current velocity solutions are well-resolved, but that, in general, one might expect a need for higher resolution for current velocity to be converged than for wave elevation. Further inspection of the maximum current speed plots showed that most of the variability in the solution seems to be concentrated in areas of strong vorticity.

Figure 8. Measured data (dashed line) and numerical simulation (solid line) at the harbor tide gage (top), HA25 ADCP (middle), and HA26 ADCP (bottom).

Figure 9. Maximum predicted fluid speed during entire duration of the 10-m resolution simulation.

4.3 Benchmark Problem #3: Tsunami Currents in Tauranga Harbor

A similar code setup to that used in Problem 2 was implemented for two different cases in Problem 3; a) simulation of tsunami alone and b) simulation of tsunami combined with tide. Open boundaries were implemented along all grid boundaries with the provided "incident" time series driving the simulation along the northern boundary. Velocity boundary conditions were inferred from the wave elevation solution, using the one-dimensional linear approximation ($u = \eta \sqrt{\frac{g}{h}}$) along the northern boundary, for the case of tsunami alone. In the case of tsunami +tide combination, the data provided show a phase shift between wave elevation and current speed signals that invalidates the use of the linear approximation to infer velocity boundary conditions. Therefore, velocity components were set to zero along the northern boundary. All simulations were performed on the provided DEM sub-sampled to 20 m. A Manning friction coefficient of 0.02 s/m$^{1/3}$ was used in all simulations. In the combined case of tsunami+tide initial values of wave elevation and current speed in the interior of the domain were set to zero. To avoid large discontinuities between values at the boundaries and interior of the grid at time zero, the simulation was initiated at the first zero-crossing of the tidal time-series.

Water elevation and current speed time series were extracted at all sample points where data were provided. Computed wave elevation and current speed values show extremely good agreement with the observational data in the case of tsunami alone at all sample locations. Figure 4 shows comparisons at Tug Berth, Sulphur Point, Moturiki and current speed at the ADCP sample points. Computed values of wave elevation were also in extremely good agreement with observations in the case of tsunami+tide, however, current speed results for this second case tend to underestimate observed values for the tidal component of the signal as seen in Figure 5. This deficiency is most probably due to the lack of knowledge about velocity initial and boundary conditions along grid boundaries when tidal effects are included. A quick analysis of the accuracy of the results suggests that accurate calculation of the velocity solution, particularly when large tidal currents are present will require some a priori knowledge of tidal velocity boundary conditions.
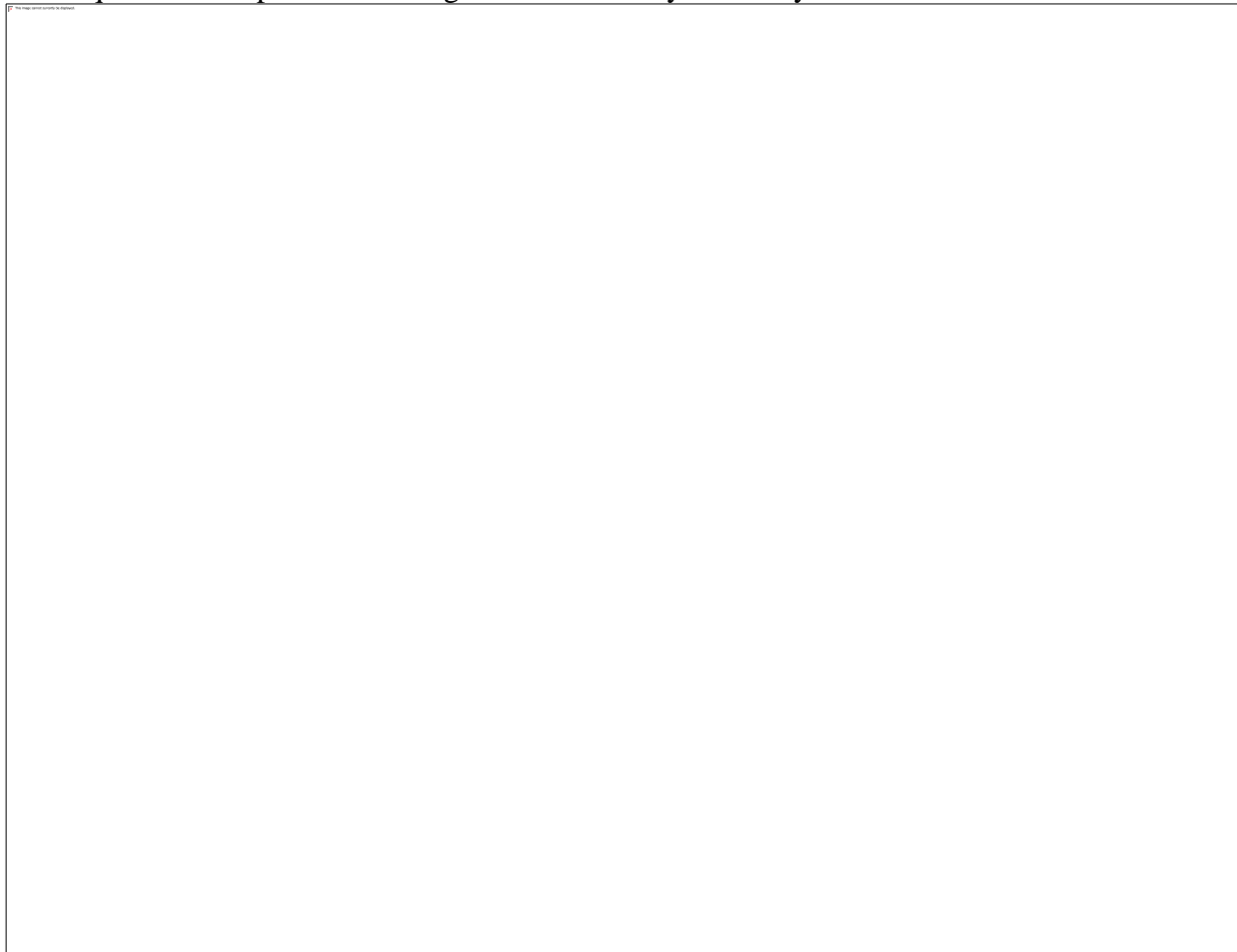
Figure 4. Comparison of wave elevation (top panels) and current speed (bottom panel) at 4 different locations inside, outside and at the Tauranga Bay entrance, for the tsunami only case.
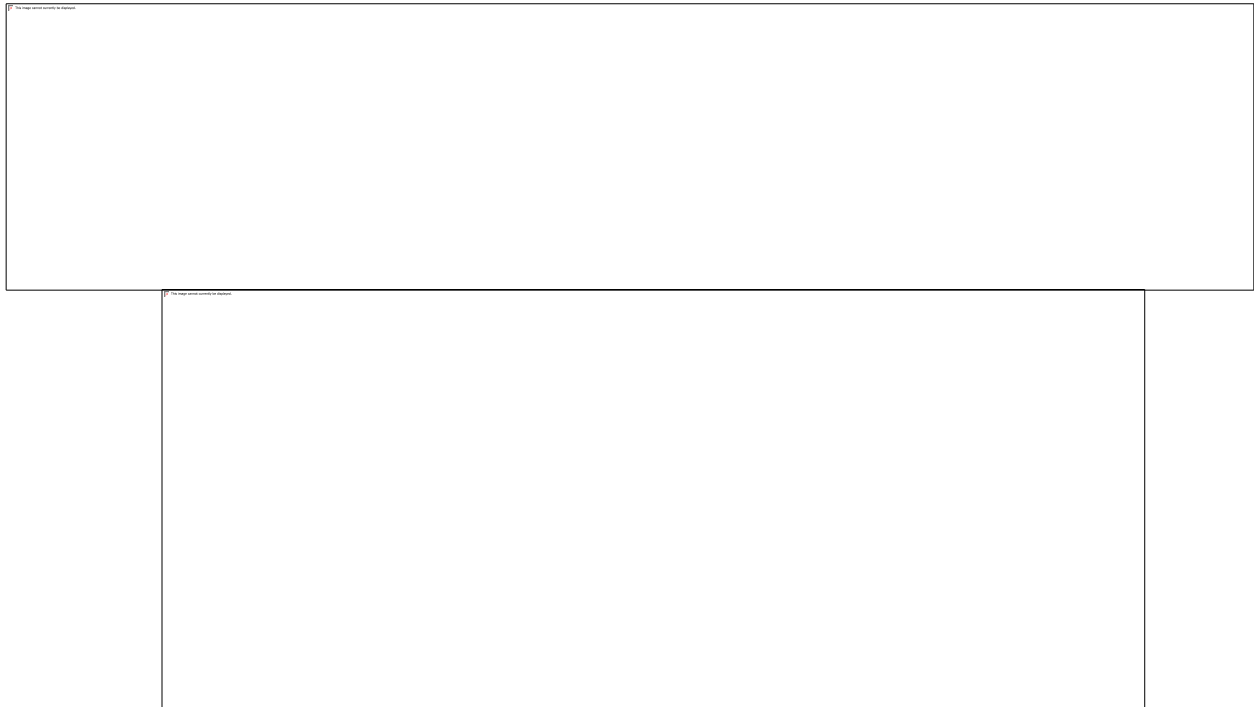
Figure 5. Comparison of wave elevation (top panels) and current speed (bottom panel) at 4 different locations inside, outside and at the Tauranga Bay entrance, for the tsunami+tide case.

4.4 Benchmark Problem #4: Flow through a City Building Layout

A numerical setup similar to that used in Problem 1 was used to simulate Problem 4 at laboratory scale. Open or reflective boundary conditions along grid boundaries were appropriately defined to mimic the laboratory setup. The simulation was driven by the incident wave time series provided with the problem statement. Since the incident wave signal was recorded at a distance x=5 m in the laboratory setting, the bathymetry DEM was cropped to discard the initial section between x=0 m and x=5 m. With this adjustment, the incoming wave was introduced into the domain exactly at the location where it was recorded. Velocity boundary conditions were specified along the input boundary so that the outgoing Riemann invariant remains consistent with that of the incoming invariant as long as no reflected waves are leaving the domain through this boundary (Tolkova, 2012) (Mei, 1983). A Manning friction coefficient of 0.025 s/m$^{1/3}$ was used to account for dissipative effects. Despite, the strong non-linearity of the incident wave, grid resolution was set to match the local depth along the x-direction, up to a depth of 0.1 m, in an attempt to match physical dispersion (Burwell et al., 2007).

Results of the simulation show excellent agreement between the recorded and computed wave forms at x=18.618 m (Figure 6, top panel) for both, the first wave and reflected wave-train, although the amplitude of the reflected waves is underestimated by the model, suggesting too much dissipation in the computed results. Figure 6 (lower panel) also shows an instant of the simulated results at t=35.1 s with the red dots indicating the location of the dry-land sample points. Figure 7 shows comparisons of flow depth, velocity and specific momentum flux at four different stations in the runup part of the domain. In general, computed results show good agreement with observations in wave amplitude, although with significant discrepancy in wave front propagation speed overland, resulting in substantial mismatch of computed and observed arrival times at dry land sample stations. This delay increases away from the shoreline and is maximum at the last sample point at station x=40.68 m.
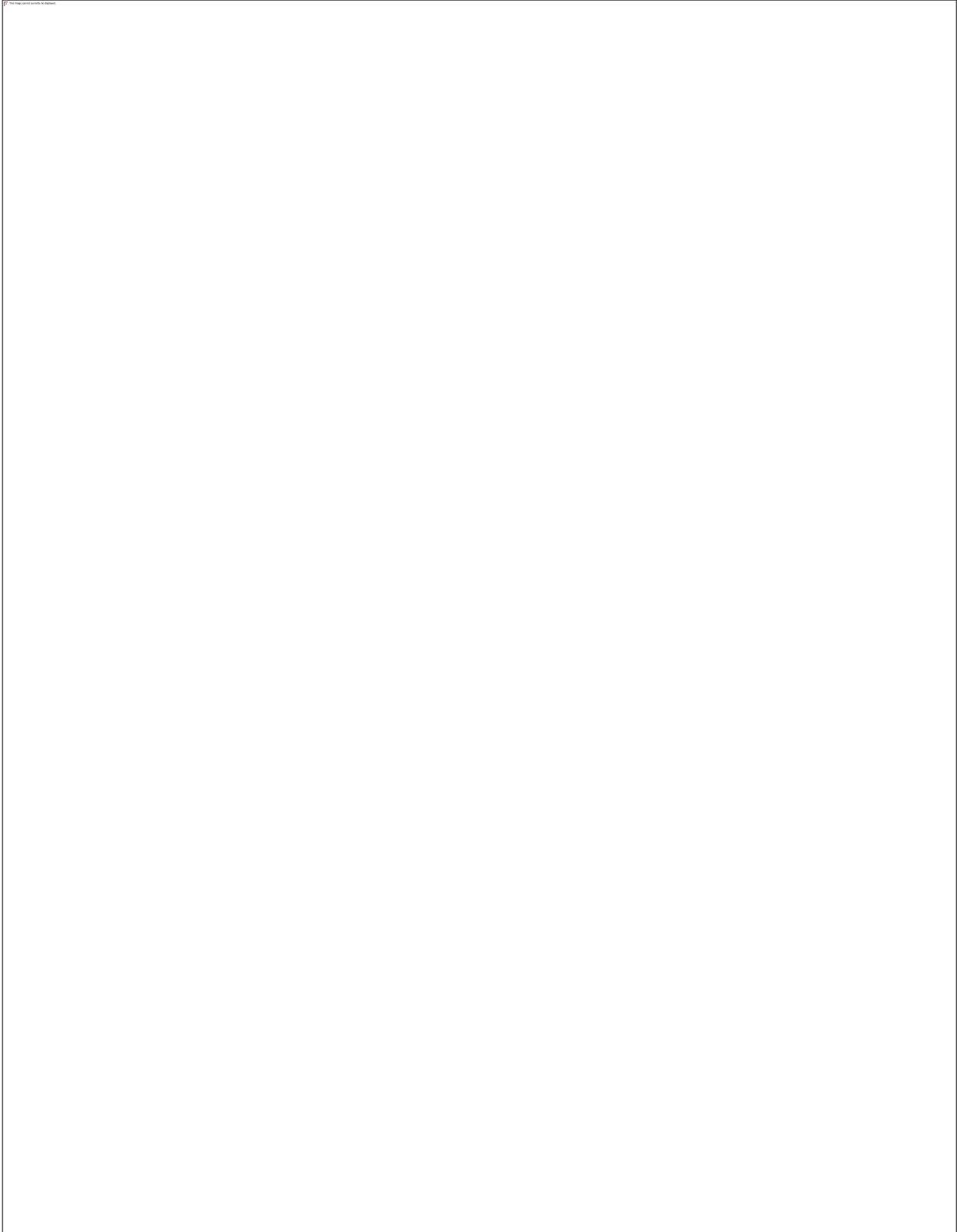

Figure 6. Comparison of computed and recorded wave elevation at the Control Point (top panel) and numerical set up with red dots showing the locations of the sample point locations (bottom panel).
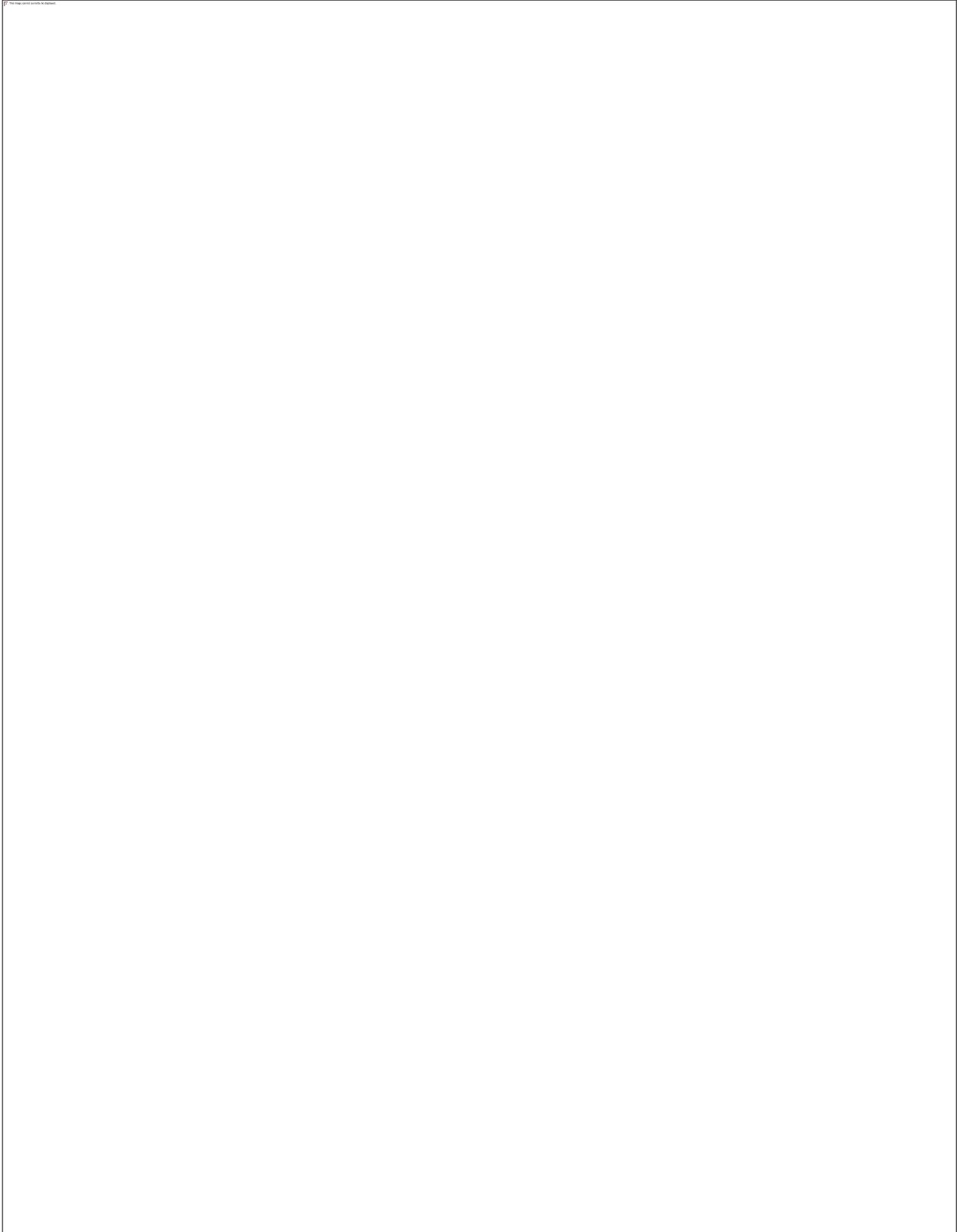
Figure 6. Comparisons computed and recorded wave elevation (left column), cross-shore velocity (center column), and cross-shore momentum flux (right column) at 4 dfferent sample points.

4.5 Benchmark Problem #5: Solitary Wave Propagation over a Complex Shelf

Even though most of the data provided for comparison, including turbulence measurements, was not relevant in the case of depth integrated models such as MOST, Problem 5 was also attempted using a similar numerical setup to that of Problems 1 and 4. The goal of the use of MOST in simulating this problem is to compare overall wave dynamics in an average sense. As in the case of Problem 4, boundary conditions were hard-coded into the computational routine. The computational domain extended from x=7.5 m to x= 43.5 m in the cross-shore direction and from y=-13.21 m to y=13.1 m in the long-shore direction. The recorded time series at x=7.5 m, y=0.0 m was used to force the model. The incident wave time series was forced through the left boundary with velocity boundary conditions inferred similarly to those in Problem 4. Due to the 2-dimensional nature of the bathymetry and the strong non-linearity of the input wave, no attempt was made to match numerical to physical (linear) dispersion. A uniform grid with dx=dy=0.0438 m was used, resulting in a total grid size of 603x823.

74

Figure 7. Comparison of computed and average recorded velocity components at three different sample points.

Figure 8. Comparison of computed and recorded wave elevation at nine different sample points.
.

Computed, depth-averaged time series of velocity components were compared with the observed signal at three stations located in front of the conical island along the center line of the domain, (x=13.0 m, y =0.0 m, z=-0.03m) behind the island, along the center line and close to the surface (x=21.0 m, y =0.0 m, z=-0.01m) and offset from the centerline (x=21.0 m, y =-5.0 m, z=-0.01m) (Figure 7). Results show very good agreement with observed time series in front of the island as well as behind the island and offset from the centerline. Comparison of the u velocity component at the gauge located on the centerline, immediately behind the island shows the most deficient correlation. However, good agreement between computed and observed measurements was observed at the other stations. This good comparison is remarkable if one takes into account the presence of a certain level of uncertainty in the observational data. For instance, an unjustified positive initial value of the v velocity component along the centerline, immediately in front of the island is observed in the data provided. Additionally, the computed free surface elevation was compared with observations (Figure 8) at all nine different locations where data were provided. Wave elevation data show very good agreement in amplitude at all gages, however, there is an arrival time delay in the model signal at gages located in the wake of the island, probably due to the Manning friction coefficient (0.025 s/m$^{1/3}$) being too large.

5 Conclusions

Model results show excellent correlation with both water level elevation and current speed observations for Problems 1, 2 and 3, with minimal optimization. In the case of Problem 1, active, well-organized, periodic vortex shedding was observed in simulations with the use of a spatially varying Manning friction coefficient. Quantitative comparison with provided velocity components confirms good accuracy in the computed results when comparing shedding frequency, amplitude and mean level of the signal to observations. The horizontal velocity component, u velocity component behind and along the centerline of the island, seems to be noticeably underestimated. In Problem 2, the grid convergence study proposed in the problem statement, reveals a high level of convergence in both the water elevation and current speed even at the coarsest grid resolution of 20 m. This is confirmed by comparisons with recorded values at the tide gage and ADCP locations. The model, however, exhibits some variability in the current speed solution in areas of active vorticity generation, near walls or during runup. This variability is present even at the highest grid resolution of 5 m suggesting a very high sensitivity of the vorticity field to grid resolution and most likely to other computational parameters as well. Problem 3 was simulated with and without tidal effects. In the case with no tide, water elevation values at all stations show excellent comparison with observations. Comparison of current speed and individual velocity components with observations is also good, although slightly underestimated. Simulation results including tidal interaction also show very good correlation between the recorded and computed total wave elevation at all stations. Capturing the correct tidal velocity and, in particular, tidal velocity components seems to be a more challenging task, hindered by the fact that accurate boundary conditions for tidal currents were not provided and, in general, they are hard to obtain. Despite, these difficulties, a very good approximation to the total velocity signal was obtained after optimization.

Results for Problems 4 and 5 were not optimized. For both problems, fine-tuning of some of the code parameters to run in laboratory scale configurations may be necessary, particularly in the run-

up algorithm, which may otherwise result in noisy run-up. As a way to mitigate this problem, a relatively high Manning friction coefficient of 0.025 s/m$^{1/3}$ was used in both Problems, which may have resulted in slow propagation speed, particularly during runup, as reflected in arrival time discrepancies between model and observations at some of the gages. In the case of Problem 5, only averaged values of velocity components could be compared due to the depth-integrated nature of the MOST code, however, except for the already mentioned arrival time delay at some of the stations, comparison with mean results is quite acceptable.

6 Acknowledgments

References

1. Burwell, D., Tolkova, E., and Chawla, A., "Diffusion and dispersion characterization of a numerical tsunami model. *Ocean Modelling"*, *19*(1–2), 10–30, (2007).

2. Durran, D. R., *Numerical Methods for Wave Equations in Geophysical Fluid Dynamics*, Springer-Verlag, New York, Berlin. (1999).

3. Gica, E., Spillane, M., Titov, V.V., Chamberlin, C. and Newman J.C., "Development of the forecast propagation database for NOAA's Short-term Inundation Forecast for Tsunamis (SIFT). NOAA Tech. Memo. OAR PMEL-139, 89 pp. (2008).

4. Mei C. C., "The Applied Dynamics of Ocean Surface Waves" John Wiley & Sons, New York, Chichester, Brisbane, Toronto, Singapore. 740 pp. (1983).

5. Titov, V. V., Modeling of breaking and nonbreaking long-wave evolution and runup using VTCS-2, *J. Waterw. Port Coast. Ocean Eng.* 121(6), 308-316 (1995).

6. Titov, V. V., *Numerical Modeling of long wave runup,* PhD thesis, University of Southern California, Los Angeles, CA. (1997)

7. Titov, V.V., and Synolakis, C.E., Numerical modeling of tidal wave runup. *J. Waterw. Port Coastal Ocean Eng., 124*(4), 157–171 (1998)

8. Tolkova, E., "MOST (Method of Plitting Tsunamis) Numerical Model", in Proceedings and Results of the 2011 NTHMP Model Benchmarking Workshop. NOAA Special Report, 212-238 (2012).

9. Wei, Y., Bernard, E., Tang, L., Weiss, R., Titov, V., Moore, C., Spillane, M., Hopkins, M. and Kânoğlu, U., Real-time experimental forecast of the Peruvian tsunami of August 2007 for U.S. coastlines. *Geophys. Res. Lett.*, *35*, L04609, doi: 10.1029/2007GL032250 (2008) .

10. .Yanenko, N. N. "The Method of Fractional Steps." (Translated from Russian by M. Holt), Springer, New York, Berlin, Heidelberg. (1971).

Cliffs Benchmark Results

Elena Tolkova,[a]

[a]NorthWest Research Associates, 4118 148th Ave NE Redmond, WA 98052-5164, USA

Abstract. Cliffs (an open source modification of MOST) was exercised with five Benchmark Problems offered by NTHMP for its modeling Workshop on Tsunami Currents, Portland, Feb.9-10, 2015: two field cases, and three lab experiments. Cliffs performed in robust and accurate manner in all cases, but one lab BP. Cliffs performed best with simulating the 2011-Tohoku event in Tauranga harbor, New Zealand. This field BP stands out in that not only the model output is being compared to the observations, but the model input is also dictated by the real-world measurements. Under these settings leaving no uncertainty in both input and output, Cliffs reproduced the wave dynamics very accurately. Cliffs was least successful with simulating an inundation of the scaled lab model of the town of Seaside, OR, where it significantly under-estimated flow depth over land. The latter might be a consequence of the model's excessive numerical dispersion and dissipation at the time scales too short for the real-world scenarios. Two field BPs highlighted an important difference between interpreting modeling results with respect to wave height and with respect to current.

Address all correspondence to: Elena Tolkova, NorthWest Research Associates, 4118 148th Ave NE Redmond, WA 98052-5164, USA; E-mail: e.tolkova@gmail.com

1   Model Background

Cliffs is an open-source relative of MOST (Method Of Splitting Tsunamis) numerical model. Cliffs is developed, documented, and maintained in a GitHub repository by E. Tolkova. Cliffs computes tsunami propagation and land inundation under the framework of non-linear shallow-water theory. Cliffs uses 1D finite-difference approximation VTCS-2 (Titov and Synolakis, 1995) or, presently, its modification (Tolkova, 2015) combined with dimensional splitting for solving in two spatial dimensions (Strang, 1968; Titov and Synolakis, 1998; Titov and Gonzalez, 1997). Cliffs inundation algorithm is based on a staircase representation of topography and treats a moving shoreline as a moving vertical wall (a moving cliff), which gave the model its name.

The flow of the computations and input/output data types are similar to that in MOST version 4, which was developed as an adaptation of a curvilinear version of the MOST model (Tolkova, 2008) to spherical coordinate systems arbitrary rotated on the Globe. For the present Cliffs version, the computational flow of MOST-4 has been optimized to focus specifically on geophysical and Cartesian coordinate systems. Cliffs code was written in 03/2013-09/2014, and has been occasionally revisited thereafter. Cliffs is a developing model, and its GitHub version might deviate from the description given in the model's birth certificate (Tolkova, 2014). The model description is periodically updated in Cliffs User Manual.

Cliffs development started with a seemingly minor change to the reflective (vertical wall) boundary condition in VTCS-2/MOST models, which re-positioned the reflective boundary from a point immediately next to the edge wet node (the center of the edge wet cell) to a cell interface between wet and dry nodes. This change allowed to reduce numerical dissipation on reflection (which resulted in better match between observations and simulations of the 2011-Tohoku tsunami), and to replace VTCS-2/MOST runup routine with another inundation algorithm. Cliffs has been tested, and performed well, with the complete set of NTHMP-selected benchmark

problems (NTHMP, 2011) focused on inundation, such as runup of breaking and non-breaking solitary waves onto a sloping beach; runup on a conical island; simulation of a lab experiment with a scaled model of Monai Valley; and simulation of the 1993 Hokkiado tsunami and inundation of the Okushiri Island. A later modification to the original VTCS-2 difference scheme resulted in slightly better performance with some inundation tests.

2   Model Equations

Cliffs solves the non-linear shallow-water equations (SWE) given below in matrix notation in the Cartesian coordinates:

$$\qquad\qquad\qquad\qquad\qquad\qquad\qquad\qquad\qquad\qquad\qquad\qquad\qquad\qquad\qquad\qquad (1)$$

where subscript denotes partial derivatives; $W = (h\ u\ v)^T$ is a vector of state variables; h is height of the water column; u, v are particle velocity components in x and y directions;

$$\qquad\qquad\qquad\qquad\qquad\qquad\qquad\qquad\qquad\qquad\qquad\qquad\qquad\qquad\qquad\qquad (1)$$

g is acceleration due to gravity; $(\alpha^x\ \alpha^y)$ are the components of acceleration due to friction; d is undisturbed water depth, or vertical coordinate of sea bottom measured down from the mean sea level (MSL). Negative values of d correspond to dry land and give the land elevation relative to MSL. In Manning friction formulation $(\alpha^x\ \alpha^y) = n^2 g\sqrt{u^2 + v^2}/h^{4/3}$, where n is Manning's roughness coefficient.

3   Numerical Solution Method

Like MOST, Cliffs solves the SWE following an efficient numerical method by Titov and Synolakis (1998). First, by making use of dimensional splitting, the original 2D problem becomes a sequence of 1D problems for the same state variables, to be solved row-wise and column-wise in an alternate manner. Next, by transitioning to Riemann invariants, each 1D problem becomes three independent convection problems for a single variable each. Note, that this numerical formulation does not allow emptying a cell, because the flow depth h relates to Riemann invariants p, q as $h = (p - q)^2 / 16g$ and cannot therefore run through zero. The difference scheme to solve each problem possesses significant numerical dispersion, which can be used to imitate physical dispersion. Numerical dissipation is greater for shorter waves, and reaches its peak (for all wavelength) at Courant number 0.707 (Burwell et al., 2007). The scheme is first-order accurate in time and second-order accurate in space for a uniform grid spacing. It allows varying grid spacing Δx_j, but should the spacing vary, an added numerical error of order $\Delta x_j - \Delta x_{j-1}$ would arise. To ensure the steady state preservation, the spatial differences between nodes i and j are expressed in terms of a non-linear combination $Q(i, j)$ of Riemann invariants and depth. There are two versions of the difference stencil: one is the original VTCS-2 scheme (Titov and Synolakis, 1995, 1998),

and the other is its modification presently used in Cliffs. To approximate a spatial derivative at point j, the original scheme uses a difference across two cells $Q(j-1, j+1)$, whereas the modification uses a sum of left and right one-cell differences $Q(j-1, j) + Q(j, j+1)$ (Tolkova, 2015). In the linear limit (with respect to both depth variations and the state variables), the two schemes are identical. The modification seems to yield better-rounded results in strongly non-linear cases.

Cliffs inundation algorithm is based on a staircase representation of topography, and treats a vertical interface between wet and dry cells (a shoreline) as a vertical wall. To enable wetting/drying, a common procedure of comparing the flow depth with an empirical threshold h_{min} is used. The wet area expands when a flooding depth in a shoreline wet node exceeds a threshold (runup), and shrinks when a flow depth in a cell is below the threshold (rundown). On the wet area expansion, dry cells to be flooded are pre-filled with water to h_{min} depth. Hence the runup occurs on an inserted cushion h_{min} high, which is removed on rundown. Reflective boundary conditions applied on an instant shoreline are formulated using a mirror ghost node coinciding with a shoreline dry node.

4   Benchmark Problem Comparisons

4.1 Benchmark Problem #1: Steady Flow over Submerged Obstacle

The simulation was performed with 0.02 s (no friction case) or 0.03 s (frictional cases) time increment on a 394 x 61 node grid spanning an area 9.85 x 1.5 m with 2.5 cm interval. These time-space resolutions correspond to Courant number 0.6-0.9 over the flat part of the basin. The cone is on the centerline of the basin, with its top 5 m away from the left boundary. The constant flow (u=0.115 m/s) state was used to define incoming characteristics on the left and right boundaries, and to initialize the domain. The simulations were carried for three values of Manning roughness coefficient n, uniform over the domain: 0 (no friction case), 0.01, and 0.015. At the beginning of the simulations, the flow is symmetric about the centerline. The Karman vortex street eventually develops at any friction. The higher the friction, the longer it takes for the Karman vortex street to develop, and the more regular pattern emerges. Specifically, the first vortices appear about after 30 s from the start of the simulations in the no-friction case, after 60 s with *n=0.01*, and after 250 s with *n=0.015*.The modified VTCS-2 difference stencil yields more regular vortex patterns at low friction than the original stencil does. The results by the two numerical schemes are identical at higher friction.

Figure 10. Experimental data (dots) and numerical simulation (solid line, not shown) for a) U velocity component at time series location 1, b) V velocity component at time series location 1, c) U velocity component at time series location 2, and d) V velocity component at time series location 2.

4.2 Benchmark Problem #2: Tsunami Currents in Hilo Harbor

The simulations of the 2011-Tohoku tsunami in Hilo harbor were performed under prescribed settings, with time increment (0.5 s for 10 m spacing) providing for 0.86 Courant number in the most offshore part of the basin. The simulations were forced with a plane wave through the north boundary. The boundary time history was computed by solving a de-convolution problem given a prescribed synthetic time history at the virtual control point, and a computed response of the control point to a pulse sent in through the north boundary, using the response formalism introduced in (Power and Tolkova, 2013). The match between the computed and recorded tsunami time histories at Hilo tide gage is probably satisfactory, subject to how well the input time history represents the actual wave. Maximal current distribution computed with three different cell sizes (5, 10, and 20 m) consistently displays the same flow pattern, with the maximal speed being 6.7 m/s at 20 m resolution, 8.1 m/s at 10 m, and 8.3 m/s at 5 m resolution. Relatively low sampling rate (6 min) of the velocity measurements does not permit to decide whether the flow spectral content is reproduced correctly. Prior to the comparisons between the measured and computed (at 10 m spacing) maximal currents at ADCPs, the simulated time histories were re-sampled to the

moments of the measurements. At the ADCP 1125 at the harbor entrance, next to the area of the strongest currents and eddy formation, modeled maximal current over-estimated the measured maximum by a factor 1.3. At ADCP 1126 inside the harbor, the modeled and measured maximal currents are nearly perfect match, with their ratio being 0.99.

Figure 11. Measured data (dashed line) and numerical simulation (solid line) at the harbor tide gage (top), HA25 ADCP (middle), and HA26 ADCP (bottom).

Figure 12. Maximum predicted fluid speed (m/s) during entire duration of the 10-m resolution simulation.

4.3 Benchmark Problem #3: Tsunami Currents in Tauranga Harbor

The simulations of the 2011-Tohoku tsunami in Tauranga harbor, New Zealand were performed on 837 x 747 node grid with 30 m spacing, $t=1.2$ s, $n=0.025$. As in BP 2, the simulations were forced with a plane wave through the north boundary. Three input cases were simulated: tsunami only, tide only, and tsunami and tide combined. For each input case, the boundary time history was computed by solving a de-convolution problem given an actual sea surface record at a control point, and a computed response of the control point to a pulse sent in through the north boundary. In all three cases, the simulations and the measurements were a very good fit at all gages, as shown in Figure 4 at Tag Berth gage. The simulated current at the prescribed ADCP position was lower than the measurements (Figure 5). However, the current rapidly varied across narrow harbor entrance where the ADCP was positioned, being fast on the channel centerline, and low next to the banks. The flow transition from low by the shore to high in the channel occupied a slightly wider zone on the numerical grid. Indeed, simulated current 127 m (3 nodes diagonally) from the prescribed position toward the channel centerline provided nearly perfect fit to the observations (Figure 5, red).

Figure 4. Surface elevation time histories at Tug Berth tide gage: measured (dashed, blue), and simulated (red).

Figure 5. Current at ADCP: measured (blue dots), simulated at a prescribed ADCP position (green), and at 127 m (3 nodes diagonally) toward the channel centerline from the prescribed position (red)

*4.4 Benchmark Problem 4: Flow through a City Building Layout*

In this BP, a single wave inundates a 1:50 scaled lab model of Seaside, OR. Simulations were carried on a grid with varying cross-shore spacing (from 1 m at the deep end to 0.05 m near and in the town), to emulate dispersive behavior implied by the linear wave theory. However, given the wave height comparable with and exceeding the depth closer to the shore, emulating physical dispersion was possible only in the deeper part of the basin, until about a $x= 20$m mark. Manning roughness coefficient was $n=0.02$. For the comparisons with the observations, the added height of the runup cushion ($h_{min} = 2cm$) was subtracted from the simulated flow depth.

As seen in Figure 6 left pane, the wave transforms during shoaling, and develops undulations. Simulations closely reproduced the observed time-history at an offshore gage WG-3 (right pane in Figure 6). However, the simulated flow depth at the first onshore gage B1 is lower than that of its lab counterpart, whereas the simulated flow speed matches the observations. Tuning up friction over the land helps to improve match at farther inland gages, but the mismatch of the wave heights at B1 is persistent. Simulated wave experiences intense loss of energy through developing undulations in the last few meters before the shoreline - perhaps more than the actual wave did. Analysis of the wave time histories seaward from B1 (not shown) suggests that the mismatch between the simulations and the measurements at on-land gages Bs originated with the excessive

energy loss in the last few meters before the coastline rather than during overland propagation. There are not enough measurements near the coastline to find out where/how the dynamics of the simulated wave diverged from that observed.
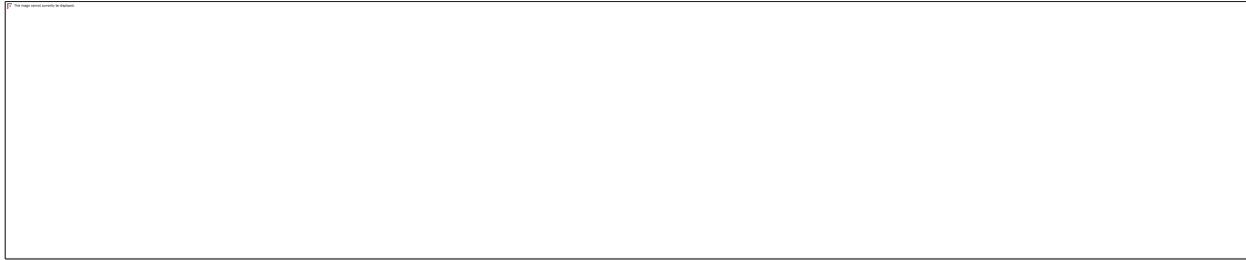
Figure 6. Left: cross-shore sea surface profiles at 18, 20, 22, 24, and 26 s along $y=-0.588$ (through B1); thick gray - topography. Black vertical lines mark positions of WG-3 and B1. Right: observations (blue) and simulated time history (red) at WG-3.
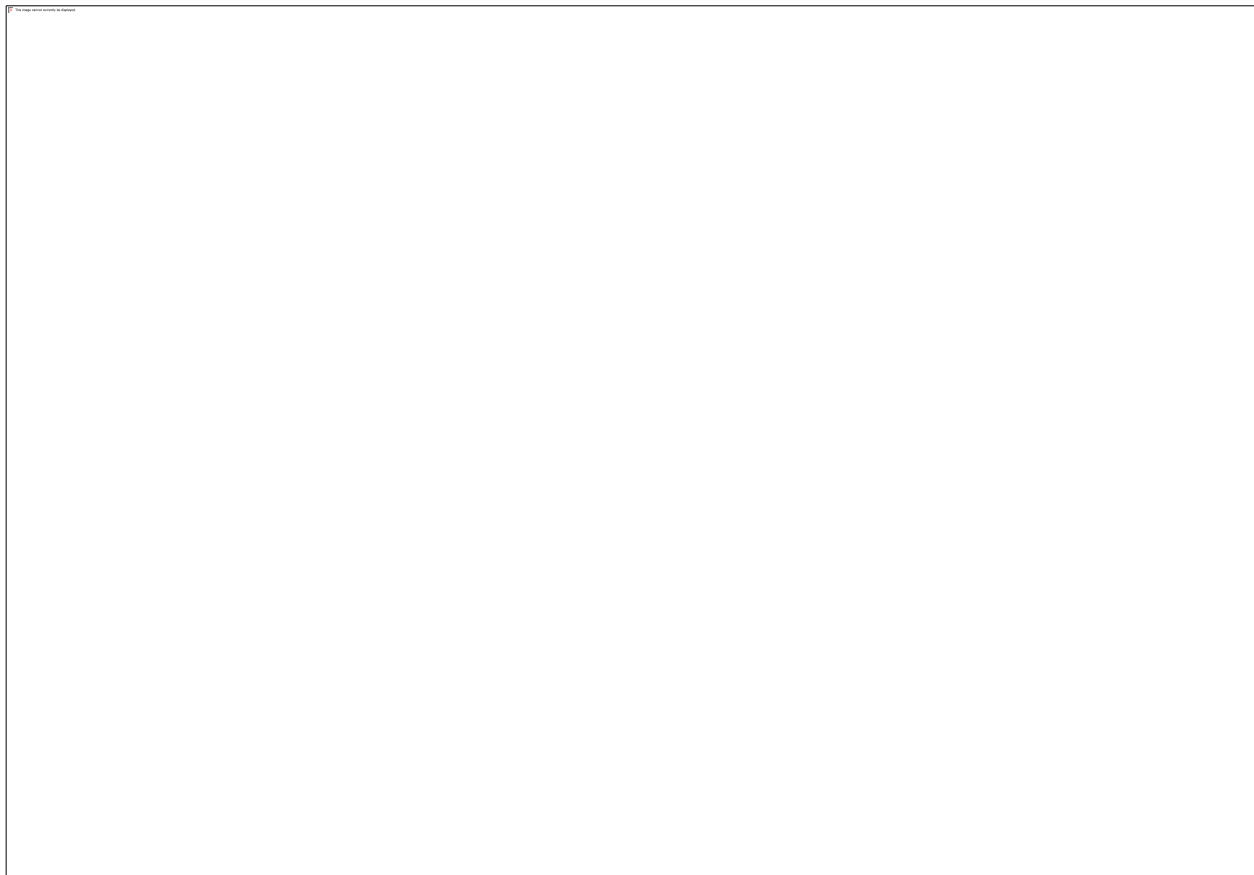
Figure 7. Rows, top to bottom: flow depth, cross-shore velocity, and cross-shore specific momentum flux at gages B1, B4, B6, and B9. Blue dots - observations; red - simulated time-histories at the gages Bs.

4.5 Benchmark Problem #5: Solitary Wave Propagation over a Complex Shelf

Computation were performed under setting attempting to imitate physical dispersion in the deeper (flat) part of the basin, with the grid resolution varying from 0.78 to 0.11 m, a time increment being 0.025 s, a roughness coefficient *n=0.011*. Simulations were forced with an analytical solitary wave input through the left boundary at x=7.5 m. As seen in Figure 8, the computed waveform of the direct pulse, both on the basin centerline (*y=0*) and off-center (*y=5*), follows that recorded in the experiment very closely up to a 13 m mark (on the tip of the triangular shelf). The model under-estimated the propagation speed of the wave over the shallow shelf, as well as somewhat misrepresented the waveform and under-estimated the height of the reflected wave, especially on the centerline. The latter might be an effect of wave shading by the island under the settings beyond the applicability of the shallow-water approximation. Modeled to measured cross-shore velocity comparisons on the basin centerline (two top left panels in Figure 9) display good agreement up to a 15 s mark, including backwash in front of the island, and until the arrival of the wave reflected by the beach. Along-shore velocity component on the centerline (two top right panels in Figure 6) is chaotic and no match can be reasonably expected. Both modeled flow components at the off-center location (two bottom panels in Figure 9) are good fit to the observations for the duration of both direct and reflected waves.

Figure 8. Modeled (red) and measured (blue) surface elevation time histories at the locations shown in the plots. Basin centerline at y=0.

Figure 9. Modeled (red) and measured (blue) velocity components at three ADVs: cross-shore U (left), and along-shore V (right). Corresponding locations are shown in left panels.

5   Conclusions

Cliffs numerical model was exercised with five Benchmark Problems offered by NTHMP Workshop on Tsunami Currents, Portland, Feb.9-10, 2015: two field cases, and three lab experiments. Cliffs performed in robust and accurate manner in all cases, but BP 4. Incidentally, in the last case, it performed well with regard to current even when it failed to correctly reproduce the flow depth. Cliffs performed best with simulating the 2011-Tohoku event in Tauranga harbor, New Zealand. This field BP stands out in that not only the model output is being compared to the observations, but the model input is also dictated by the real-world measurements. Under these settings leaving no uncertainty in both input and output, Cliffs reproduced the wave dynamics very accurately.

Cliffs was least successful with simulating an inundation of the scaled lab model of the town of Seaside, OR, where it significantly under-estimated flow depth over land. The latter might be a consequence of the model's excessive numerical dispersion and dissipation at the wave scales involved. Preliminary analysis points to loss of energy in the Cliffs solution in the last few meters before the shoreline, where the wave disintegrated into undulations caused by strong numerical dispersion of the VTCS-2 scheme. This behavior might not be an issue for the real-world problems, due to the following scale estimates. The duration of the attacking wave at WG-3 was about 8 s. The numerical wave developed undulations (possibly, artifacts) about 1 s in duration. With the lab

model being at 1:50 scale, these time intervals correspond to 1 min and 7 s, accordingly. These are too short for the real-world problems for which the model is intended. In particular, to generate 1 min long pulse in 1000 m deep water (estimated depth at Cascadia trench offshore Seaside), the width of the tsunami source function should be about 6 km - at least an order of value below an actual dimension of a real-world mega-earthquake.

Two filed BPs highlighted an important difference between interpreting modeling results with respect to wave height and with respect to current, arising from the fact that current varies in space more rapidly than the wave height. Hence, typically, a mismatch between simulated and observed wave heights at a given point indicates that a model misrepresented the wave height domain/subdomain-wide. The later might not hold true with regard to current. A mismatch between simulated and observed currents at a given point might indicate that the model slightly misrepresented the current spatial distribution, for example, by stretching a transition zone between high and low currents. Then current at a nearby point might provide a better representation for the real-world prototype. This option was investigated with BP 3, but not with BP 2.

References

1. D. Burwell, E. Tolkova, and A. Chawla, "Diffusion and Dispersion Characterization of a Numerical Tsunami Model", Ocean Modelling, **19**(1-2), 10-30 (2007), doi:10.1016/j.ocemod.2007.05.003.

2. [NTHMP] National Tsunami Hazard Mitigation Program. Proceedings and Results of the 2011 NTHMP Model Benchmarking Workshop. Boulder: U.S. Department of Commerce/NOAA/NTHMP; NOAA Special Report. 436 p., July 2012

3. W. Power and E. Tolkova, "Forecasting tsunamis in Poverty Bay, New Zealand, with deep-ocean gauges", Ocean Dynamics, **63**(11), 1213-1232 (2013). doi: 10.1007/s10236-013-0665-6.

4. G. Strang, "On the construction and comparison of difference schemes", SIAM Journal on Numerical Analysis, **5**(3), 506-517 (1968).

5. V. V. Titov and C. E. Synolakis, "Modeling of breaking and nonbreaking long-wave evolution and runup using VTCS-2", J. Waterw., Port, Coastal, Ocean Eng., **121**(6), 308316 (1995).

6. V.V. Titov and F.I. Gonzalez, Implementation and testing of the Method of Splitting Tsunami (MOST) model. NOAA Tech. Memo. ERL PMEL-112 (PB98-122773), NOAA/Pacific Marine Environmental Laboratory, Seattle, WA, 11 pp. (1997).

7. V. V. Titov and C. E. Synolakis, "Numerical modeling of tidal wave runup", J. Waterw., Port, Coastal, Ocean Eng., **124**(4), 157171 (1998).

8. E. Tolkova, "Curvilinear MOST and its first application: Regional Forecast version 2". In: D. Burwell and E. Tolkova. Curvilinear version of the MOST model with application to the coast-wide tsunami forecast, Part II. NOAA Tech. Memo. OAR PMEL-142, 28 pp. (2008)

9. E. Tolkova, "MOST (Method of Splitting Tsunamis) Numerical Model". In: [NTHMP] National Tsunami Hazard Mitigation Program. Proceedings and Results of the 2011 NTHMP Model Benchmarking Workshop. Boulder: U.S. Department of Commerce/NOAA/NTHMP; NOAA Special Report. 436 p. (2012)

10. E. Tolkova, "Land - Water Boundary Treatment for a Tsunami Model With Dimensional Splitting". Pure and Applied Geophysics, **171**(9), 2289-2314 (2014). doi: 10.1007/s00024-014-0825-8.

11. E. Tolkova (2015). Cliffs User Manual. http://arxiv.org/abs/1410.0753

GeoClaw Benchmark Results

Randall J. LeVeque,[a] Frank I. González[b], and Loyce M. Adams[a]
[a]University of Washington, Dept. of Applied Mathematics, Seattle, WA 98195
[b]University of Washington, Dept. of Earth & Space Sciences, Seattle, WA 98195

Abstract. The open source GeoClaw software has been applied to four of the problems from the NTHMP Tsunami Currents Benchmarking Workshop of 2015. Two problems compare simulation results to laboratory experiments of unstable vortices generated by a submerged obstacle and of flow through a scale model of an urban environment. The other two problems compare simulations against observations recorded during the 2011 Tohoku event, in Hilo Harbor, Hawaii, and in Tauranga Harbour, New Zealand.

Address all correspondence to: Randall J. LeVeque, University of Washington Department of Applied Mathematics, Seattle, WA 98195-3925; Tel: +1 206-685-3037; Fax: +1 206-685-1440; E-mail: rjl@uw.edu

1   Model Background

The open source GeoClaw software has been actively developed at the University of Washington and by collaborators elsewhere for over 10 years, starting with the work of George (2006, 2008) and George & LeVeque (2006), and is part of the Clawpack software suite (Clawpack Development Team, 2015). The model was validated using the NTHMP benchmarks, as reported in Gonzalez et al. (2011). Validation against synthetic problems was performed in Berger et al. (2011) and LeVeque et al. (2011) and against data from the Tohoku event in Arcos & LeVeque (2015) and MacInnes et al. (2013). Following NTHMP approval, it has been used for several hazard assessment projects for the State of Washington Emergency Management Division (Gonzalez et al. (2013b, 2013c) and on-going development of new inundation maps), and as the basis for development of PTHA methodology for a pilot project funded by FEMA and Baker/AECOM (Gonzalez et al. (2013a) and Adams, et al. (2015)). This software has also been used by several other groups for modeling past events and performing hazard assessment. More references can be found at www.geoclaw.org.

2   Model Equations

GeoClaw approximately solves the two-dimensional nonlinear shallow water equations (SWE). The variables are depth and momenta in the two horizontal directions. The nonlinear equations are written in conservation form, with the addition of source terms in the momentum equations for the effect of variable topography and bottom friction, which is modeled by a Manning friction term. Wave breaking is handled via shock formation in the SWE. Coriolis terms can be included in GeoClaw but are generally turned off since they have been found to have little effect on tsunami propagation (Berger et al. 2011).

3   Numerical Solution Method

GeoClaw solves the nonlinear SWE using a high-resolution shock-capturing finite volume method based on solving Riemann problems at cell interfaces and applying second-order correction terms with limiters to avoid non-physical oscillations near discontinuities, while obtaining sharp

resolution of shocks and achieving second-order accuracy in regions where the solution is smooth. These general methods are described in detail in LeVeque (2002). The equations are solved on logically-rectangular grids in longitude-latitude on the curved surface of the sphere. Block-structured adaptive mesh refinement (AMR) is used to concentrate computational work in the regions around the propagating wave in the ocean, and to obtain much higher resolution at points of interest along the coast. The topography source terms are incorporated into the Riemann solution in a well-balanced manner that exactly preserves the ocean-at-rest steady state solution and insures that limiters are applied only to the propagating waves modeling deviation from steady state. The coastline is modeled as the interface between wet cells and dry cells, and the Riemann solvers developed by George (2006, 2008) robustly handle wetting and drying during inundation. By using fine AMR grids in regions of interest, the fact that cells are rectangular is not an issue. The numerical methods and AMR algorithms used in GeoClaw are presented in detail in Berger et al. (2011), along with a review of tsunami applications. GeoClaw uses OpenMP to achieve reasonable parallel performance on multi-core shared memory computers. For each benchmark problem we report approximate run times using this capability on a quadcore MacBook Pro laptop computer.

4   Benchmark Problem Comparisons

4.1 Benchmark Problem #1: Steady Flow over Submerged Obstacle

For the GeoClaw simulation, we set the Manning coefficient to zero where the tank bottom is flat, and to nonzero values on the conical hill. We found that with friction applied everywhere, the flow slows down or the depth increases with time, depending on the boundary conditions imposed on the left boundary. Note that flow is sub-critical (the Froude number is less than 1 near the left boundary) and information propagates upstream so that, mathematically, it is not correct to specify both an inflow depth and an inflow velocity as is suggested in the problem description. The flow will slow down due to friction as it flows down the channel, which should cause the depth to increase and this increase will propagate back to the inflow. When friction is set to zero except on the cone, there is minimal effect, but with friction everywhere we found a significant effect. Several other modeling groups did not encounter this problem and applied friction everywhere, and this requires further study in GeoClaw. We used a 260x20 coarse grid over the domain $0 \le x \le 19.76$ and $0 \le y \le 1.52$, and allowed a second level of refinement by a factor of 8 over the region $3 \le x \le 10$. The obstacle was centered at x = 5. These runs typically required about 20 minutes of wall time to compute for 200 seconds of simulated time (on a quadcore MacBook Pro).

We did not highly optimize the results, but obtained reasonable agreement with observations by using Manning coefficient n = 0.015, in terms of the period of the vortex shedding. The peak velocity amplitudes were greater in the GeoClaw simulations than the observed peaks, perhaps because we had no bottom friction downstream from the obstacle. We also found that the results with unstable vortex shedding are very sensitive to any changes in parameters, or even to the time step used. For example, changing the target Courant number in our adaptive code from 0.9 to 0.89 (resulting in slightly smaller time steps) gives very different vortex shedding patterns, although the period and peak velocities were similar at each gauge. For n = 0.025 we observed a steady vortex street.

Figure 13. Experimental data (dots) and numerical simulation (solid line, not shown) for a) U velocity component at time series location 1, b) V velocity component at time series location 1, c) U velocity component at time series location 2, and d) V velocity component at time series location 2.

4.2 Benchmark Problem #2: Tsunami Currents in Hilo Harbor

Adaptive mesh refinement was used with the resolution near the top boundary fixed at 2 arc-seconds (180 m) to simplify specifying uniform boundary forcing, but the bulk of the domain was refined to the resolutions specified in the problem. The computational domain was longitude $204.905 \leq x \leq 204.965$, and latitude $19.71 \leq y \leq 19.758$. The control point where the incident wave information was specified is (204.93, 19.7576). The boundary conditions were set at y=19.758 based on this data. Each time step, the depth h and momentum hu in the grid cell containing this point is used to determine an incoming plane wave moving in the y-direction necessary to match the data at this point. At other points along the boundary, the ghost cell data is chosen so that the incoming wave matches this. The control point data provided starts at a surface elevation of −0.13 m rather than at 0. As in the provided Matlab script, we also shifted the provided elevation by 0.13 for use as the input in a simulation where the sea level was set to 0 relative to the bathymetry provided (corresponding to MHW).

The grid refinement study showed reasonable self-consistent overall convergence of our results, going from 20-meter to 10-meter to 5-meter resolution. However, we observed that the strong vortex shedding at the end of the sea wall creates vortices that can be quite different at different resolutions. This potentially limits the ability to compare results directly (both at different resolutions for a single model, or to compare different models), since the velocities observed at a gauge can be very different if a vortex happens to pass near the gauge or does not. Full simulation of the Tohoku tsunami from the source region, propagating across the Pacific, and then into Hilo Harbor using GeoClaw has been studied in Arcos and LeVeque (2015), using the earthquake source model of Fujii et al. (2011). For this benchmark study we also solved the full problem using the source of Shao et al. (2011). In both cases our results showed very different surface elevation at the specified control point than what was provided for this benchmark problem, as well as differences at the ADCP gauges. For these reasons, we question the value of comparing different models to the observed data for this problem. Regardless of agreement with the observations, this is a valuable problem for comparing the predictions of different models in a realistic harbor with highly constrained input data. The simulations over only the harbor with 1/3 arc-second (10 meter) resolution for 5 hours of simulated time required about 45 minutes to complete. The full simulations from the source over 13 hours of simulated time, with comparable resolution in the harbor during the last 5 hours after the tsunami arrives, required about 75 minutes.
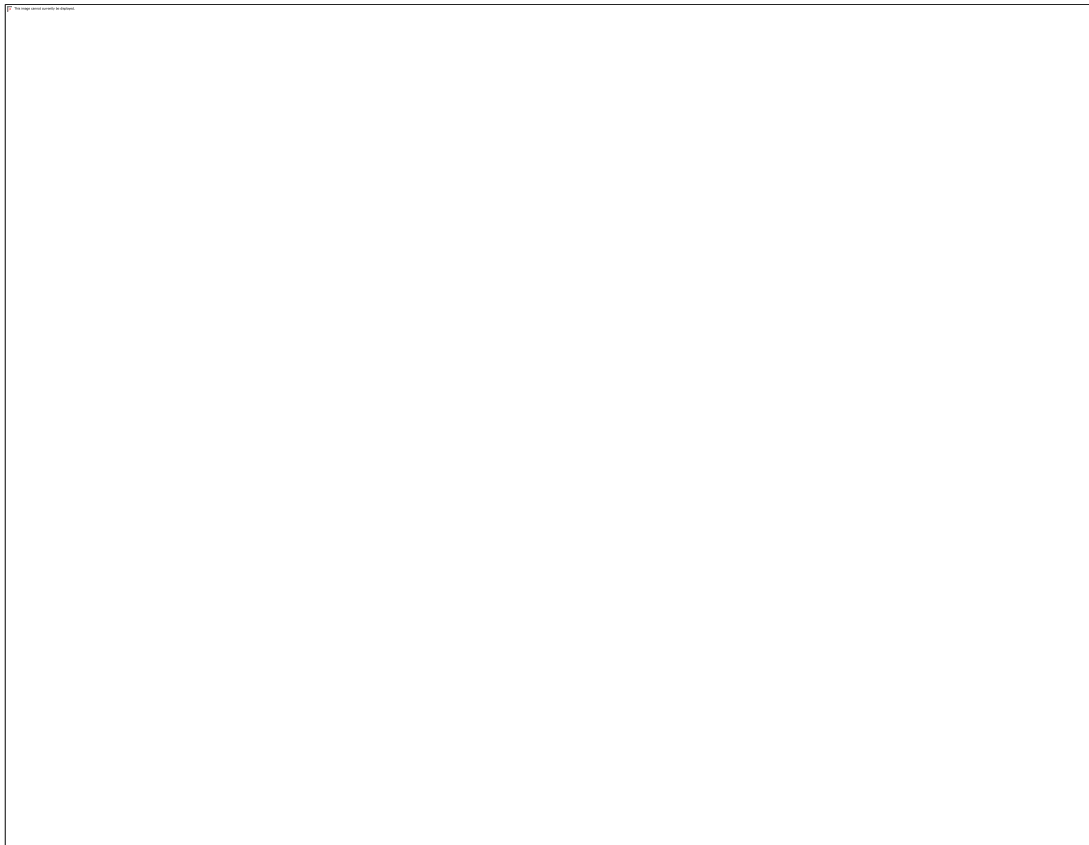
Figure 14. Measured data (dashed line) and numerical simulation (solid line) at the harbor tide gage (top), HA25 ADCP (middle), and HA26 ADCP (bottom).

Figure 15. Maximum predicted fluid speed during entire duration of the 10-m resolution simulation.

4.3 Benchmark Problem #3: Tsunami Currents in Tauranga Harbor

For this optional problem, we did not set up the boundary conditions specified in the benchmark problem. Instead we found it more illuminating to solve the full problem from earthquake initiation, for which we used the source of Fujii et al. (2011). Adaptive mesh refinement was used with 7 levels of refinement. The coarsest grid covered the full computational domain from longitude 120E (-240) to 100W (-100) and latitude 60S to 60N with a 35x30 grid (4 degree cell size). Refinement ratios from each level to the next were 10, 6, 4, 10, 6, 3, so that the finest level had a cell size of 1/3 arc-second (10 meter). Three levels of refinement were allowed for regions of trans-oceanic propagation, clustered around the first incident wave approaching New Zealand, Up to 5 levels of refinement were allowed over all of Tauranga Harbour, with levels 6 and 7 only allowed near the harbour entrance, as shown in Figure 4 at time 15.5 hours post-earthquake. The computation to this point required approximately 3.5 hours.

Figure 5 shows sample results for the surface elevation at the locations A-Beacon and TUG, and the velocities compared to observations at the ADCP location. The times have been shifted by 12 minutes to better match the observations. This time shift is at least partly due to the non-dispersive nature of the shallow water equations, as discussed in Arcos & LeVeque (2015). These results are

promising but very preliminary. We did not explore the effect of changing the earthquake source model or refinement criteria.
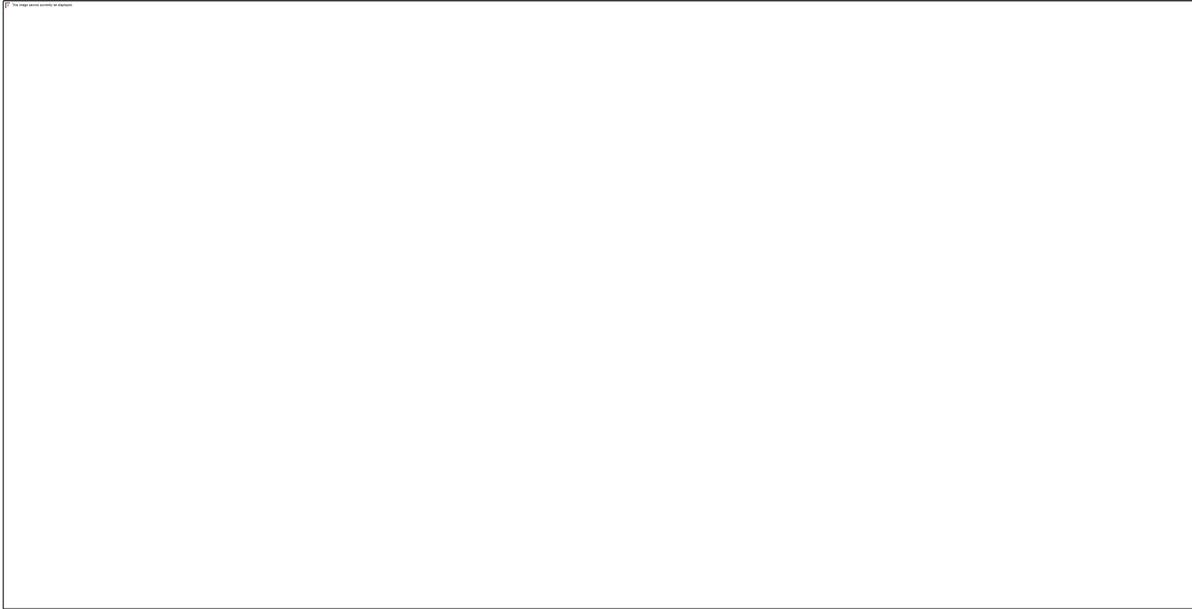
Figure 4. Benchmark Problem #3. Zoom on the north Island of New Zealand (left) and the Tauranga Harbour region (right) showing the AMR grid resolutions in these regions at 15.5 hours post-earthquake.

Figure 5. Benchmark Problem #3. Comparison of observations (black circles) with GeoClaw simulation (red curves) at two locations for surface elevation and at the ADCP gauge location.

4.4 Benchmark Problem #4: Flow through a City Building Layout

The bathymetry file provided was used as topography in GeoClaw without any significant problems, in spite of the fact that the lidar data is quite rough and so the buildings are not represented as smooth shapes. Manning coefficient 0.025 was used. The data provided for the wavemaker speed s(t) can be fit quite well with a Gaussian of the form $s(t)=A \exp(\beta(t-t_0)^2)$ with $\beta=0.25$, $t_0=14.75$ and amplitude $A=0.51$. However, the amplitude at the Wave Gauge at x=5 matched better in our computation by setting A=0.6, probably due to the fact that our boundary

conditions are prescribed as a stationary wall with a prescribed velocity boundary condition, which implicitly assumes small amplitude at the boundary. Adaptive mesh refinement was used. The coarsest grid had a resolution of approximately 0.5 meter cells (54×88 grid cells on the full domain). The finest grid, which only covered the Seaside model region, was refined by a total factor of 40 relative to the coarsest grid (1.25 cm cell size). The total run time with these parameters was about 30 minutes (out to t = 40 seconds of simulated time).

GeoClaw handled flow through this complex topography quite robustly. Figure 6 shows a zoomed view of the simulation at time t=30 over part of the domain to exhibit the inundation pattern, overtopping of some buildings, and the generation of many shock waves within the flow. Figure 7 shows the depth, speed, and momentum flux as functions of time at the specified gauges labeled B1, B4, B6, and B9 in the problem description (numbered 201, 204, 206, and 206 in Figure 6). We did not observe as much inundation at gauge B9 as was seen in the experiment, perhaps because of the choice of Manning coefficient.

Figure 6. Simulated flow depth for Benchmark #4 at t = 30 seconds. Scale is in meters. The points labeled 201 through 209 correspond to gauges B1 through B9 where results are compared with observations. The points labeled 101-109 correspond to the A gauges and 301-309 to the C gauges. The D gauges are not seen in this zoomed view.

100

Figure 7. Benchmark Problem #4. Observed depth, speed, and momentum flux at the four gauges B1, B4, B6, and B9 are shown in blue, along with the GeoClaw simulations in red.

5   Conclusions

Maximum flow speeds can vary significantly over very short spatial scales, as observed for example in the plots of maximum velocity in Hilo Harbor in Figure 2. The current around the tip of the seawall is much stronger than other locations nearby and the vortices that are generated can lead to high velocities in concentrated regions that are highly sensitive to the details of the numerical modeling. As mentioned in Section 4.1, the details of the unsteady vortices generated are very sensitive even to small changes in the time step on a fixed grid. This leads to significant challenges in validating numerical tsunami models for studies involving currents. Nonetheless, the results obtained on these benchmark problems are encouraging and indicate that some useful information about tsunami currents and maximum speeds can be obtained from GeoClaw simulations. These tests did not uncover any obvious deficiencies in the code, beyond the limitations inherent in using the two-dimensional SWE to model complex flows that may be fully three-dimensional. The incorporation of dispersive terms into GeoClaw is work in progress that may lead to better modeling of some phenomena, although it is not clear to what extent this is important for these benchmark problems.

Additional plots of GeoClaw results, some animations, and additional comments on the benchmark problems can be found at
  http://www.geoclaw.org/ benchmarks/nthmp_currents_2015
The GeoClaw code used to perform these experiments can be found in the GitHub repository
  https://github.com/rjleveque/tsunami_benchmarks

6   Acknowledgments

References

1. Adams, L. M., LeVeque, R. J. & González, F. I. The Pattern Method for incorporating tidal uncertainty into probabilistic tsunami hazard assessment (PTHA). *Nat Hazards* **76,** 19–39 (2014).

2. Arcos, M. E. M. & LeVeque, R. J. Velocity Measurements Near Hawaii Compared to Model Simulations of the 11 March 2011 Tohoku Tsunami. *Pure Appl. Geophys.* **172,** 849–867 (submitted).

3. Berger, M. J., D. L. George, R. J. LeVeque, and K. T. Mandli, The GeoClaw software for depth-averaged flows with adaptive refinement, Adv. Water Res. 34, 1195-1206 (2011).

4. Fujii, Y., Satake, K., Sakai, S., Shinohara, M. & Kanazawa, T. Tsunami source of the 2011 off the Pacific coast of Tohoku Earthquake. *Earth, planets and space* **63,** 815–820 (2011).

5. GeoClaw Development Team, The GeoClaw software (2015). <http://www.geoclaw.org>

6. George, D. L. Finite Volume Methods and Adaptive Refinement for Tsunami Propagation and Inundation. (University of Washington, 2006).

7. George, D. L. Augmented Riemann solvers for the shallow water equations over variable topography with steady states and inundation. *J. Comput. Phys.* **227,** 3089–3113 (2008).

8. George, D. L. & LeVeque, R. J. Finite volume methods and adaptive refinement for global tsunami propagation and local inundation. *Science of Tsunami Hazards* **24,** 319–328 (2006).

9. Gonzalez, F. I., LeVeque, R. J. & Adams, L. M. *Probabilistic Tsunami Hazard Assessment (PTHA) for Crescent City, CA. Final Report for Phase I*. (2013a). at <http://hdl.handle.net/1773/22366>

10. Gonzalez, F., LeVeque, R. & Adams, L. Tsunami Hazard Assessment of the Elementary School Berm Site in Long Beach, WA. *Final Report Submitted to WA EMD* (2013b). at <https://digital.lib.washington.edu/researchworks/handle/1773/22705>

11. Gonzalez, F., LeVeque, R. & Adams, L. Tsunami Hazard Assessment of the Ocosta School Site in Westport, WA. *Final Report: September 11, 2013* (2013c). at <https://digital.lib.washington.edu/researchworks/handle/1773/24054>

12. Gonzalez, F., R. J. LeVeque , P. Chamberlain, B. Hirai, J. Varkovitzky, and D. L. George, GeoClaw Results for the NTHMP Tsunami Benchmark Problems (2011) [http://depts.washington.edu/clawpack/links/nthmp- benchmarks/geoclaw-results.pdf].

13. LeVeque, R. J. *Finite Volume Methods for Hyperbolic Problems*. (Cambridge University Press, 2002).

14. LeVeque, R. J., George, D. L. & Berger, M. J. Tsunami modeling with adaptively refined finite volume methods. *Acta Numerica* 211–289 (2011).

15. MacInnes, B. T., Gusman, A. R., LeVeque, R. J. & Tanioka, Y. Comparison of earthquake source models for the 2011 Tohoku event using tsunami simulations and near field observations. *Bull. Seis. Soc. Amer.* 1256–1274 (2013).

16. Shao, G., Li, X., Ji, C. & Maeda, T. Focal mechanism and slip history of the 2011 Mw 9.1 off the Pacific coast of Tohoku Earthquake, constrained with teleseismic body and surface waves. *Earth Planet Sp* **63,** 559–564 (2011).

GeoClaw-AECOM Benchmark Results

Hong Kie Thio,[a] Wenwen Li [a]

[a]AECOM, 915 Wilshire Blvd, Los Angeles, CA 90017

Abstract. This report presents the results from the NTHMP velocity benchmark exercises (nos. 1,2,4 and 5) for the AECOM GeoClaw-based tsunami code. In general we find good agreements with the observed data in most cases but notice a much stronger sensitivity of the velocities (compared to amplitudes) on parameters such as Manning's coefficient.

Address all correspondence to: Hong Kio Thio, AECOM, 915 Wilshire Blvd, Los Angeles, CA 90017; Tel: +1 213-996-2250; Fax: +1 213-996-2290; E-mail: hong.kie.thio@aecom.com

1   Model Background

AECOM has developed an in-house version of the GeoClaw code to facilitate the use in the current AECOM work environment, which requires the computation of large numbers of scenarios with multiple high-resolution target areas. The most important change is the use of nested grids rather than adaptive meshing. This code is currently being used in the development of probabilistic tsunami inundation maps for the State of California. We have also complemented the original set of NTHMP validation exercises, the report of which is pending.

2   Model Equations

The model solves the two-dimensional depth-averaged nonlinear shallow water equations:

$$h_t + (hu)_x + (hv)_y = 0,$$

$$(hu)_t + (hu^2 + \frac{1}{2}gh^2)_x + (huv)_y = -ghB_x - Du,$$

$$(hv)_t + (huv)_x + (hv^2 + \frac{1}{2}gh^2)_y = -ghB_y - Dv,$$

(1)

where u (x, y, t) and v (x, y, t) are the depth-averaged velocities in the two horizontal directions, B (x, y, t) is the topography or bathymetry, and D (h, u, v) is the drag coefficient. In case of the existence of friction, manning correlation is use for the friction:

$$D = \frac{gn^2\sqrt{u^2 + v^2}}{h^{5/3}}$$

(2)

where n is the Manning's coefficient, generally taken to be 0.025.

3   Numerical Solution Method

The model is based on the core of the GeoClaw solver which solves the two-dimensional depth-averaged nonlinear shallow water equations using high-resolution finite volume methods. The methods are based on Godunov's method that consists of solving the Riemann problem and using the resulting wave structure to update cell averages in the adjacent finite volume cells. In practice an approximate Riemann solution is used. Refer to GeoClaw for details of the model numerical scheme (the numerical accuracy and sources of numerical dissipation; the model shoreline boundary scheme).

4   Benchmark Problem Comparisons

4.1 Benchmark Problem #1: Steady Flow over Submerged Obstacle

The computational domain is 0 m $\leq x \leq$ 20 m and 0 m $\leq y \leq$ 1.52 m. The grid cell size is 7.6 mm. The Courant/CFL number used is 0.70. The constant velocity $u = 0.115$ m/s is imposed at the left boundary. The Manning coefficient is set to zero where the tank bottom is flat and is only nonzero on the conical hill. If we apply a non-zero Mannings coefficient throughout the model, the flow would slow down too much due to friction. When friction is set to zero except on the cone, the slow-down is minimal.

The comparison plots with the Mannings Coefficient $n = 0.015$ applied only on cone are shown in Figure 16. Experimental data (dots) and numerical simulation (solid line, not shown) for a) U velocity component at time series location 1, b) V velocity component at time series location 1, c) U velocity component at time series location 2, and d) V velocity component at time series location 2.. We found the Mannings coefficient $n = 0.015$ is the optimum value other than the requested value 0.01. The results with unstable vortex street development are very sensitive to any changes in the model (such as the Courant number). The comparison plots with the Mannings Coefficient $n = 0.015$ applied only on cone are shown in Figure 16. Experimental data (dots) and numerical simulation (solid line, not shown) for a) U velocity component at time series location 1, b) V velocity component at time series location 1, c) U velocity component at time series location 2, and d) V velocity component at time series location 2.. We found the Mannings coefficient $n = 0.015$ is the optimum value other than the requested value 0.01. The results with unstable vortex street development are very sensitive to any changes in the model (such as the Courant number) – slightly changing the Courant number gives very different vortex shedding patterns
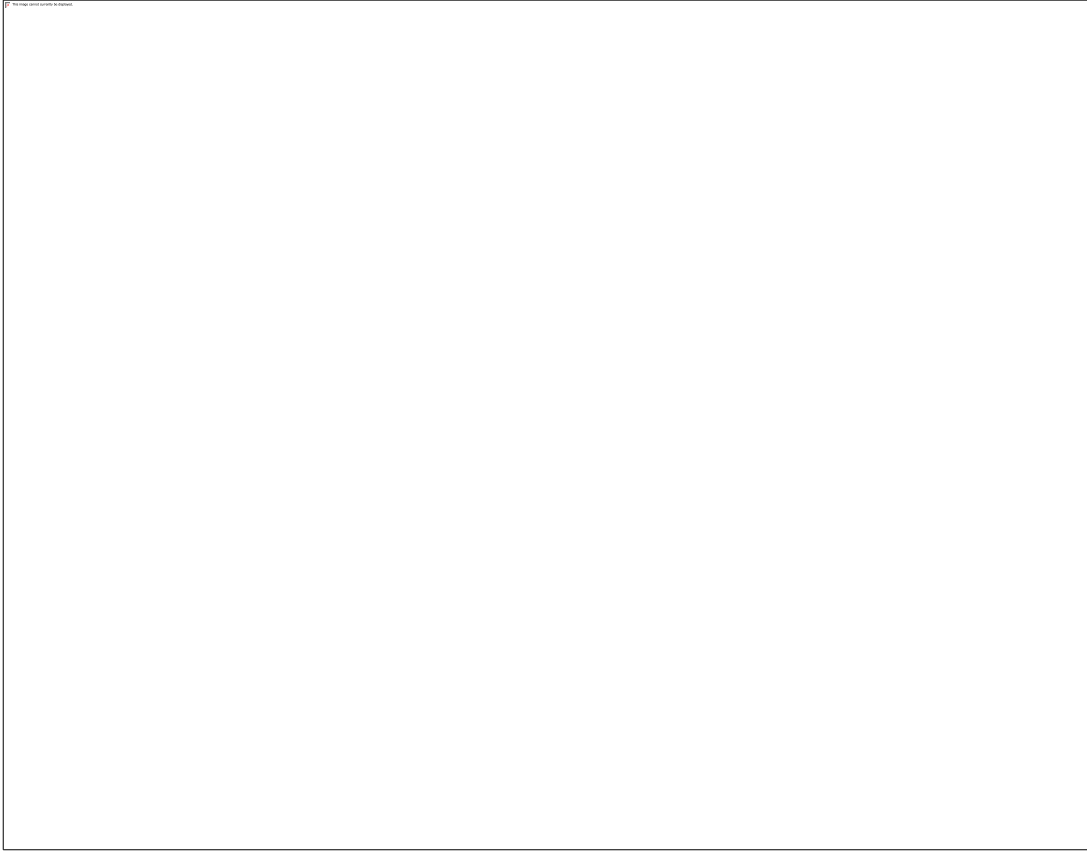
Figure 16. Experimental data (dots) and numerical simulation (solid line, not shown) for a) U velocity component at time series location 1, b) V velocity component at time series location 1, c) U velocity component at time series location 2, and d) V velocity component at time series location 2.

4.2 Benchmark Problem #2: Tsunami Currents in Hilo Harbor

The computational domain is longitude $204.901º \leq x \leq 204.965º$ and latitude $19.710º \leq y \leq 19.774º$. The Mannings coefficient is set to $n = 0.025$. The Courant number used is 0.75. The incident wave was specified at the control point (204.93, 19.7576). The boundary condition at $y = 19.774$ was based on this information. There are three different numerical configurations: ~ 20 m (2/3 arcsec) resolution, ~ 10 m (1/3 arcsec) resolution, and ~ 5 m (1/6 arcsec) resolution. Figure 2 presents comparisons of the simulated and measured water surface elevation at the Hilo tide station (204.9447, 19.7308), as well as the velocity measurement locations. Figure 3 provides the maximum flow speed recorded during the simulation.
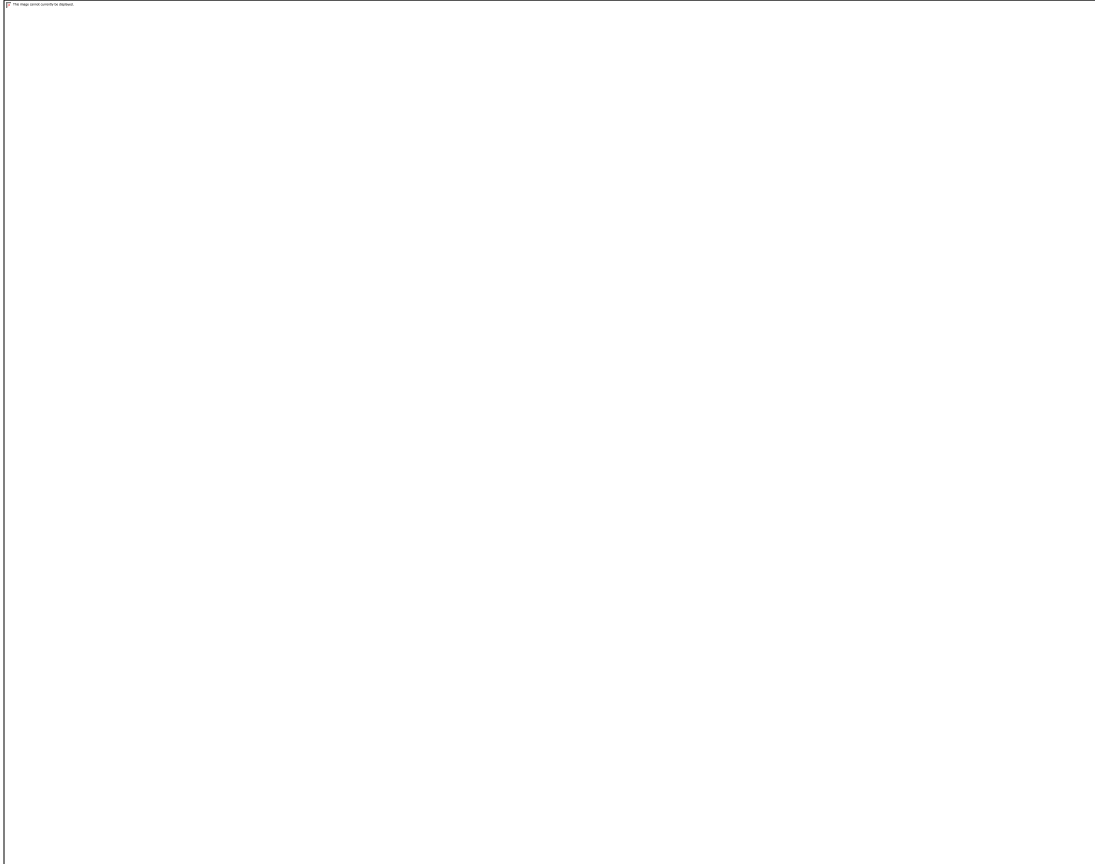
Figure 17. Measured data (dashed line) and numerical simulation (solid line) at the harbor tide gage (top), HA25 ADCP (middle), and HA26 ADCP (bottom).

Figure 18. Maximum predicted fluid speed during entire duration of the 10-m resolution simulation.

5   Conclusions

The overall reasonable agreement between measured data and numerical simulation demonstrates the validity of our numerical model (nonlinear and non-dispersive shallow water equations) with the above benchmark problems. The dispersive effects are important for some cases that cannot be captured by the non-dispersive shallow water equations.

The numerically computed runup values can be significantly affected by changes in the value of the Mannings coefficient of friction. Since the friction term is a function of water depth, the effects are more important for shallow water.

Tsunami-HySEA Benchmark Results

Jorge Macías[a], Manuel J. Castro[a], Sergio Ortega[b], Cipriano Escalante[a], José Manuel González-Vida[c].

[a]University of Málaga, Facultad de Ciencias, Departamento de Análisis Matemático, Campus de Teatinos, s/n, Málaga, Spain, 29080

[b]University of Málaga, Laboratorio de Métodos Numéricos, SCAI, Campus de Teatinos, s/n, Málaga, Spain,29080

[c]University of Málaga, E.T.S. Telecomunicación, Departamento de Matemática Aplicada, Campus de Teatinos, s/n, Málaga, Spain, 29080

Abstract. The Tsunami-HySEA model is used to perform the five numerical benchmarks proposed in the *"NTHMP/MMS Benchmarking Workshop: Tsunami currents"*. Many different model configurations and sensitivity studies were performed for the different benchmarks, combining numerical methods of first, second and third order, different friction laws, varying friction coefficients and numerical resolution or even different implementations of the boundary conditions for BP1. For benchmark #2, the complete scenario (Tohoku 2011) computed from the source was also presented. Benchmark 1 appeared to be the most difficult one due to its large sensitivity. For benchmarks 2 to 5 good fit with measured data is obtained. A first version of Tsunami-HySEA model implementing dispersion was used to reproduce benchmark problem 5.

Address all correspondence to: Jorge Macías, University of Malaga, Facultad de Ciencias, Departamento de Análisis Matemático, Campus de Teatinos, s/n, 29080-Málaga, Spain; Tel: +34 952132016; Fax: +34 952131894; E-mail: jmacias@uma.es

1   Model Background

HySEA (**Hy**perbolic **S**ystems and **E**fficient **A**lgorithms) software consists of a family of geophysical codes based on either single layer, two-layer stratified systems or multilayer shallow water models. HySEA codes have been developed by EDANYA Group (http://edanya.uma.es) from the Universidad de Málaga (UMA) for more than a decade and they are in continuous evolution and upgrading. Initially, the software was developed and the numerical algorithms implemented published under no particular name. Several developments have been published in peer-review international journals since 2005 where different analytical and experimental test cases have been presented. Ordered by year of publication, some of these model developments can be found in [1]-[7]. In September 2013, at ITS 2013, held at Göcek (Turkey) the ensemble of all the codes was named as HySEA for the very first time, and Landslide-HySEA (for aerial landslide) and Tsunami-HySEA presented in the two separate contributions [8] and [9], respectively. The work recently published in MARGO in [10], in this case for a submarine landslide, it is the first peer-review paper where HySEA code is named as such.

Tsunami-HySEA is the numerical model specifically designed for tsunami simulations. It combines robustness, reliability and good accuracy in a model based on a GPU faster than real time (FTRT) implementation. It has been severely tested, and in particular has passed all tests in *Synolakis et al. (2008),* but also other laboratory tests and proposed benchmark problems. Some of them can be found in references [1]-[7] cited above. *Synolakis et al. (2008)* test cases for HySEA can be found at [11] in Spanish, and will be gathered in a companion NTHMP report [12]. Among these benchmarks the Monai Valley test case, one of the most emblematic test cases for tsunami

codes, was presented at EGU 2013 in [13]. A comparison of Tsunami-HySEA numerical results with the MOST model for LANTEX 2013 scenario and tsunami impact on Puerto Rico coasts can be found at [14]. Besides all this, much effort has been made to develop a specific HySEA code suitable for tsunami computations in the framework of Tsunami Early Warning Systems (TEWS). The work done to develop a tsunami code for computations in times much faster than real time was presented at EGU 2014 in [15] and at Perspectives of GPU Computing in Physics and Astrophysics in [16]. The TEWS version of Tsunami-HySEA is currently the core numerical code at INGV (Instituto Nazionale di Geofisica e Vulcanologia) of the Italian TEWS. It is also going to be adopted by the JRC (Joint Research Centre of the European Commission) as one of the numerical codes of their Tsunami Alert System and by the Spanish IGN (Instituto Geográfico Nacional) in its future TEWS. In order to be approved by the INGV as the numerical code for their system, the Tsunami-HySEA model has passed through an exhaustive one-year validation process at INGV. In fact, sixteen different TVD and non-TVD numerical schemes were implemented and tested in search for robustness, computational speed-up and suitable numerical results, in order to make a final suitable choice for the code to be adopted by the Italian TEWS. A comparative study containing most of these numerical schemes can be found at [17]. An important application of the Tsunami-HySEA model to the emblematic real case of Tohoku 2011, can be found in [18]. In December 2014, Lisbon 1775 and Puerto Rico 1918 earthquake scenarios were simulated with Tsunami-HySEA and presented at the "Experts Meeting Workshop on Tsunami Modeling and Mitigation" held at Cartagena de Indias (Colombia). The presentation can be downloaded at [19]. Concerning landslide-generated tsunamis, a stratified two-layer Savage-Hutter shallow water model, the Landslide-HySEA model, was implemented based on [4] and incorporated to the HySEA family. Validation of this code comparing numerical results with the laboratory experiments of *Heller and Hager (2011)* and *Fritz et al. (2001)* can be found at [20]. A milestone in the validation process of this code consisted in the numerical simulation of the Lituya Bay 1958 mega-tsunami with real topo-bathymetric data in [21]. This validation was carried out under a research contract with PMEL/NOAA. The result of this project leads NCTR to adopt Landslide-HySEA as the numerical code used to generate initial conditions for the MOST model to be initialized in the case of landslide-generated tsunami scenarios. A related research consisted, a joint work with PMEL/NOAA about a hypothesized submarine landslide at Hudson Canyon. This numerical work was carried out in 2013, and a technical memorandum [22] was written. Finally, more recently, a joint work with the Dept Estratigrafia, Paleontologia i Geociènces Marines (GRC Geociènces Marines, Universitat de Barcelona) on a simulation study of the tsunamigenic potential of four submarine landslides located on the Ibiza Channel in the Western Mediterranean Sea will appear (see [23]).

2   Model Equations

Tsunami-HySEA uses the well-known 2D nonlinear one-layer shallow water system in both spherical and Cartesian coordinates. For the sake of brevity and simplicity, only the latter system is written:

$$h_t + (q_x)_x + (q_y)_y = 0$$

$$(q_x)_t + (q_x^2/h + g\,h^2/2)_x + (q_x\,q_y/h\,)_y = ghH_x + S_x$$

$$(q_y)_t + (q_x \, q_y/h \,)_x + (q_y{}^2/h + g \, h^2/2 \,)_y = ghH_y + S_y$$

In the previous set of equations, $h(\boldsymbol{x},t)$, denotes the thickness of the water layer at point $\boldsymbol{x} \in D \subset R^2$ at time t, being D the horizontal projection of the 3D domain where the tsunami takes place. $H(\boldsymbol{x})$ is the depth of the bottom at point $\boldsymbol{x}$ measured from a fixed level of reference. Let us also define the function $\eta(\boldsymbol{x},t) = h(\boldsymbol{x},t)-H(\boldsymbol{x})$ that corresponds to the free surface of the fluid. Let us denote by $q(\boldsymbol{x},t) = (q_x(\boldsymbol{x},t), \, q_y(\boldsymbol{x},t))$ the mass-flow of the water layer at point $\boldsymbol{x}$ at time t. The mass-flow is related to the height-averaged velocity $\boldsymbol{u}(\boldsymbol{x},t)$ by means of the expression $q(\boldsymbol{x},t) = h(\boldsymbol{x},t) \, \boldsymbol{u}(\boldsymbol{x},t)$. The notation $(\ )_t, (\ )_x$ and $(\ )_y$ applies for temporal and spatial partial derivatives in the x and y directions, respectively.

The terms S_x and S_y parameterize the friction effects and two different laws are considered:
- The Manning law:

$$S_x = -gh \, M_n{}^2 \, u_x \, \|u\| \, /h^{4/3}$$
$$S_y = -gh \, M_n{}^2 \, u_y \, \|u\| \, /h^{4/3}$$

where $M_n > 0$ is the manning coefficient.
- A quadratic law

$$S_x = -c_f \, u_x \, \|u\|$$
$$S_y = -c_f \, u_y \, \|u\|$$

where $c_f > 0$ is the friction coefficient.

Finally, we have also used the dispersive non-linear shallow-water system of *Madsen and Sorensen (1992)* to perform BP5.

3 Numerical Solution Method

Tsunami-HySEA solves the two-dimensional shallow-water system using a high-order (second and third order) path-conservative finite volume method. Values of h, q_x and q_y at each grid cell represent cell averages of the water depth and momentum components. The numerical scheme is conservative for both mass and momentum in flat bathymetries and, in general, is mass preserving for arbitrary bathymetries. High order is achieved by a non-linear TVD reconstruction operator of the unknowns h, q_x, q_y and $\eta = h-H$. Then, the reconstruction of H is recovered using the reconstruction of h and η. Moreover, in the reconstruction procedure, the positivity of the water depth is ensured. Tsunami-HySEA implements several reconstruction operators: MUSCL (see *van Leer, 1979*) that achieves second order, the hyperbolic Marquina's reconstruction (see *Marquina, 1994*), that achieves third order, and a TVD combination of piecewise parabolic and linear 2D reconstructions that also achieves third order (see [24]). The high order time discretization is performed using the second or third order TVD Runge-Kutta method described in *Gottlieb and Shu (1998)*. At each cell interface, Tsunami-HySEA uses Godunov's method based on the approximation of 1D projected Riemann problems along the normal direction to each edge. In particular Tsunami-HySEA implements a PVM-type method that uses the fastest and the slowest wave speeds, similar to HLL method (see [25]). A general overview of the derivation of the high order methods is performed in [26]. For large computational domains as the case of the complete scenario in benchmark problem 2 and in the framework of TEWS, Tsunami-HySEA also

implements a two-step scheme similar to leap-frog for the deep water propagation step and a second-order TVD-WAF flux-limiter scheme described in [7] for close to coast propagation/inundation step. The combination of both schemes guaranties the mass conservation in the complete domain and prevents the generation of spurious high frequency oscillations near discontinuities generated by leap-frog type schemes. At the same time, this numerical scheme reduces computational times compared with other numerical schemes, while the amplitude of the first tsunami wave is preserved.

Concerning the wet-dry fronts discretization, Tsunami-HySEA implements the numerical treatment described in [1] and [3], that consists in locally replacing the 1D Riemann solver used during the propagation step, by another 1D Riemann solver that takes into account the presence of a dry cell. Moreover, the reconstruction step is also modified in order to preserve the positivity of the water depth. The resulting schemes are well-balanced for the water at rest, that is, they exactly preserve the water at rest solutions, and are second or third order accurate, depending on the reconstruction operator and the time stepping method. Finally, the numerical implementation of Tsunami-HySEA has been performed on GPU clusters [7, 27, 28] and nested-grids implementation available [9, 14, 15, 16, 18, 19, 22] (nested grids have been used for the complete scenario in benchmark problem 2). These facts allow to speedup the computations, being able to perform complex simulations, in very large domains, much faster than real time [9, 14, 15, 16, 20].

4 Benchmark Problem Comparisons

4.1 Benchmark Problem #1: Steady Flow over Submerged Obstacle

The model setup used was the same as the one provided in the description of the benchmark, with a spatial resolution of 0.0152 m and a mesh composed of 642 by 100 cells. Up to 112 different numerical experiments testing the order of the numerical scheme, the friction law, the values for the friction coefficient and the implementation of the boundary conditions were performed for the workshop. First, second and third order numerical schemes were tested, quadratic and Manning friction laws were considered, with up to 12 different friction coefficients ranging from the inviscid case, and then from c_f=0.05 up to a value of *0.015* with a step of *0.001* were used, and finally three implementations of the same input/output boundary conditions (ghost cells and sponge layers) were tested. The first conclusion extracted is the high sensibility of this test problem (to the numerical method, boundary conditions, and friction). In particular, concerning the open boundary conditions, any perturbation not leaving the computational domain will highly interfere with the numerical solution. This fact makes it crucial the ability of the implemented the boundary conditions to let these perturbations to move out of the computational domain, avoiding undesired spurious reflections to take place. Depending on this, the numerical solution will be more or less affected.

Some conclusions that we outlined from our numerous numerical experiments were the following: 1) concerning the order of the numerical scheme, first order schemes must be ruled out, as they are found too diffusive (at least for the mesh resolution considered here); third order schemes do not necessarily do better as they require a more accurate imposition of the boundary conditions; 2) concerning the friction, a high sensitivity of the numerical solutions for low values of the friction coefficient and much lower sensitivity for higher values was found. For this latter case, regular periodic solutions appear. For the third order scheme this is fully true when the 2-sponge boundary

condition is imposed, but not that much for the other two boundary conditions (ghost cells and 1-sponge BC), for which frequency is more affected; and 3) concerning the boundary conditions, how they are implemented is crucial. This benchmark problem is so sensitive to minor changes that, if perturbations do not move out from the computational domain through the open boundaries and they are reflected, even in a really small amount, this will affect the numerical solution. Finally, and disappointingly, we do not have a choice for the optimal solution. Depending on what is the preferred feature of the observed time series the one we want to better capture (amplitude or frequency) we select the second order scheme with the 2-sponge layer BC and $M_n=0.01$ or the third order scheme with the 2-sponge layer BC and various possible c_f values, for example 0.01. In Figure 1, the first one of these two choices (the second order scheme numerical results) is compared with the measured data at location 1 and 2. For this case amplitude is better captured but not frequency. To check the results for the third order scheme, for which frequency is closer to measurements, see presentation file. Finally, although we performed the sensitivity analysis using the quadratic law, we ended having the feeling that the Manning law is more suitable to get closer to measurements results in this BP. To clearly assess this assertion, we will perform a similar sensitivity analysis for this BP using the Manning law.
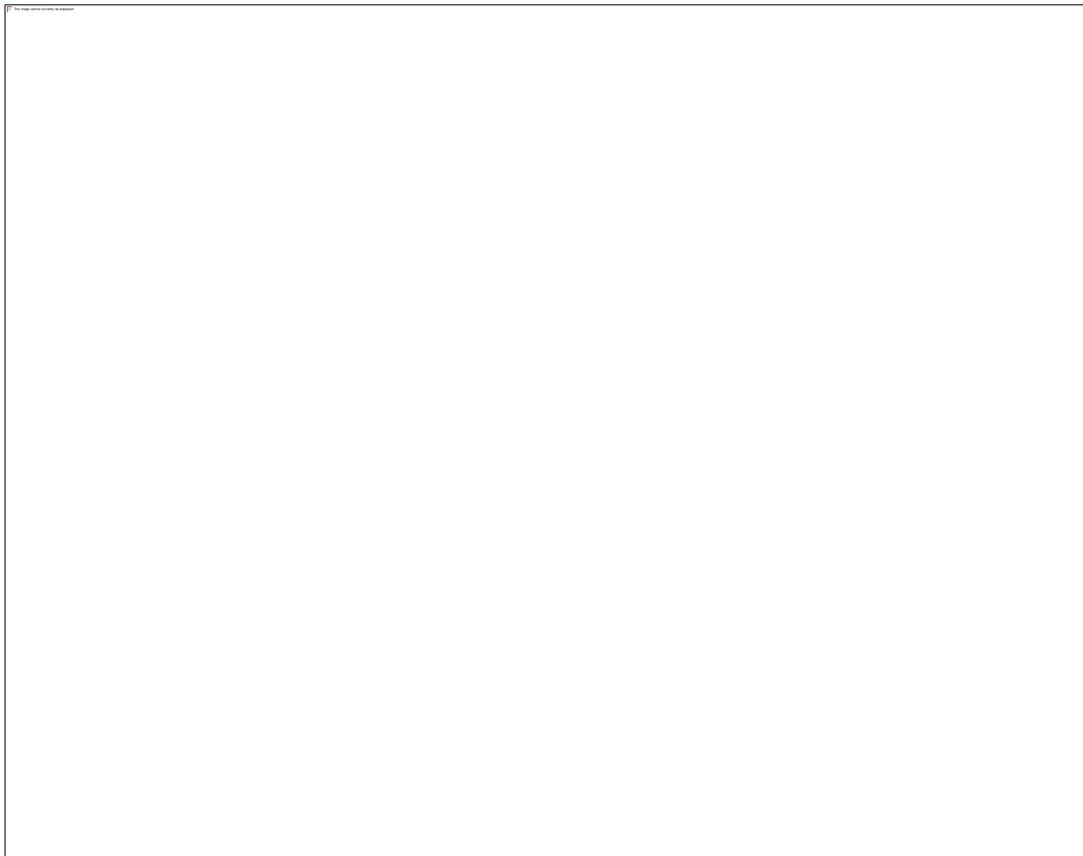
Figure 19. Experimental data (dots) and numerical simulation (solid line, not shown) for a) *u* velocity component at time series location 1, b) *v* velocity component at time series location 1, c) *u* velocity component at time series location 2, and d) *v* velocity component at time series location 2.

4.2 Benchmark Problem #2: Tsunami Currents in Hilo Harbor

Numerical results for the three requested resolutions (2/3, 1/3 and 1/6 arc-sec) were computed and a sensitivity study to friction with values for *n=0.025* (requested), *0.030* and *0.035* was performed. For the local results in the reduced domain (mandatory), the boundary condition aimed at reproducing the sea surface elevation provided at the control point was set by imposing at the upper grid boundary the same time series provided for the control point. As result a good match with the time series at control point (not shown) was obtained. For the **complete scenario** (optional), three nested meshes where used with decreasing resolutions of 128/3, 8/3 arc-sec and for the finer grid the same three resolutions as for the local case were used (2/3, 1/3 and 1/6 arc-sec). Spatial resolution of outer meshes was also varied to 256/3 and 16/3 in order to assess the role of "ambient" meshes resolution in model results. Two Tohoku 2011 sources, one from NOAA and another from GeoClaw, were used.

Some conclusions can be extracted from the numerical results. First for the **reduced scenario**, at HA125 the two initial perturbations in the *u* and *v* components of the velocity are well captured, then the simulated *u* component becomes too oscillatory. In general the effects of varying friction and increasing resolution are very limited, and they are only slightly felt in the maximum and minimum values of the time series (in speed and surface elevation). The observed behavior for HA126 numerical results is similar to the one described for HA125. But in this case larger differences are observed for different values of the friction parameter and increased resolution. The differences for the maximum speed maps between the 20m and 5m resolution simulation on the one hand and the 10m minus 5m resolution simulation on the other, suggest convergence of the numerical solution. Hilo TG fit is pretty good. In what respect the **complete scenario**, simulated from the source, the computed variables reproduce well the first two or three initial waves, in particular for the sea surface elevation in the control point. At HA125 the simulated signal is less oscillatory than in the local scenario and mesh refinement has a minor effect and depending on the sampling (see comments of other modelers), the *v* component of the speed is well captured or highly overestimated but for the first perturbation. Again, at HA126, larger but still limited sensitivity to mesh refinement is observed. The bad news come when trying to assess sensitivity to the ambient and intermediate mesh resolutions: Much larger sensitivity is now observed, meaning that the "ambient" resolution is important and that the outer meshes can not be very coarse, something we would like to have in order to speedup computations. On the other hand, in [14] is also shown that going beyond a certain resolution is also useless. All this, while the role if increasing inner resolution remains limited (for the three resolutions considered here). Finally, two different sources where used for the **complete scenario.** Both simulations surprisingly agree quite well, despite the differences in the sources. In general, time series for the velocity components obtained when GeoClaw source is imposed are more oscillatory, mainly for the *u* component, but both simulations produce good results.

Figure 20. Measured data (dashed line) and numerical simulation (solid line) at the harbor tide gage (top), HA25 ADCP (middle), and HA26 ADCP (bottom).

Figure 21. Maximum predicted fluid speed during entire duration of the 10-m resolution simulation.

4.3 Benchmark Problem #3: Tsunami Currents in Tauranga Harbor

This benchmark provides the data for comparison with a field database recording the Japan 2011 tsunami in Tauranga Harbor, New Zealand. The aim of this test is to attempt to include the effects of the tides. The model setup used is the one proposed in the benchmark description. A rotated domain of 40 km by 20 km with a 20 m numerical resolution was used (bathymetry data resolution 10 m), resulting in a 2,000,000 cell size problem. The boundary condition imposed at the "upper" boundary was the time series recorded at A Beacon for: 1) only tide, 2) only tsunami and 3) the combined tide+tsunami signals, depending on the simulated scenario.

The numerical results show a good agreement with measured data both for free surface elevation at the four tidal stations and for the three different configurations (tide only, tsunami only and tide plus tsunami signal). In Figure 4, measured vs simulated tsunami-only signal at the four tidal stations is shown (left column panel) and for tsunami+tide signal (right column panel). Finally, Figure 5 depicts the comparison between depth-average horizontal velocity data at ADCP location and simulated depth-average velocity, showing numerical results good agreement with observed data.

Figure 22. Comparison of the free surface elevation at the 4 tidal stations for tsunami-only signal and tsunami+tide signal.
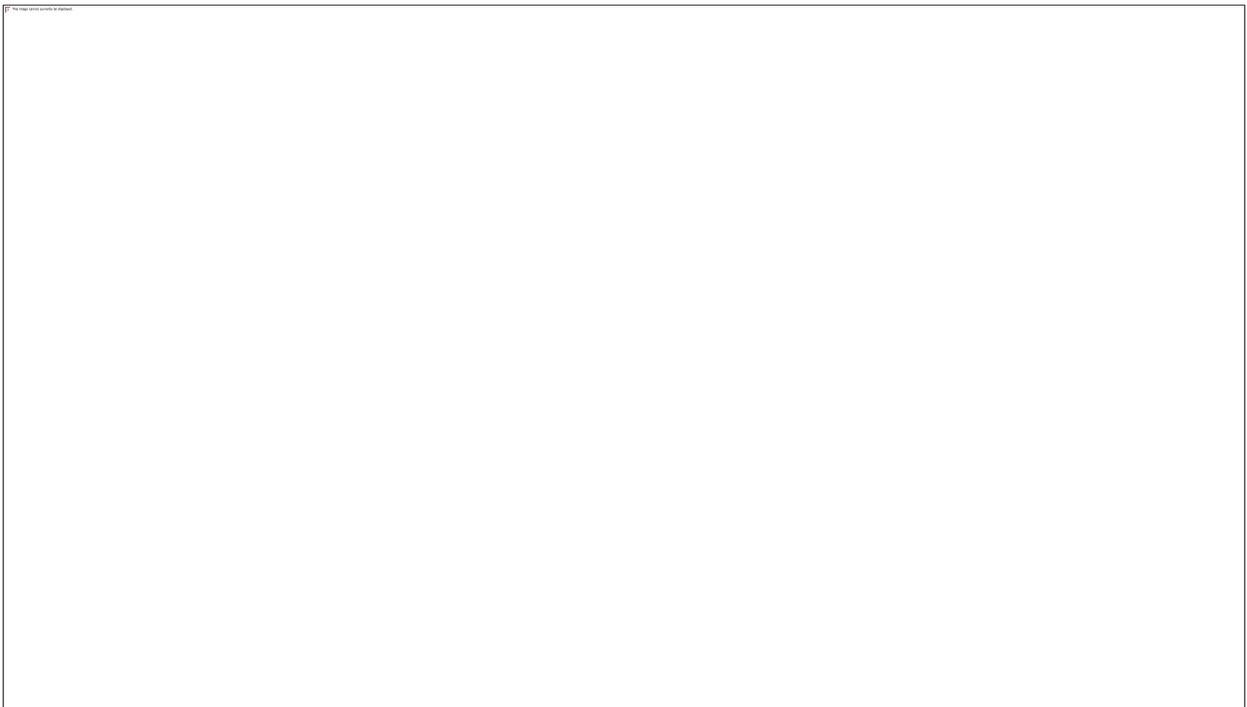
Figure 23. Depth average horizontal velocity comparison HySEA model-ADCP data.

117

4.4 Benchmark Problem #4: Flow through a City Building Layout

This benchmark consists in a single-long period wave propagating up a piecewise linear slope and onto a small-scale model of the town of Seaside, Oregon. For numerically generating this wave we chose the second option of the two proposed approaches: Imposing the time series of incident wave elevation at x=5 cm to force the model at x=5 cm. Several model configurations have been considered. Two numerical resolutions were set: 1cm and 2cm. Three numerical schemes used: first order, second order and WAF. The numerical results presented here are for the second order scheme. Several values for the friction parameter were considered, ranging from 0.01 to 0.035. We also questioned ourselves about the spatial variability of the simulated variables slightly moving the sampling location in the y direction (by 4 cm).

The first remark concerns the simulated signal at the control point compared with the measured one. The exact arrival time is not well captured nor the train of waves between t=35 and 40 sec. This fit cannot be arranged by simply changing the shape for the initial condition, but need of the used of a dispersive model. For the initial phase of the propagation of the generated wave dispersion is important. Nevertheless, we observed that, in this case, including dispersion in the model is not mandatory in order to get good agreement with measured data. In the numerical results we found out that for location B1 flow depth and momentum flux where very sensitivity to small variations in the y-direction of the position of the sampling point, getting a much better fit for points moved slightly "downwards". This analysis of the spatial variability of the simulated variables was performed motivated by the fact that, while the flow depth at locations B4, B6 and B9 fit well, it was clearly underestimated for the first location, B1. We checked out that slightly moving the sampling point downwards resulted in a much better fit with measured data (not shown, but can be found in the presentation slides). In Figure 6, the comparison between measured data (flow depth, velocity and momentum flux) and numerical model for different values of the friction parameter at locations B1 and B4 is shown. Figure 7 depicts the same comparison for locations B6 and B9. At location B9, for simulations performed with low values for the friction (around 0.012) reflected waves can be observed both in flow depth and velocity direction.

Figure 24. Comparison of measured flow depth, cross-shore velocity and cross-shore momentum flux with numerical results for varying friction coefficients for B1 and B4 locations.
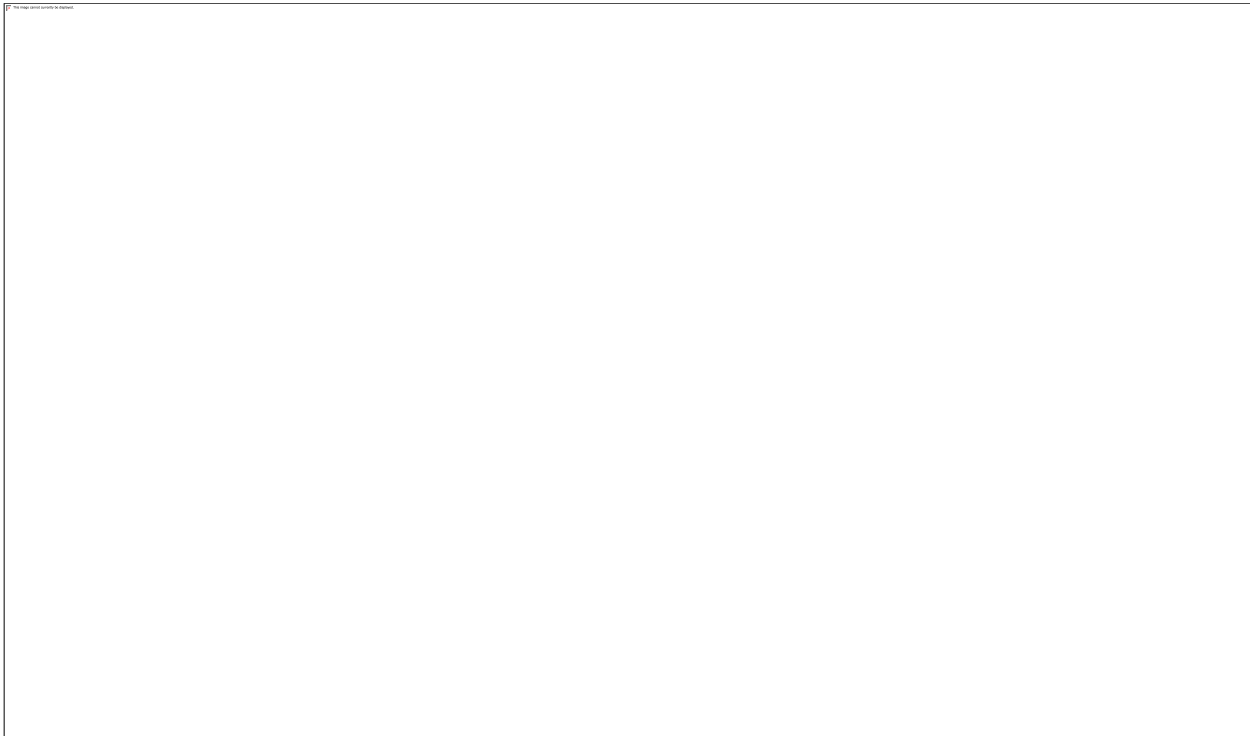
Figure 25. Comparison of measured flow depth, cross-shore velocity and cross-shore momentum flux with numerical results for varying friction coefficients for B6 and B9 locations.

4.5 Benchmark Problem #5: Solitary Wave Propagation over a Complex Shelf

This benchmark consists in a single solitary wave propagating up a triangular shaped shelf with an island feature located at the offshore point of the shelf. As computational domain the extended region [-9,44.6]x[-13,13] was considered. The initial condition for the free surface elevation consisted in a soliton, whose approximate expression taken from *Tonelli and Petti (2009)* is given by:

$$\eta(x,0) = A\ sech\ [(x-x_0)\ \sqrt{(3A/4H^3)}]$$

besides an initial velocity correction is imposed as:

$$u(x,0) = \eta(x,0)\ \sqrt{(gH)}/H$$

with $x_0 = -3.3$ m; $A = 0.39$ m; $H = 0.78$ m; $g = 9.81$ m/s. Thus, the initial conditions imposed were, $h(x,y,0) = \eta(x,0) + 0.78$; $q_x(x,y,0) = h(x,y,0)\ u(x,0)$ and $q_y = 0$. Two NLSW models were used, one with and the other without dispersion. The non-dispersive NLSW model considers two numerical schemes (second and third order), with three mesh resolutions (2.5, 5 and 10 cm) and varying friction ranging from *0.005* to *0.035*. The model including dispersion implements a third order numerical scheme for the NLSW terms and second order for dispersive terms, uses a resolution of 10 cm (490 by 260 cells) and a varying friction ranging from *0.005* to *0.035*. The breaking criteria used, although is not the same, is based on the hybrid criteria from *Kazolea et al. (2014)*. The dispersion coefficient is set to *1/21*.

Some conclusions can be extracted from the numerical experiments performed. First, it should be mentioned that for this problem configuration A/H = 0.5 in the left-hand side of the domain where propagation of the initial perturbation takes place. This makes dispersion mandatory in this part of the domain. But at the same time nonlinearity becomes predominant when approaching the shelf and in the breaking zone. Therefore, a hybrid model is needed to suitably represent both stages of the flow: the dispersive-dominated flow and the non-linear shallow water dominated flow. For numerical comparison, we used first a NLSW model without dispersion. In this case, increasing numerical resolution from 10 cm to 5 cm and 2.5 cm has a minor effect, producing similar (bad) results. Varying friction in the NLSW non dispersive model has negligible effects on points located in front of the obstacle and the effect of varying friction it is mostly felt at points behind the obstacle, more while "more behind" with smaller friction producing results closer to measured data. When the model including dispersion is used much better results, closer to measured data are obtained, mainly for free surface elevation, with larger discrepancies in the *v* component of the velocity. Figure 8 shows the comparison between numerical results and measurements for the free surface elevation at the nine locations considered. For locations in front of the obstacle (*x=7.5* and *x=13m*) the shape and amplitude of the signal is well captured and friction has some minor effect. For points located behind (*x=21* and *x=25m*) friction plays an important role and a better fit to observations is obtained for lower values of friction. The breaking criteria starts acting at the shelf, where the flow becomes shallower, in particular at *y=0m* this happens at *x=13m*. In Figure 8, in the graphic for location *x=13m - y=0m* it can be observed how the breaking criteria starts acting

and the soliton starts to dissipate, while at location *x=7.5m - y=0m* it can be observed how it is fully present. Figure 9 depicts the comparison between model results and measurements for the two components of the velocity at *x=13m y=0m* location. The structure of *u* component is captured but model fails to reproduce the *v* component at this location. Nevertheless, some doubts about the accuracy of the velocity component in the y-direction at ADV1 and ADV2 locations has previously been mentioned (*Shi et al., 2012*), arguing that too small values were recorded.

Figure 26. Comparison of free surface elevation measurements with NLSW dispersive model (varying friction) at the 9 given locations.

121

Figure 27. Comparison of velocity ADV data for location x=13m y=0m and computed values.

5 Conclusions

The overall conclusion that we could extract from this validation exercise was that the Tsunami-HySEA model performed well in all benchmark problems proposed, being the most difficult one the first benchmark. In BP1 turbulent effects and viscosity play an important role and crude shallow water models that only consider friction terms similar to Manning or Darcy law will find it difficult to get numerical results close to measured data. For the rest of the benchmarks no special problems were found. For BP2 -Hilo Harbor- good agreement is obtained for the control point and the tidal station for sea surface elevation. Depth average velocities show a good fit for the initial pattern of the signal (in *u* and *v*), becoming noisier for the *u* component at location HA1125 (see comments of other modelers on data sampling for this case). We analyzed sensitivity to friction and convergence when mesh is refined. Differences in maximum velocity between 20m, 10m and 5m mesh resolutions suggest model convergence. The simulation of the complete scenario from the source in the whole Pacific domain was also performed, obtaining also in this case a good fit for sea surface elevation signals at control point and at Hilo tide station. For the velocity time series, a good agreement of the initial phase of the signal and less oscillatory time series for the *u* component is obtained in this case. Sensitivity to mesh refinement showed minor effects for inner finer meshes and larger effects for the outer coarser ambient meshes. BP3 –Tauranga Harbor- was performed in the three requested configurations (only tsunami, tsunami+tide and only tide). The time series for these three configurations for the sea surface elevation at the four locations considered is very good and also a very good fit is obtained for the speed signal at the ACDP location. For BP4 two numerical resolutions were considered, three numerical schemes used and several values for the friction coefficient imposed. Due to the fact that a good agreement for the three variables considered (flow depth, velocity and momentum flux) were obtained for the three inner locations (B4, B6 and B9) while the flow depth, and consequently momentum flux, were clearly underestimated for the closer to coast location B1, this made us wondering about the spatial variability in the y-direction of the simulated variables. We found out that by slightly moving downwards the location of the sampling point for B1 location we could recover a signal much closer to observations for the sea surface and momentum flux (the velocity signal was good at both

122

locations). At location B9, when low values for the friction parameter are considered (0.012), reflected waves can be observed both in flow depth and velocity signal. Finally, for BP5, shallow water equations without and with dispersion (*Madsen & Sorensen* model) were used, varying friction and resolution. The main conclusion is that dispersion is mandatory in this BP. The exact arrival time and shape is not well captured by the non-dispersive NLSW model, getting a much better agreement for the model with dispersion. Dispersive model results fit to observations is very good for points located in front of the obstacle, including where the process of breaking starts. Besides, at these locations in front of the obstacle, the effect of varying the friction is minor. For points behind the obstacle, results are sensitive to friction and to the breaking criteria used and a better or worse fit to observations depends on the value of friction and on the parameters used in the breaking criteria. For the velocity, at *x=13m y=0m* location, a good fit for the *u* component is obtained while the *v* component is not well captured.

As Tsunami-HySEA is composed of a family of numerical schemes, well adapted to different flow configurations, in general it has produced good results in all the benchmark problems without the need of any new implementation. The sole exception was for BP1, which we found the more difficult one, mainly due to the simplicity of the shallow water model that we used for this test. We think that a better parameterization of the viscous effects should be included in the model in order to obtain a good fit with experimental data. For the rest of the BPs, the use of Tsunami-HySEA was simple and straightforward. Besides, for the very first time we tested a dispersive version of the model and applied to BP5. For large scale, highly computationally demanding problems (as BP2, complete scenario), Tsunami-HySEA performs extremely fast, producing accurate simulations in very short computational times. For such problems nested meshes were used.

6   Acknowledgments

HySEA References

1. M.J. Castro, A. Ferreiro, J.A. García, J.M. González, J. Macías, C. Parés, M.E. Vázquez (2005). On the numerical treatment of wet/dry fronts in shallow flows: Applications to one-layer and two-layer systems. *Math. Comp. Model*. 42 (3-4): 419-439.

2. M. Castro, J.M. González and C. Parés (2006). Numerical treatment of wet/dry fronts in shallow flows with a modified Roe scheme. *Math. Mod. Meth. App. Sci*., 16(6):897-931.

3. J.M. Gallardo, C. Parés and M. Castro (2007). On a well-balanced high-order finite volume scheme for shallow water equations with topography and dry areas. *J. Comp. Phys.,* 227:574-601.

4. E.D. Fernández, F. Bouchut, D. Bresh, M.J. Castro, A. Mangeney (2008). A new Savage-Hutter type model for submarine avalanches and generated tsunami. *J. Comp. Phys*., 227: 7720-7754.

5. M.J. Castro, T. Chacón, E.D. Fernández-Nieto, J.M. González-Vida, C. Parés (2008). Well-balanced finite volume schemes for 2D non-homogeneous hyperbolic systems. Applications to the dam break of Aznalcóllar. *Comp. Meth. Appl. Mech. Eng.,* 197(45):3932-3950.

6. Castro, M.J., de la Asunción, M., Macías, J., Parés, C., Fernández-Nieto, E.D., González-Vida, J.M., Morales, T. (2012). IFCP Riemann solver: Application to tsunami modelling using GPUs. In E. Vázquez, A. Hidalgo, P. García, L. Cea eds. **CRC Press**. Chapter 5, 237-244.

7. M. de la Asunción, M.J. Castro, E.D. Fernández-Nieto, J.M. Mantas, S. Ortega, J. M. González-Vida (2013). Efficient GPU implementation of a two waves TVD-WAF method for the two-dimensional one layer shallow water system on structured meshes. *Computers & Fluids*, 80:441-452.

8. González-Vida, J.M., de la Asunción, M., Castro, M.J., Macías, J., Ortega, S., Sánchez-Linares, C., Arcas, D., Titov, V. (2013). HySEA-Landslide GPU-based model: Validation to the 1958 Lituya Bay mega-tsunami. International Tsunami Symposium (ITS2013). Göcek (Turkey) 25-28 September 2013.

9. Macías, J., Castro, M.J., González-Vida, J.M., Ortega, S., de la Asunción, M. (2013). HySEA-Tsunami GPU-based model. Application to FTRT simulations. International Tsunami Symposium (ITS2013). Göcek (Turkey). 25-28 September 2013.

10. Macías, J., Vázquez, J.T., Fernández-Salas, L.M., González-Vida, J.M., Bárcenas, P., Castro, M.J., Díaz-del-Río, V., Alonso, B. (2015). The Al-Boraní submarine landslide and associated tsunami. A modelling approach. *Marine Geology*, 361:79-95. DOI: 10.1016/j.margeo.2014.12.006.

11. Millán, A. (2014). Estudio y validación de un modelo de volúmenes finitos TVD-WAF 2D de aguas someras para la simulación de tsunamis. Universidad de Málaga. 101 pp.

12. EDANYA Group (2015). Validation and verification of HySEA tsunami model. *In progress.*

13. Macías, J., Castro, M.J., González-Vida, J.M., Ortega, S. (2013). Non-linear Shallow Water Models for coastal run-up simulations. EGU 2013.

14. J. Macías, J.M. González-Vida, A. Mercado, S. Ortega, M.J. Castro (2015). Numerical simulation of LANTEX 2013 tsunami scenario with HySEA model. Impact assessment on Puerto Rico coasts.

15. Macías, J., Castro, M.J., González-Vida, J.M., de la Asunción, M., Ortega, S. (2014). HySEA: An operational GPU-based model for Tsunami Early Warning Systems. EGU 2014.

16. M.J. Castro, J.M. González-Vida, J. Macías, M. de la Asunción, I. Molinari, D. Melini, F. Romano, R. Tonini, S. Lorito, A. Piatanesi (2014). *HySEA-tsunami model: A GPU implementation for the Italian TEWS.* In Proceedings of Perspectives of GPU Computing in Physics and Astrophysics. Rome (Italy), 15-17 September 2014.

17. Castro, M.J., González-Vida, J.M., Macías, J. (2014). Numerical schemes for SW equations aimed for tsunami simulations in the perspective of TEWS. Poster presented at TsuMaMoS 2013 conference. April 2013, Málaga, Spain. https://www.researchgate.net/publication/261696609_Numerical_schemes_for_SW_equations_aimed_for_tsunami_simulations_in_the_perspective_of_TEWS

18. González-Vida, J.M., Macías, J., Ortega, S., Castro, M.J. (2015). Modelling propagation and inundation of the March 2011 Tohoku tsunami with the tsunami-HySEA model. *In progress*.

19. Macías, J. (2014). Tsunami Numerical Simulations: HySEA model. A GPU approach to tsunami modeling and case studies. Experts Meeting Workshop on Tsunami Modeling and Mitigation. Cartagena de Indias (Colombia), 1-3 December, 2014. https://www.researchgate.net/publication/269991081_Tsunami_Numerical_Simulations_HySEA_model._A_GPU_approach_to_tsunami_modeling_and_case_studies

20. C. Sánchez-Linares (2011). Simulación numérica de tsunamis generados por avalanchas submarinas: aplicación al caso de Lituya-Bay. Master report, 87 pages. http://hdl.handle.net/10630/7702

21. González-Vida, J.M., Macías, J., Castro, M.J., Sánchez-Linares, C., de la Asunción, M., Ortega, S., (2015). *The Lituya Bay landslide-generated mega-tsunami. Numerical simulation and sensitivity*

analysis. In progress. A preliminary version of this work can be found at: https://www.researchgate.net/publication/265250059_The_Lituya_Bay_landslide-generated_mega-tsunami._Numerical_simulation_ and_ sensitivity_analysis#share

22. de la Asunción, M., Castro, M.J., González-Vida, J.M., Macías, J., Ortega-Acosta, S., Sánchez-Linares, C. (2013) "East Coast Non-Seismic Tsunamis: A first landslide approach". The memorandum can be downloaded at: https://www.researchgate.net/publication/265250441_East_ Coast_Non-Seismic_Tsunamis_A_first_landslide_approach?ev=prf_pub

23. Iglesias, O., Lastras, G., Macías, J., González-Vida, J.M., Casamor, J.L., Costa, S., Canals, M. (2015). Analysis of the tsunamigenic potential of four submarine landslides located on the Ibiza Channel, Western Mediterranean Sea. *In progress.*

24. Gallardo, J.M., Ortega, S., de la Asunción, M., Mantas, J.M. (2011). Two-dimensional compact third-order polynomial reconstructions. Solving non-conservative hyperbolic systems using GPUs. *J. Sci. Comput.,* 48:141-163.

25. Castro, M.J., Fernández-Nieto, E. D. (2012). A class of computationally fast first order finite volume solvers: PVM methods. *SIAM J. Sci. Comput.,* 34:A2173-2196.

26. Castro M.J., Fernández-Nieto E.D, Ferreiro A.M., García Rodríguez J.A., Parés C. (2009). High order extensions of Roe schemes for two-dimensional non-conservative hyperbolic systems. *J. Sci. Comput.,* 39(1):67-114.

27. Asunción, M., Mantas, J.M, Castro, M.J. (2011). Simulation of one-layer shallow water systems on multicore and CUDA architectures. *J. Supercomput.,* 58:206-214.

28. Castro, M.J., Ortega, S., Asunción, M., Mantas, J.M., Gallardo, J.M. (2011). GPU computing for shallow water flow simulation based on finite volume schemes. *Comptes Rendus Mécanique*, 339:165-184.

Other References

29. Fritz, H.M., Hager, W.H., Minor, H.-E. (2001). Lituya Bay case: Rockslide impact and wave run-up. *Science of Tsunami Hazards*, 19(1):3-22.

30. Gottlieb S., Shu C.W. (1998). Total variation diminishing Runge-Kutta schemes. *Math. Comp*., 67: 73-85.

31. Heller, V., Hager, W.H. (2011). Waves types of landslide generated impulse waves. *Ocean Eng.*, 38(4):630-640.

32. Kazolea, M., Delis, A.I., Synolakis, C.E. (2014). Numerical treatment of wave breaking on unstructured finite volume approximations for extended Boussinesq-type equations. *J. Comp. Phys.*, 271:281-305.

33. Madsen P.A., Sorensen O.R. (1992). A new form of the Boussinesq equations with improved linear dispersion characteristics. Part 2: A slowing varying bathymetry. *Coast. Eng.*, 18: 183-204.

34. Marquina A. (1994). Local piecewise hyperbolic reconstructions for nonlinear scalar conservation laws, *SIAM J. Sci. Comput*., 15:892-915.

35. Shi, F., Kirby, J.T., Harris, J.C., Geiman, J.D., Grilli, S.T. (2012). A high-order adaptive time-stepping TVD solver for Boussinesq modeling of breaking waves and coastal inundation, *Ocean Model.*, 43-44:36-51.

36. Synolakis, C.E., Bernard, E.N., Titov, V.V., Kânoğlu, U., González, F. I. (2008). Validation and verification of tsunami numerical models, *Pure Appl. Geophys*., 165(11–12):2197–2228.

37. Tonelli, M., Petti, M. (2009). Hybrid finite-volume finite-difference scheme for 2DH improved Boussinesq equations, *Coast. Eng*., 56:609-620.

38. van Leer, B. (1979). Towards the Ultimate Conservative Difference Scheme, V. A Second Order Sequel to Godunov's Method. *Com. Phys*., 32:101-136.

pCOULWAVE Benchmark Results

Patrick J. Lynett[a]

[a] University of Southern California, Tsunami Research Center, Los Angeles, CA 90089

Abstract. In this report, the Boussinesq-type model pCOULWAVE is used to study two benchmark problems. The pCOULWAVE model is somewhat unique in that it has been formulated specifically to include physics relevant to shallow, rotational flow. The numerical solution scheme is high-order, with a Finite-Volume representation in space and a forward-marching, implicit and iterative time integration. Both time and space accuracy is fourth-order. Agreement with measured data in the benchmark problems is, in general, very good, and the model demonstrates an ability to capture the current field under long waves in the coastal zone.

Address all correspondence to: Patrick Lynett, University of Southern California, Department of Civil and Environmental Engineering, Los Angeles, CA 90089. Phone: 213-740-3133; email: plynett@usc.edu

1   Model Background

For the work presented here, the Boussinesq-based numerical model pCOULWAVE (Lynett and Liu, 2002) is used. This model solves the fully nonlinear extended Boussinesq equations on a Cartesian grid. A particular advantage of the model is the use of fully nonlinear equations for both deep and shallow water. This avoids the common problem of "splitting" the analysis when the wave reaches shallow water. Applications for which pCOULWAVE has proven accurate include wave evolution from intermediate depths to the shoreline, including parameterized models for wave breaking and bottom friction.

pCOULWAVE is based on the Boussinesq-type equations, which are known to be accurate for inviscid wave propagation from fairly deep water (wavelength/depth ~2) all the way to the shoreline (Wei et al., 1995). The equation model consists of a complex set of partial differential equations that are integrated in time to solve for the free surface elevation and the horizontal velocity vector. A fourth order Adams-Bashforth-Moulton predictor-corrector time integration scheme is required, and fourth-order centered finite differences approximate spatial derivatives. The high order scheme is required owing to the inclusion of first to third order derivatives in the model equations. pCOULWAVE has been used for wave propagation and wave breaking studies (e.g. Lynett and Liu, 2002; Lynett et al., 2003; Korycansky and Lynett, 2005; Lynett and Liu, 2006; Lynett, 2006; Lynett, 2007); wave runup and inundation studies (e.g. Lynett et al, 2002; Lynett et al., 2003; Korycansky and Lynett, 2005; Cheung et al, 2003; Pedrozo-Acuña et al., 2006; Korycansky and Lynett, 2007; Lovolt et al., 2013), tsunami studies (e.g. Geist et al., 2009; Son et al., 2011; Lynett and Liu, 2011; Lynett et al., 2012; Park et al., 2013; Parsons et al., 2014), hurricane wave studies (e.g. Cheung et al., 2003; Augustin et al., 2009; Lynett et al., 2010; Oaks et al., 2012; Irish et al., 2013), and port and harbor modeling (e.g. Son et al., 2011; Lynett et al., 2012; Renteria and Lynett, 2014; Lynett et al., 2014).

2   Model Equations

pCOULWAVE solves the weakly-dispersive, rotational, and turbulent equations of Kim et al. (2009), which are given in conservative form as:
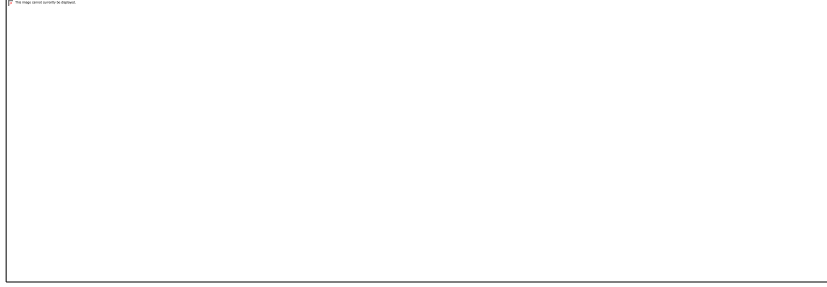
where $H = h + \varsigma$ is the total local water depth, U denotes the velocity at a reference elevation z_a, which varies in time according to $z_\alpha = \varsigma h + (1 + \varsigma)\eta$, with $V = -0.53$. The high-order terms denoted by the script H are extremely tedious and will not be repeated here. In terms of the dissipation mechanisms, bottom friction is included through a standard drag law, which can be easily transformed to model friction through a Manning's coefficient. Subgrid horizontal mixing is captured through a simple Smagorinsky closure, while vertical mixing is coarsely modeled following Elder (1959). A turbulence backscatter model is employed in the model, allowing for the initiation of large-scale coherent features and a reverse-energy cascade. Dissipation due to wave breaking is included through a set of transport equations, with empirically tuned coefficients that govern the onset and conclusions of a breaking event; however this breaking model is relevant to the benchmark problems studied here.

3   Numerical Solution Method

The fourth-order accurate Monotone Upstream-centered Schemes for Conservation Laws (MUSCL) FVM with Harten-Law-van Leer (HLL) Riemann solver is used for the leading-order terms in the depth-integrated equations. For the high-order terms, fourth-order finite volume discretization equations are used. The time integration utilizes the third-order Adams–Bashforth predictor and the fourth-order Adams–Moulton corrector scheme. A constant time step, based on the CFL condition and the deepest water depth in the domain, was used for all simulations.

However, in this numerical scheme which combines the Riemann solvers and MUSCL scheme, there can occur unphysical oscillations when applied on rapidly changing bathymetry. One option to mitigate this issue is use of the Surface Gradient Method (Zhou et al., 2001), which can eliminate these oscillations, but requires that the bathymetry varies continuously. In this paper, a modified version of the Surface Gradient Method, developed by Kim et al. (2008), is used.

4   Benchmark Problem Comparisons

4.1 Benchmark Problem #1: Steady Flow over Submerged Obstacle

pCOULWAVE was set up following the tank geometry. To generate the current, a modified internal source function was used; the amplitude of this function required interactive tuning for each different bottom friction model and value. Consistent with the use of an internal source function, outgoing energy was absorbed using sponge layers. First, as a test of the importance of numerical dissipation, a simulation was run with all dissipation models turned off. With no limiters

used, simulations crash due to instabilities at island apex, for resolutions smaller than 0.02 m. When using the minmod limiter (van Leer, 1979), stable results can be achieved to resolutions of 0.01 m, but no numerical convergence (in the deterministic sense) is found. The wake behind the island is entirely chaotic, with large and irregular eddies generated.

When including the bottom friction models, the numerical results begin to resemble the physical expectations. When using the roughness height friction model (i.e. friction factor from the Moody Diagram), numerically convergent results (after spin-up) are found at a resolution of 0.015 m, and inclusion of the backscatter model yields the best results (see Figure 1). Numerical convergence (in the deterministic sense) was not found with prescribed Mannings or friction coefficient due to the formation of a chaotic wake. Through examination of the range of Reynolds numbers found in the wake, it is likely that the bottom friction factor varies between 0.012 and 0.04 as the flow oscillates. This temporal and spatial variation of bottom stress should be important to the generation of shear layers, and can not be captured with a uniform bottom friction coefficient.
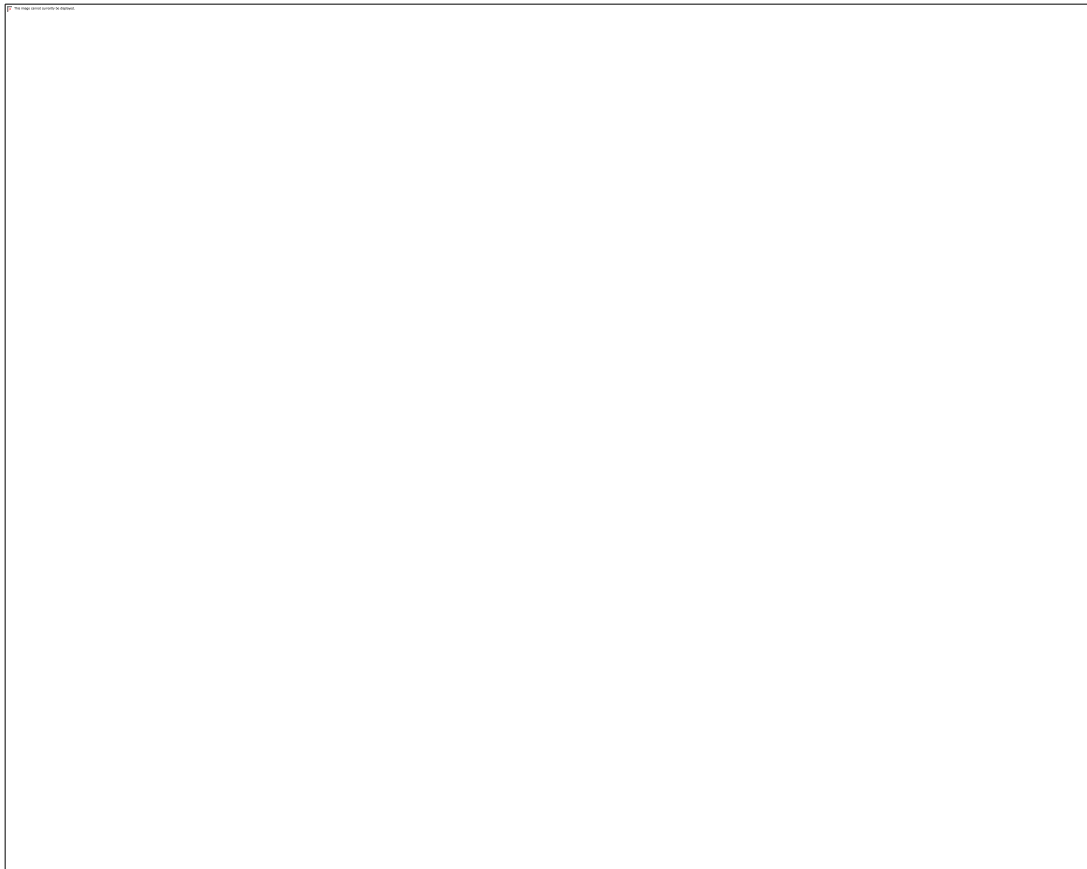

Figure 28. Experimental data (dots) and numerical simulation (solid line, not shown) for a) U velocity component at time series location 1, b) V velocity component at time series location 1, c) U velocity component at time series location 2, and d) V velocity component at time series location 2.

4.2 Benchmark Problem #2: Tsunami Currents in Hilo Harbor

This problem is simulated on a Cartesian grid, with an internal source generator placed inside of the northern boundary. The internal source generator signal is tuned to create the target time series at the Control Point. All boundaries are lined with sponge layers. As prescribed by the problem statement, simulations were run for three different resolutions, all using the same bottom friction coefficient.

Time series comparisons with data are given in Figure 2, and the maximum predicted flow speed in the simulation is shown in Figure 3. Free surface elevation predictions and velocity predictions in regions not effected by eddies show convergence with grid resolutions of no less than 20 m. In regions that are effected by eddies, there is no numerical convergence in the deterministic sense down to a resolution of at least 5 m. In these regions, variations and data errors are on the order of 50-100% of the flow speed
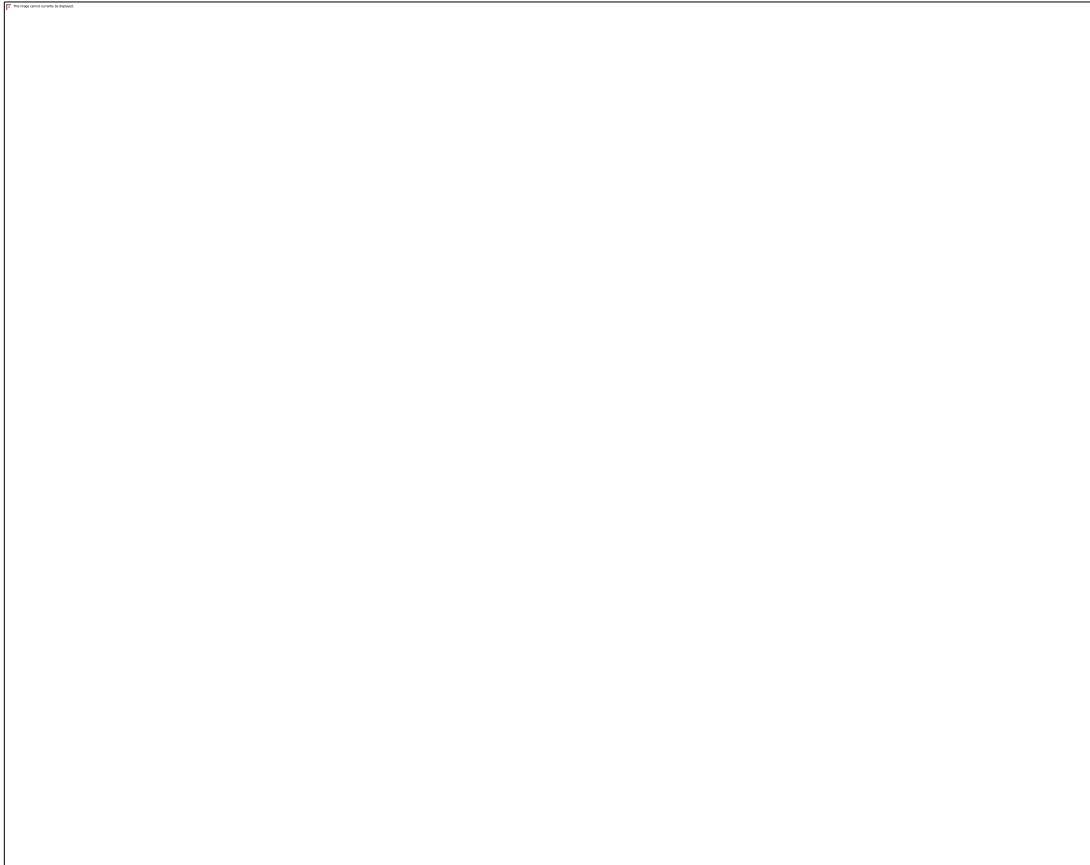
Figure 29. Measured data (dashed line) and numerical simulation (solid line) at the harbor tide gage (top), HA25 ADCP (middle), and HA26 ADCP (bottom).

Figure 30. Maximum predicted fluid speed (m/s) during entire duration of the 10-m resolution simulation.

5   Conclusions

pCOULWAVE appears to be able to accurately capture the complex flow fields under long waves in shallow water. Agreement with the first Benchmark Problem was excellent, while using the bottom friction coefficient as specified by the measured bottom roughness height. Numerical convergence for two benchmark problems was as expected, although the Benchmark Problem #2 results indicate that for many situations related to tsunamis in harbors, convergence cannot be achieved in any deterministic sense.

References

1. Augustin, L. N., Irish, J. L., and Lynett, P. (2009). "Laboratory and Numerical Studies of Wave

    Damping by Emergent and Near-Emergent Wetland Vegetation." Coastal Engineering, v. 53(3), p.

    332-340.

2. Cheung, K.F., Phadke, A.C., Wei, Y., Rojas, R., Douyere, Y.J.-M., Martino, C.D., Houston, S.H.,

Liu, P.L.-F., Lynett, P.J., Dodd, N., Liao, S., and Nakazaki, E., 2003, Modeling of storm-induced coastal flooding for emergency management: Ocean Engineering, v. 30, p. 1353-1386.

3. Geist, E., Lynett, P., and Chaytor, J. (2009). "Hydrodynamic Modeling of Tsunamis from the Currituck Landslide." Marine Geology, v. 264 (1-2), p. 41-52.

4. Irish, J., Lynett, P., Weiss, R., Smallegan, A., and Cheng, W., (2013) "Buried relic seawall mitigates Hurricane Sandy's impacts." Coastal Engineering, v. 80, pp. 79-82, doi: 10.1016/j.coastaleng.2013.06.001

5. Kennedy, A.B., Chen, Q., Kirby, J.T., and Dalrymple, R.A., 2000, Boussinesq modeling of wave transformation, breaking and runup: I. one dimension: Journal of Waterway, Port, Coastal, and Ocean Engineering, v. 126, p. 39-47.

6. Korycansky, D.G., and Lynett, P.J., 2005, Offshore breaking of impact tsunami: The Van Dorn effect revisited: Geophysical Research Letters, v. 32, p. doi:10.1029/2004GL021918.

7. Korycansky, D.G., and Lynett, P.J., 2007, Run-up from impact tsunami: Geophysical Journal International, v. 170, p. 1076-1088.

8. Lovolt, F., Pedersen, G., and Lynett, P. (2013) "Simulating run-up on steep slopes with operational Boussinesq models; capabilities, spurious effects and instabilities." Nat. Hazards Earth Syst. Sci., v. 20, pp. 379-395, doi:10.5194/npg-20-379-2013

9. Lynett, P., 2006, Nearshore wave modeling with high-order Boussinesq-type equations: Journal of the Waterways and Harbors Division, A.S.C.E., v. 132, p. 348-357.

10. Lynett, P., 2007, The effect of a shallow water obstruction on long wave runup and overland flow velocity: Journal of Waterway, Port, Coastal, and Ocean Engineering, v. 133, p. 455-462.

11. Lynett, P., Borrero, J.C., Liu, P.L.F., and Synolakis, C.E., 2003, Field survey and numerical simulations: A review of the 1998 Papua New Guinea tsunami: Pure and Applied Geophysics, v. 160, p. 2119-2146.

12. Lynett, P., and Liu, P.L.F., 2002, A numerical study of submarine-landslide-generated waves and run-

up: Proceedings of the Royal Society of London, A, v. 458, p. 2885-2910.

13. Lynett, P. J., and P. L.-F. Liu (2005), A numerical study of run-up generated by three-dimensional landslides, J. Geophys. Res., 10, doi:10.1029/2004JC002443.

14. Lynett, P., and Liu, P.L.F., 2006, Three-dimensional runup due to submerged and subaerial landslides, in Mercado, A., and Liu, P.L.F., eds., Caribbean Tsunami Hazard: Singapore, World Scientific Publishing Co., p. 289-307.

15. Lynett, P.J., Wu, T.-R., and Liu, P.L.-F., 2002, Modeling wave runup with depth-integrated equations: Coastal Engineering, v. 46, p. 89-107.

16. Lynett, P., Melby, J., and Kim, D.-H., (2010) "An Application of Boussinesq Modeling to Hurricane Wave Overtopping and Inundation." Ocean Engineering, v. 37, p. 135-153. doi: 10.1016/j.oceaneng.2009.08.021

17. Lynett, P., and Liu, P. L.-F. (2011) "Simulation of Complex Tsunami Behavior." Computing in Science and Engineering Magazine, July/August 2011, v. 13(4), pp. 50-57, doi: 10.1109/ MCSE.2011.22

18. Lynett, P., Weiss, R., Renteria, W., De La Torre Morales, G., Son, S., Arcos, M., and MacInnes, B. (2012) "Coastal Impacts of the March 11th Tohoku, Japan Tsunami in the Galapagos Islands. " Pure and Applied Geophysics, doi: 10.1007/s00024-012-0568-3.

19. Lynett, P., Borrero, J, Weiss, R., Son, S., Greer, D., and Renteria, W. (2012) "Observations and Modeling of Tsunami-Induced Currents in Ports and Harbors." Earth and Planetary Science Letters, v. 327/328, pp. 68-74, doi: 10.1016/j.epsl.2012.02.002, 2012.

20. Lynett, P., Borrero, J., Son, S., Wilson, R., and Miller, K., (2014) "Assessment of the Tsunami-Induced Current Hazard." Geophysical Research Letters, doi: 10.1002/2013GL058680.

21. Park, H., Cox, D., Lynett, P., Wiebe, D., and Shin, S. (2013) "Tsunami Inundation Modeling in Constructed Environments: A Physical and Numerical Comparison of Free-Surface Elevation, Velocity, and Momentum Flux." Coastal Engineering, v. 79, pp. 9-21, doi:

10.1016/j.coastaleng.2013.04.002

22. Parsons, T., Geist, E., Ryan, H., Lee, H., Haeussler, P., Lynett, P., Hart, P., Sliter, R., and Roland, E. (2014) "Source and progression of a submarine landslide and tsunami: the 1964 Great Alaska earthquake at Port Valdez." in press for JGR-Solid Earth

23. Pedrozo-Acuña, A., Simmonds, D.J., Otta, A.K., and Chadwick, A.J., 2006, On the cross-shore profile change of gravel beaches: Coastal Engineering, v. 53, p. 335-347.

24. Renteria, W. and Lynett, P. (2014) "Assessment of the Chile 2010 and Japan 2011 Tsunami Events in the Galapagos Islands." in AGU Monograph Series, special issue on the Galapagos Islands.

25. Son, S., Lynett, P., and Kim, D.-H. (2011) "Nested and Multi-Physics Modeling of Tsunami Evolution from Generation to Inundation." Ocean Modelling, v. 38 (1-2), p. 96-113, doi: 10.1016/j.ocemod.2011.02.007

26. Wei, G., Kirby, J.T., Grilli, S.T., and Subramanya, R., 1995, A fully nonlinear Boussinesq model for surface waves. Part 1. Highly nonlinear unsteady waves: Journal of Fluid Mechanics, v. 294, p. 71-92

FUNWAVE-TVD Benchmark Results

James T. Kirby,[a] Stephan T. Grilli,[b] Fengyan Shi,[a] Babak Tehranirad[a], Yong Sung Park[c], Michael Shelby[b]

[a]University of Delaware, Center for Applied Coastal Research, Dept. of Civil and Environmental Engineering, Newark DE 19716 USA

[b]University of Rhode Island, Department of Ocean Engineering, Narragansett, RI 02882, USA

[c]University of Dundee, Division of Civil Engineering, Perth Road, Dundee, United Kingdom, DD1 4HN

Abstract. We describe the application of the model FUNWAVE-TVD to the study of the five benchmark test cases established for the NTHMP Current Benchmark Workshop, help in February 2015. FUNWAVE-TVD is a finite volume implementation of the fully nonlinear Boussinesq equations, extended to incorporate damping by bottom friction and wave breaking effects. In the paper, we provide a short history of the model's background followed by descriptions of the model equations and numerical scheme. Then, results for Benchmarks 1-5 are presented. The model is seen to perform well on each of the benchmarks. In Benchmark 5, we also provide a direct comparison of two prevalent methods for handling wave breaking in Boussinesq codes (eddy viscosity and imposition of a hydrostatic approximation) and show that the two methods produce consistent results for the case considered.

Address all correspondence to: James T. Kirby, University of Delaware, Center for Applied Coastal Research, Dept. of Civil and Environmental Engineering, Newark, DE 19716 USA; Tel: +1 302-831-2438; Fax: +1 302-831-1228; E-mail: kirby@udel.edu

1   Model Background

FUNWAVE-TVD is the present stage of evolution of a depth-integrated, fully nonlinear Boussinesq model originally proposed in Wei et al. (1995). The development of the original finite difference form of the model is described by Kennedy et al. (2000) and Chen et al. (2000), and was distributed to the user community as open source code in this form for over a decade, with an extensive list of publications resulting from its worldwide use. The model was extensively rewritten in 2012 using a hybrid finite volume/finite difference TVD scheme in order to take advantage of the stability properties and shock-capturing capabilities of the approach, and to utilize Riemann solvers to improve wetting-drying processes during inundation. The work described here uses a version of the code developed for a Cartesian coordinate system, described by Shi et al. (2012). A corresponding version in spherical polar coordinates for use in ocean scale propagation is described by Kirby et al. (2013).

FUNWAVE-TVD has been used for all propagation and inundation modeling in NTHMP work for the US East Coast. Descriptions of the early stages of this work may be found in Abadie et al. (2012), Grilli et al. (2015) and Tehranirad et al. (2015). The model was previously benchmarked for inundation during the original NTHMP benchmark workshop; detailed results are provided in Tehranirad et al. (2011).

2   Model Equations

FUNWAVE equations follow from the derivation of Chen (2006), extended to include moving reference level as in Kennedy et al. (2001). The depth-integrated volume conservation equation is given by

$$\eta_t + \nabla \cdot \vec{M} = 0 \tag{1}$$

where η is surface elevation and

$$\vec{M} = H(\vec{u}_\alpha + \vec{u}_2)$$

is the horizontal volume flux, $H = h + \eta$ is the total local water depth, $\vec{u}_\alpha$ denotes the velocity at a reference elevation z_a, which varies in time according to $z_a = Vh + (1 + V)\eta$, with $V = -0.53$. $\vec{u}_2$ is the depth averaged $O(\mu^2)$ contribution to the horizontal velocity field, given by

$$\vec{u}_2 = \left(\frac{z_\alpha^2}{2} - \frac{1}{6}(h^2 - h\eta + \eta^2) \right)\nabla B + \left(z_\alpha + \frac{1}{2}(h - \eta) \right)\nabla A$$

where $A = \nabla \cdot (h\vec{u}_\alpha)$ and $B = \nabla \cdot (\vec{u}_\alpha)$.

The depth-averaged horizontal momentum equation can be written as

$$\vec{u}_{\alpha,t} + (\vec{u}_\alpha \cdot \nabla)\vec{u}_\alpha + g\nabla\eta + \vec{V}_1 + \vec{V}_2 + \vec{V}_3 + \vec{R} = 0 \tag{2}$$

where g is the gravitational acceleration and $\vec{V}_1, \vec{V}_2$ and $\vec{V}_3$ are terms representing the dispersive Boussinesq terms given by

$$\vec{V}_1 = \left[\frac{z_\alpha^2}{2}\nabla B + z_\alpha \nabla A \right]_t - \nabla\left[\frac{\eta^2}{2}B_t + \eta A_t \right]$$

$$\vec{V}_2 = \nabla\left[(z_\alpha - \eta)(\vec{u}_\alpha \cdot \nabla)A + \frac{1}{2}(z_\alpha^2 - \eta^2)(\vec{u}_\alpha \cdot \nabla)B + \frac{1}{2}(A + \eta B)^2 \right]$$

$$\vec{V}_3 = \omega_0 \vec{i}_z \times \vec{u}_2 + \omega_2 \vec{i}_z \times \vec{u}_\alpha$$

In which

$$\omega_0 = (\nabla \times \vec{u}_\alpha) \cdot \vec{i}_z = v_{\alpha,x} - u_{\alpha,y}$$

$$\omega_2 = (\nabla \times \vec{u}_2) \cdot \vec{i}_z = z_{\alpha,x}(A_y + z_\alpha B_y) - z_{\alpha,y}(A_x + z_\alpha B_x)$$

In (2), $\vec{R}$ represents diffusive and dissipative terms including bottom friction $\vec{R}_{frc}$, subgrid turbulent mixing $\vec{R}_{sub}$, and breaking induced dissipation $\vec{R}_{brk}$ if the artificial eddy viscosity breaking scheme (Kennedy et al., 2000) is applied. A quadratic form of bottom friction is used as

$$\vec{R}_{frc} = \frac{C_d}{H} | \vec{u}_\alpha | \vec{u}_\alpha$$

where C_d is the friction coefficient, which can be a constant Chezy coefficient or based on Manning's formula described by

$$C_d = \frac{gn^2}{H^{1/3}}$$

where n is Manning's roughness coefficient. For modeling of wave breaking, two options were implemented in the model. One is the natural TVD shock capturing scheme, which switches the Boussinesq equations to the nonlinear shallow water equations at cells where the ratio of surface elevation to water depth exceeds a certain threshold (SWE breaker; Tonelli and Petti, 2009, 2010). The other is the artificial eddy-viscosity breaker (VIS breaker) developed by Kennedy et al. (2000).

3   Numerical Solution Method

In FUNWAVE-TVD, a combined finite-volume and finite-difference method is applied to the spatial discretization. For the flux terms and the first-order derivative terms, a high-order MUSCL-TVD scheme is used. The MUSCL-TVD scheme implemented in the model includes different orders of accuracy from second- to fourth-order (Yamamoto et al., 1993, 1998), which can be chosen by a user. The van-Leer limiter is used for the second- and third-order schemes and the Minmod limiter is used for the fourth-order scheme. The numerical fluxes are computed using a HLL approximate Riemann solver. For time stepping, the third-order Strong Stability-Preserving (SSP) Runge-Kutta scheme (Gottlieb et al., 2001) is adopted. An adaptive time step is chosen following the Courant-Friederichs-Lewy (CFL) criterion. The spatial numerical scheme is of fifth-order accuracy for a smooth gradient of velocity field if the fourth-order scheme is chosen. However, the model accuracy would decrease due to utilizing limiters in the TVD-type scheme. The numerical diffusion is mainly from the reduced numerical accuracy when a sharp gradient of flow field occurs.

A moving shoreline is modeled by a wetting-drying scheme based on the local surface elevation versus water depth. The normal flux at the wet-dry interface is set to zero. A mirror boundary condition is applied to the high-order MUSCL-TVD scheme and discretization of dispersive terms at a moving boundary. The wave speed of the Riemann solver at the wet-dry interface is modified according to Zhou et al. (2001).

4   Benchmark Problem Comparisons

4.1 Benchmark Problem #1: Steady Flow over Submerged Obstacle

FUNWAVE-TVD was set up in a computational domain with a width of 1.52 m and length of 9.78 m. A steady discharge velocity of 0.115 m/s was specified at the upstream boundary. At the downstream boundary, a radiation boundary condition was applied. The radiation boundary condition for the Riemann solver was implemented using the zero-gradient condition for surface elevation and velocity components according to Toro (2009). Several tests were carried out with different bottom friction coefficients (C_d = 0.0, 0.003, 0.006, 0.012), different grid resolutions (0.005 m, 0.01 m, 0.03 m) and CLF conditions (CLF = 0.25, 0.5). The model convergence tests showed that model results were unaffected by the grid size reduction from 0.01 m to 0.005 m and the CLF reduction from 0.5 to 0.25. The optimal bottom friction coefficient was found to be C_d = 0.012 based on model/data comparisons of velocity components at measurement locations.

Figure 31. Experimental data (dots) and numerical simulation (solid line, not shown) for a) U velocity component at time series location 1, b) V velocity component at time series location 1, c) U velocity component at time series location 2, and d) V velocity component at time series location 2.

4.2 Benchmark Problem #2: Tsunami Currents in Hilo Harbor

We simulated this benchmark using FUNWAVE-TVD on regular Cartesian grids with 5, 10, and 20 m resolution. The bathymetry was mapped to the Cartesian coordinate system using a transverse Mercator transformation. The control point lies on the northern boundary of the computational grid, along which the free surface elevation was set to be the same as that of the control point, except for a correction to this elevation introduced to account for shallow water breaking. The horizontal current magnitude was specified along the offshore boundary based on linear long wave theory, for the corresponding elevation, initially in a boundary normal direction. A few iterative simulations were performed to estimate both the reflection coefficient and wave angle of incidence (which affects velocity components), by trial and error.

With this inflow boundary condition, in each grid, the calculated surface elevation at the control point is very close to that provided, with a root-mean-squared (rms) error between the data and the simulation of about 0.08 m for all three grids (the maximum elevation of incident waves was over

1 m). By contrast, the rms error increases at the tidal gauge, to about 0.5 m in each grid, with the maximum elevation of the wave being about 2 m. Effects of grid refinement are more important for the velocity. At the ADCP 1125, the rms difference on velocity magnitude between the 20 and 10 m grids is about 0.01 m/s, whereas it is about 0.06 m/s between the 10 and 5 m grids. At the ADCP 1126, the rms difference between each pair of grids is about 0.06 m/s. Note that, at both locations, the maximum velocity is on the order of 1 m/s.
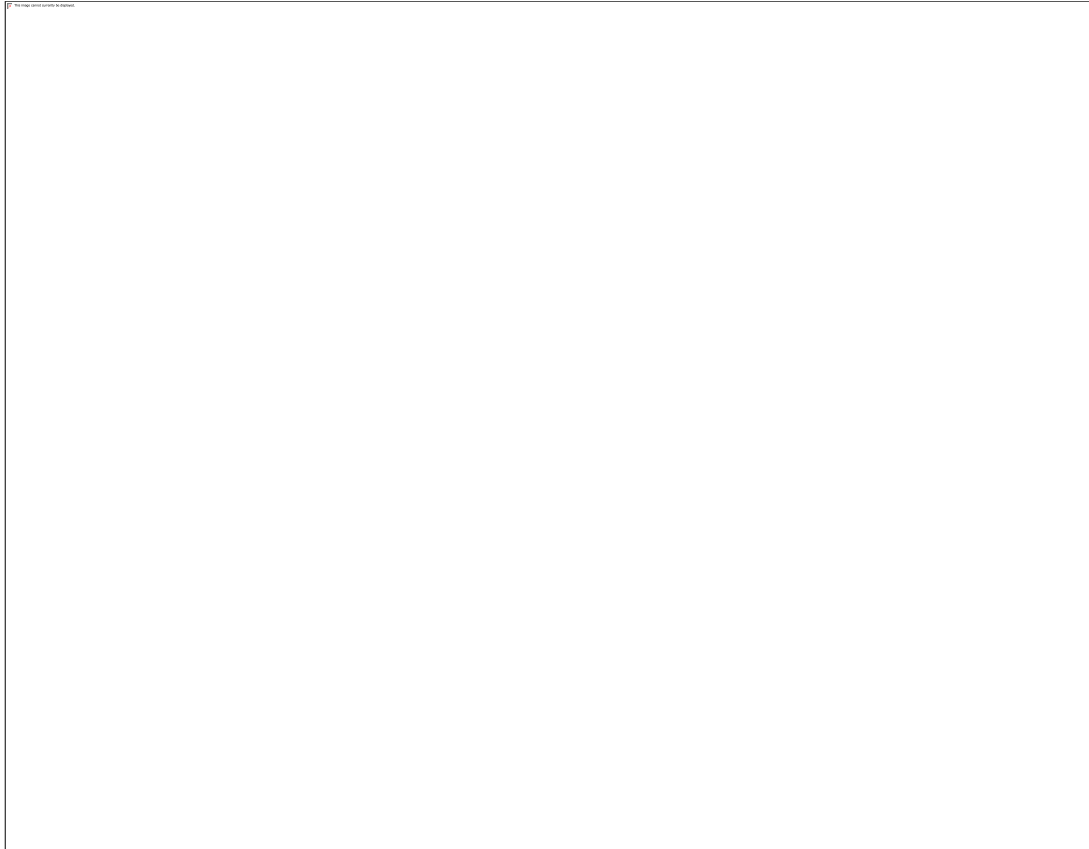
Figure 32. Measured data (dashed line) and numerical simulation (solid line) at the harbor tide gage (top), HA25 ADCP (middle), and HA26 ADCP (bottom).

**Figure 33. Maximum predicted fluid speed (m/s) during entire duration of the 10-m resolution simulation.**

4.3 Benchmark Problem #3: Tsunami Currents in Tauranga Harbor

We simulated tide-tsunami interactions at Tauranga, NZ using FUNWAVE-TVD in a 40 m resolution (948 by 437 cells; SW corner: 37.5248° S, 175.8445° E) Cartesian computational grid with a smaller 10 m resolution grid nested within it, centered about the port of Tauranga (504 by 404 cells; SW corner: 37.6319° S 176.1442° E; Fig. 4). Bathymetry was rotated -49° from north and cropped such that A Beacon (-37.60287, 176.17781) was positioned on the upper boundary of the 40 m grid. Comparisons between measurements of the 2011 Tohoku tsunami and model results were made at four tide gauges (1-4 in Fig. 4) and an ADCP buoy located at the harbor entrance (5 in Fig. 4). Tide and tsunami signals were first modeled independently, then together. In all simulations, bottom friction was computed based on a 0.025 Manning coefficient. An obstacle, defining an internal no-flux boundary was introduced to represent the steep bathymetry at the two loading docks.

Boundary conditions for tsunami modeling were set along the offshore boundary using surface elevation at A Beacon and the corresponding horizontal current magnitude based on linear long wave theory, initially assumed in a boundary normal direction. Computed currents along the boundary did not initially match the specified currents, as a result of the unknown wave direction and interference from wave reflection. Boundary conditions were updated by averaging input and

output currents and rerunning the model using the given surface elevations; this refinement process was repeated several times until results converged. Current and surface elevation data were computed at many numerical gauges along the boundary of the 10 m nested grid, and the model was rerun in it from initial time. Tidal boundary conditions, both elevation and current, were generated along the offshore boundary of the 40 m grid using the Oregon Tide Prediction Software (OTPS; developed at Oregon State University by Erofeeva and Egbert). The tide was similarly modeled in the 40 m grid and in the nested 10 m grid. Finally, the two sets of boundary conditions were linearly combined at the outer boundary of the 40 m grid, and the model was run in both grids.

Fig. 5 (left) shows that surface elevations computed in the combined simulations at Sulphur Point agree well with observations. Nonlinear effects in tide-tsunami simulations can be quantified by comparing surface elevation from the combined simulation to the linear superposition of surface elevation from the tide-only and tsunami-only simulations. Fig. 5 (left) shows that differences are small between these, but are greatest near high tide, as could be expected from the stronger currents. Currents modeled at the entrance to Tauranga Harbor agree well in magnitude with those measured at the ADCP, but the model predicts a change in direction between the ebb and flood currents of 180° instead of the observed 140° (Fig. 5, right).
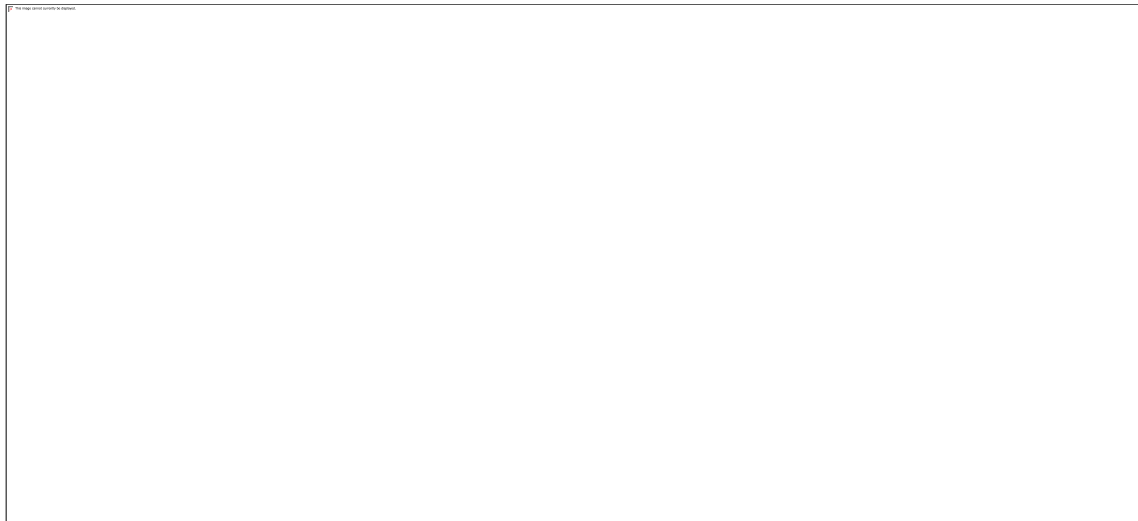
Figure 4. Shore-oriented (x) bathy/topo (color scale in m) of 40 m Cartesian FUNWAVE-TVD grid, with a 10 m nested grid (black box). Locations of measuring equipment are shown as red dots. Tide stations are marked as follows: (1) A Beacon, (2) Tug Berth, (3) Sulfur Point and (4) Moturiki. An ADCP buoy is anchored in the middle of the inlet (slack mooring) at dot marked (5). "A-Bacon" provides the inflow boundary conditions along the upper offshore boundary.
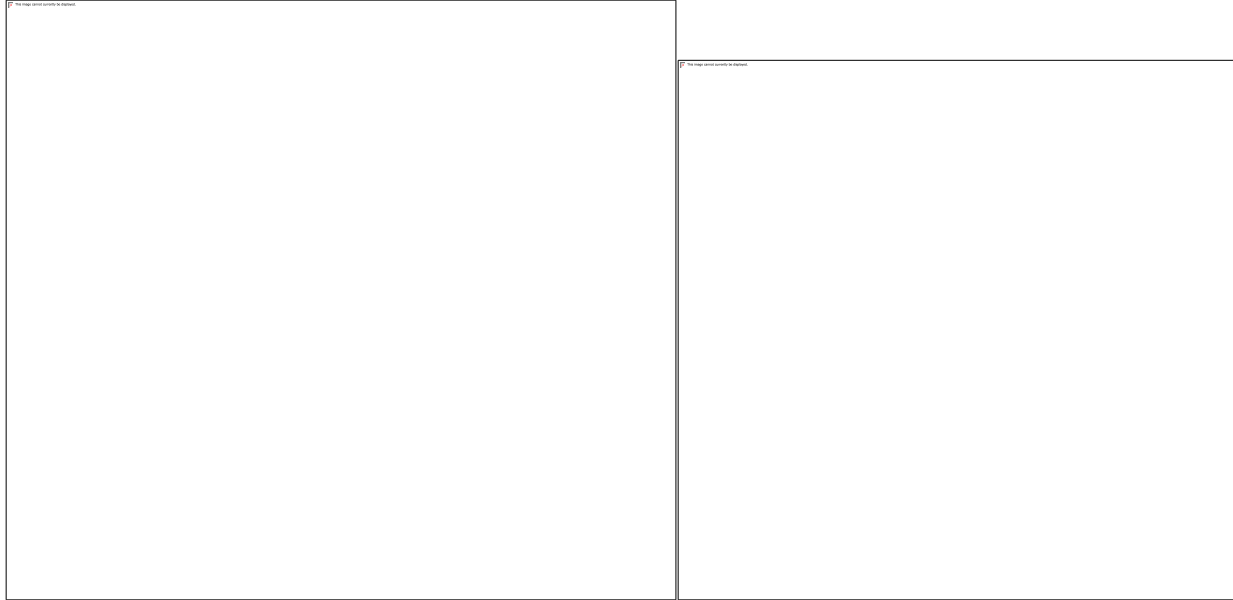
Figure 5. Tide-tsunami simulations: (left) Measured surface elevations at Sulphur Point (black solid line), compared to FUNWAVE-TVD's 40 meter grid results of tide and tsunami alone linearly superimposed (dashed line), and results of simulations using a combined tide-tsunami boundary condition (blue solid line), at three locations: (a) A Beacon, (b) Tug Berth, (c) Sulfur Point. (right) Current magnitude (radial scale in m/s) and direction (deg. in polar diagram) at Tauranga Harbor entrance, modeled (+) and observed (●).

*4.4 Benchmark Problem #4: Flow through a City Building Layout*

For this benchmark, we generate a wave at the left (wavemaker) boundary using the recorded experimental surface elevation data at WG2 close to the wavemaker. A 20 cm wide sponge layer was deployed on the right (shoreline) side of the domain to avoid reflection effects. Several runs were performed to investigate the convergence of the model, and the effect of different drag coefficients on the results was investigated. Results obtained using a grid resolution of 5 cm and drag coefficient $C_d = 0.001$ were chosen for presentation here. These values were similar to numbers that Park et al. (2013) suggested for this case. All model runs were conducted using the experimental DEM as supplied, without any topographic smoothing.

Figure 6 shows the water surface elevation at gauge WG3 (located about half way between the model wavemaker boundary and the still water shoreline) for measured and simulated data, which are in good agreement. Figure 7 shows the comparison between measurements (red) and simulation results (blue) for the gauges B1, B4, B6 and B9. The arrival time of the results are in good agreement with recorded data, as well as maximum values for flow depth, velocity and momentum flux, with less than 20 percent error relative to measured values. There is a marked overprediction of surface elevation and underprediction of cross-shore velocity at gauge B1 after passage of the initial wave crest, which has not been explained. This coincides with an underprediction of flow depth at B4; however, velocities at this second gauge are predicted quite well. The errors noted here are likely due to the interaction of the flow with the detailed geometry

143

of the DEM. Details differ from the results presented in Park et al. (2013), where some degree of topographic smoothing is applied to the DEM.

Figure 6. Comparison between measured (Red) and simulated (Blue) surface elevation for gauge WG3 located in the middle of the domain.
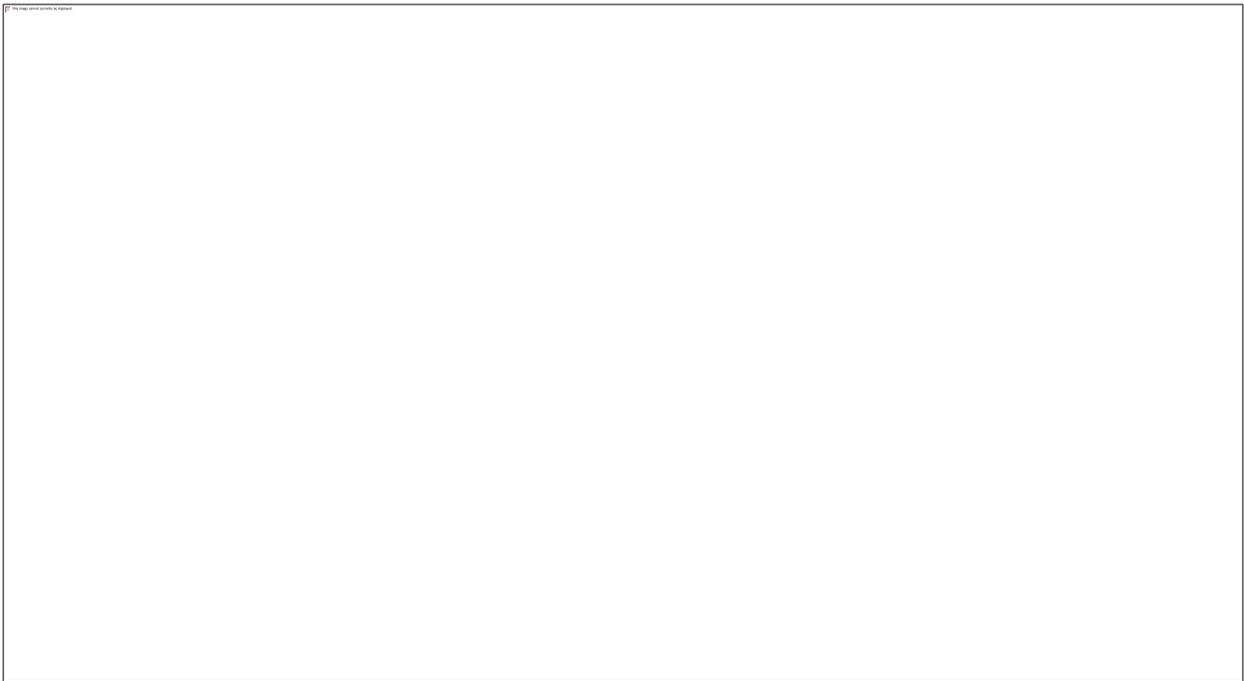
Figure 7. Experimental data (Red) and numerical simulation (Blue) for gauges B1 (Dotted), B4 (Solid), B6 (Dashed) and B9 (Dash-dotted). Depths, velocities and momentum fluxes for each gauge are offset vertically by 0.4 m, 4 m/s and 1 m^3/s^2 respectively,

4.5 Benchmark Problem #5: Solitary Wave Propagation over a Complex Shelf

For FUNWAVE-TVD, the model bathymetry was constructed by extending the bathymetry data to the left by 8.76 m (100 grid points in the model grid) with a constant water depth of 0.78 m in order to initialize the solitary wave on the left side. Grid convergence tests were conducted using two grid resolutions. The tests indicated that the reduction of grid size from dx $= 0.0876$ m, dy $=$

0.1063 m, to 0.0438m and 0.0532m, did not affect model results. The simulations were performed using two wave breaking schemes implemented in FUNWAVE-TVD. One is the natural TVD shock capturing scheme (SWE breaker, Shi et al., 2012). The other is the artificial eddy-viscosity breaker (VIS breaker) developed by Kennedy et al. (2000).

Figure 8 shows time series of surface elevation modeled by the SWE breaker model and the VIS breaker model with comparison to the measurements at Gauges 1-9 (from top to bottom). Both models predict well the solitary wave propagation and its reflection from the shore. The models also capture the collision of edge waves propagating around the two sides of the island, as indicated at the gauge behind the island (Gauge 3). The comparison between the SWE breaker model and VIS breaker model results shows that the surface elevations predicted by the two models are generally identical. Figure 9 shows model/data comparisons of velocity components (u,v) at the ADV 1. Both models predict the peak velocity and the entire trend of velocity variation in time at the measurement location. Again, the results from the two models are basically identical except for slight differences in later time when wave breaking is involved.

The image cannot currently be displayed.

Figure 8. Model/data comparisons of time series of surface elevation at Gauge 1- Gauge9 (from top to bottom). Solid line: data, red dashed line: VIS breaker model, blue dashed line: SWE breaker model.

Figure 9. Model/data comparisons of time series of velocity components (u,v) at ADV 1. Solid line: data, red dashed line: VIS breaker model, blue dashed line: SWE breaker model.

5   Conclusions

Overall, FUNWAVE-TVD has performed satisfactorily in each benchmark test. Possible additional fine tuning of model results could be obtained by using more extensive testing of bottom friction effects. There are also general open research questions regarding the choice of methods for handling breaking in existing Boussinesq models, and additional head to head comparisons of methods described in the literature should be made. Finally, Benchmark 2 involves a great deal of guesswork to establish an input wave condition across a variable depth boundary from the single measurement, a process which is poorly constrained to say the least. It is possible that further improvement in this case would be obtained if an inverse approach, or possibly an ensemble Kalman filter approach were used to constrain an input wave condition with a greater number of degrees of freedom. Accuracy of available bathymetric data should also be verified and could impose a strong controlling factor on model accuracy.

Overall, there is no indication of a need for immediate adjustments or improvements to the model in order to improve performance.

6 Acknowledgments

References

1. Abadie, S., J.C. Harris, S.T. Grilli and R. Fabre 2012. Numerical modeling of tsunami waves generated by the flank collapse of the Cumbre Vieja Volcano (La Palma, Canary Islands) : tsunami source and near field effects. *J. Geophys. Res.*, **117**, C05030, doi:10.1029/2011JC007646.

2. Chen, Q., Kirby, J. T., Dalrymple, R. A., Kennedy, A. B. and Chawla, A., 2000, "Boussinesq modeling of wave transformation, breaking and runup. II: Two horizontal dimensions", *Journal of Waterway, Port, Coastal and Ocean Engineering*, **126**, 48-56.

3. Chen, Q., 2006. Fully nonlinear Boussinesq-type equations for waves and currents over porous beds. *J. Eng. Mech.* **132**, 220–230.

4. Gottlieb, S., Shu, C.-W., Tadmore, E., 2001. Strong stability-preserving high-order time discretization methods. *SIAM Rev*. **43** (1), 89–112.

5. Grilli, S. T., O'Reilly, C., Harris, J. C., Tajalli Bakhsh, T., Tehranirad, B., Banihashemi, S., Kirby, J. T., Baxter, C. D. P., Eggeling, T., Ma, G. and Shi, F., 2015, "Modeling of SMF tsunami hazard along the upper U. S. East Coast: Detailed impact around Ocean City, MD", *Nat. Hazards*, **76**, 705-746, doi: 10.1007/s11069-014-1522-8.

6. Kennedy, A.B., Chen, Q., Kirby, J.T., Dalrymple, R.A., 2000. Boussinesq modeling of wave transformation, breaking and runup. I: 1D. *J. Waterway Port Coastal Ocean Eng., * **126**, 39–47.

7. Kennedy, A.B., Kirby, J.T., Chen, Q., Dalrymple, R.A., 2001. Boussinesq-type equations with improved nonlinear performance. *Wave Motion,* **33**, 225–243.

8. Kirby, J. T., Shi, F., Tehranirad, B., Harris, J. C. and Grilli, S. T., 2013, "Dispersive tsunami waves in the ocean: model equations and sensitivity to dispersion and Coriolis effects", *Ocean Modelling*, **62**, 39-55.

9. Park, H., Cox, D. T., Lynett, P. J., Wiebe, D. M., and Shin, S., 2013, "Tsunami inundation modeling in constructed environments: A physical and numerical comparison of free-surface elevation, velocity, and momentum flux", *Coastal Engineering*, **79**, 9- 21.

10. Shi, F., Kirby, J. T., Harris, J. C., Geiman, J. D. and Grilli, S. T., 2012, "A high-order adaptive time-stepping TVD solver for Boussinesq modeling of breaking waves and coastal inundation", *Ocean Modelling*, **43-44**, 36-51.

11. Tehranirad, B., Shi, F., Kirby, J.T., Harris, J.C., Grilli, S., 2011. "Tsunami benchmark results for fully nonlinear Boussinesq wave model FUNWAVE-TVD, Version 1.0". Research Report No. CACR-11-02, Center for Applied Coastal Research, University of Delaware.

12. Tehranirad, B., Harris, J. C., Grilli, A. R., Grilli, S. T., Abadie, S., Kirby, J. T. and Shi, F., 2015, "Far-field tsunami hazard on the western European and US east coast from a large scale flank collapse of the Cumbre Vieja volcano, La Palma", submitted to *Pure and Applied Geophysics*.

13. Tonelli, M., Petti, M., 2009. Hybrid finite volume-finite difference scheme for 2DH improved Boussinesq equations. *Coastal Eng*. **56**, 609–620.

14. Tonelli, M., Petti, M., 2010. Finite volume scheme for the solution of 2D extended Boussinesq equations in the surf zone. *Ocean Eng*. **37**, 567– 582.

15. Toro, E.F., 2009. *Riemann solvers and numerical methods for fluid dynamics: a practical introduction*, third edition. Springer, New York.

16. Wei, G., Kirby, J.T., Grilli, S.T., Subramanya, R., 1995. A fully nonlinear Boussinesq model for surface waves: Part I. Highly nonlinear unsteady waves. *J. Fluid Mech*. **294**, 71–92.

17. Yamamoto, S., Daiguji, H., 1993. Higher-order-accurate upwind schemes for solving the compressible Euler and Navier–Stokes equations. *Comput. Fluids* **22**, 259– 270.

18. Yamamoto, S., Kano, S., Daiguji, H., 1998. An efficient CFD approach for simulating unsteady hypersonic shock-shock interference flows. *Comput. Fluids* **27**, 571– 580.

19. Zhou, J.G., Causon, D.M., Mingham, C.G., Ingram, D.M., 2001. The surface gradient method for the treatment of source terms in the shallow-water equations. *J. Comput. Phys*. **168**, 1–25.

BOSZ Benchmark Results

Volker Roeber [a], Troy W. Heitmann [b], C. Gabriel David [c], Jeremy D. Bricker [a], Kwok Fai Cheung[b]

[a]Tohoku University, International Research Institute of Disaster Science (IRIDeS), 468-1 E304 AzaAoba, Aramaki, Aoba-ku, Sendai, Japan, 980-0845
[b]University of Hawaii at Manoa, Department of Ocean & Resources Engineering, 2540 Dole Street, Holmes Hall 402, Honolulu, USA, 96822
[c]Franzius-Institute for Hydraulic, Estuarine and Coastal Engineering, Leibniz University of Hanover, Nienburger Straße 4, Hanover, Germany, 30167

Abstract. This document summarizes the performance of the numerical model, *BOSZ*, for the 2015 NTHMP benchmarking challenge for the problems 1, 2, and 5. *BOSZ* is a depth-integrated free-surface resolving numerical code based on a set of extended Boussinesq-type equations. It uses a Finite Volume scheme for the hydrostatic part of the governing equations and a Finite Difference discretization for the parabolic terms. The model handles breaking waves and hydraulic jumps through a Riemann solver. Dissipative terms based on Manning coefficients include the effects of bottom friction. In addition to previous validations with the 2011 NTHMP benchmarking problems for runup and inundation, the presented results highlight the models performance in providing accurate and stable solutions for flow velocities and vortex structures. Overall, *BOSZ* successfully computes complex vortex patterns and the associated flow velocities over a range of grid sizes with realistic Manning's n values. The model can therefore be considered a reliable numerical tool for runup/inundation mapping purposes with accurate representation of nearshore currents and flow velocities.

Address all correspondence to: Volker Roeber, Tohoku University, International Research Institute of Disaster Science (IRIDeS), 468-1 E304 AzaAoba, Aramaki, Aoba-ku, Sendai, Japan, 980-0845; Tel: +81 022-752-2088; Fax: +81 022-752-2088; E-mail: roeber@irides.tohoku.ac.jp

1   Model Background

The *B*oussinesq *O*cean & *S*urf Zone model (*BOSZ*) is a numerical tool for the computation of depth integrated free surface wave equations describing both nonlinear and dispersive wave processes. *BOSZ* was initially designed to provide stable solutions for extreme wave events. Its applications range from computing inundation scenarios and wave processes related to near-field tsunamis, hurricane and large ocean swells to river flooding and ship-borne waves. The model also serves as an educational tool for practical coastal engineering design studies.

The linear performance of the governing equations is identical to that of extended Boussinesq-type equations of Nwogu (1993); however, *BOSZ* utilizes conservative variables for the leading order nonlinear shallow water terms, which provides the foundation for handling sub- and supercritical flows with discontinuities (i.e. breaking waves and hydraulic jumps) (Toro, 2001). The numerical treatment of the mixed hyperbolic-parabolic mathematical structure is split into both finite volume and finite difference discretization schemes. The conservative hyperbolic terms utilize a finite volume Riemann solver to allow for the discontinuous treatment of wave breaking and runup processes. The non-conservative parabolic terms, arising from the inclusion of dispersion, and source terms are treated with a finite difference discretization.

The wave generating mechanisms include internal source functions based on input wave spectra, initial free surface displacements, time series through the boundaries, as well as moving pressure distributions (for ship waves). The model can be easily integrated into other model packages, such as for storm surge calculations, since it can account for a non-uniform initial water level, as well as for spatial and temporal variations of input wave spectra. The source code is written in *C* and parallelized with *OpenMP*. The inclusion of a program interface built to operate in both Matlab and Octave with standard *gcc* compilers caters to user friendliness.

The model has completed the NTHMP benchmarks for inundation (Roeber and Cheung, 2012). In addition, a series of large-scale laboratory experiments was conducted at the O.H. Hinsdale Wave Research Laboratory of Oregon State University in 2007 and 2009 to provide validation datasets specifically designed for wave and bore propagation over fringing reefs (Roeber et al. 2010, Roeber & Cheung 2012). *BOSZ* was also validated with field data obtained from a reef system in Hawaii (Roeber & Cheung, 2012, Heitmann *et al*. 2014). In several studies, integrated quantities such as significant wave height and wave setup, were cross-validated with the spectral wave model SWAN (e.g., Li *et al*., 2014). Recently, a study on extreme typhoon waves over a fringing reef shows a quantitative comparison between *BOSZ* and the 3D RANS solver OpenFOAM (Roeber & Bricker, 2015, and Bricker & Roeber, 2015). In all cases, *BOSZ* agrees well with data and/or other established models for wave height, flow speed, runup/inundation, and secondary processes such as wave setup and circulation.

2   Model Equations

The modular structure of *BOSZ* caters to a range of extended Boussinesq-type equations with second-order optimization of linear frequency dispersion. Let ε and μ denote the nonlinear and dispersion parameters. Here, we present the governing equations based on Gobbi & Kirby (1999), who derived a set of higher-order nonlinear equations with accuracy up to $O(\varepsilon^2\mu^4)$. Truncating high-order nonlinearity and retaining terms up to $O(\varepsilon)$ and $O(\mu^2)$, we arrive at the continuity and momentum equations with second order linear dispersion properties as

$$\eta_t + \nabla\cdot\left[(h+\varepsilon\eta)\mathbf{u}\right]$$
$$+\nabla\cdot\left\{\mu^2(h+\varepsilon\eta)\left[\left(Ah-\frac{h}{2}\right)\left[\nabla h(G\nabla\cdot\mathbf{u})+\nabla(G\nabla h\cdot\mathbf{u})\right]+\left(\frac{h^2B}{2}-\frac{h^2}{6}\right)\nabla(G\nabla\cdot\mathbf{u})\right]\right\}=0 \tag{3}$$

$$\mathbf{u}_t+\nabla h+e(\mathbf{u}\cdot\nabla)\mathbf{u}$$
$$+m^2\left[z_{\partial M1}\left[\nabla h(G\nabla\cdot\mathbf{u})+\nabla(G\nabla h\cdot\mathbf{u})\right]+\frac{m^2}{2}\left[z_{\partial M2}\nabla(G\nabla\cdot\mathbf{u})\right]\right]_t + t = 0 \tag{4}$$

where $\mathbf{u} = (u,v)$ velocity vector, h = local water depth with respect to still water level, η = free surface elevation, $G = \boxed{}$, $z_{aM1} = Ah - h$, $z_{aM2} = Bh^2 - h^2$, and $\boxed{} = (\boxed{}, \boxed{})$ in the horizontal plane defined by the (x, y) coordinate system.

The variables A and B are used for optimization of nonlinearity and dispersion and are related to Nwogu's (1993) optimization parameter $\boxed{}$ through $B = \boxed{}$, and $A = B^{0.5}$. With $\boxed{} = -0.5208$, $A = 0.4792$ and $B = 0.2296$ the equations exhibit identical properties to Nwogu's (1993) equations, which handles dispersion with less than 5% error over $0<kh<5$ (k is wave number).

The equation structure allows for implementation of additional terms representing nonlinear dispersion, which is also included in the *BOSZ* code but is neither necessary nor considered for the current benchmarking tests.

The Boussinesq-type equations (1) and (2), which contain the nonlinear shallow water equations as subsets, can be written in terms of conserved variables. With a stationary bathymetry, the continuity equation can be readily expressed with the total water depth, $H = h + \eta$, as time dependent variable. In dimensional differential form, the subscripts x and y denote partial differentiation in the respective directions and the continuity equation becomes

$$h_t + (Hu)_x + (Hv)_y$$

$$+ \left[h \left(Ah - \frac{h}{2} \left[h_x G(u_x + v_y) + (G(h_x u + h_y v))_x \right] + h \left(\frac{h^2 B}{2} - \frac{h^2}{6} G(u_x + v_y) \right)_x \right) \right]_x$$

(5)

$$+ \left[h \left(Ah - \frac{h}{2} \left[h_y G(u_x + v_y) + (G(h_x u + h_y v))_y \right] + h \left(\frac{h^2 B}{2} - \frac{h^2}{6} G(u_x + v_y) \right)_y \right) \right]_y = 0$$

The momentum equations with conserved variables, Hu and Hv, arise from Eq. (2) after pre-multiplication with H in combination with the continuity equation (1), which is pre-multiplied by u and v respectively as

$$(Hu)_t + (Hu^2)_x + (Huv)_y + \frac{1}{2}g(h^2)_x + g(\eta h)_x + g\eta h_x$$

$$+ H \left[z_{aM1} \left[h_x G(u_x + v_y) + (G(h_x u + h_y v))_x \right]_t + \frac{1}{2} z_{aM2} \left\{ G(u_x + v_y) \right\}_{x,t} \right] + t_1 = 0$$

(6)

$$(Hv)_t + (Hv^2)_y + (Huv)_x + \frac{1}{2}g(h^2)_y + g(\eta h)_y + g\eta h_y$$

$$+ H \left[z_{aM1} \left[h_y G(u_x + v_y) + (G(h_x u + h_y v))_y \right]_t + \frac{1}{2} z_{aM2} \left\{ G(u_x + v_y) \right\}_{y,t} \right] + t_2 = 0$$

(7)

153

where g denotes acceleration due to gravity and ☐ and ☐ are frictional drag terms. The first row of Eqs. (3), (4), and (5), denotes the conservative hyperbolic nonlinear shallow-water part whereas the remaining terms contain sources, sinks, and non-conservative parabolic dispersive terms. The expansion of the surface gradients, i.e. ☐ (and similar in y-direction), facilitates the implementation of a moving boundary with preservation of the extended C-property (i.e. lake at rest with wet/dry boundaries).

Since depth-integrated equations describe overturning breaking waves or bores as flow discontinuities, the non-hydrostatic terms pose a challenge to the solution. A relation between momentum gradient and celerity in both directions is queried locally and momentarily in each time step

☐ (8)

to identify cells where dispersion effects are omitted.

It is important to note that the conserved form of the governing equations holds for sub and supercritical flow without additional treatment. Eq. (6) does not necessarily define the onset of a breaking wave and it is not strictly required to provide the correct height and speed of a breaking wave. Instead, it should be seen as a threshold, beyond which numerical instabilities might occur. This measure obviously is dependent on the grid spacing, and in many cases, breaking waves propagate freely without even triggering the threshold. This technique performs in a robust way for a variety of breaking waves and stationary hydraulic jumps.

The dissipative term in *BOSZ* arises from the bottom friction based on Manning's roughness as

$t_1 = gn^2 H^{-1/3} u \sqrt{u^2 + v^2}$, $t_2 = gn^2 H^{-1/3} v \sqrt{u^2 + v^2}$, where n is the Manning coefficient in [s/m$^{1/3}$].

The Manning's n is a parameter designed to account for the surface property of the terrain. It is not straightforward and recommended to represent turbulence with these coefficients. Therefore, the effects of large-scale roughness elements, which dimensions are of equal order of magnitude as the flow depth and which induce three-dimensional vortex structures, cannot be accounted for. A summary of best-practice techniques with respect to the appropriate selection of roughness coefficients can be found in Bricker *et al*. (2015). Optionally, a Smagorinsky subgrid closure model can be used for horizontal mixing. This option was not activated in any of the benchmark problems to better allow for evaluation of the fundamental structure in *BOSZ*.

3   Numerical Solution Method

The governing equations can be written in matrix form as

154

in which the vector $\mathbf{U} = [H, P, Q]^T$ contains the evolution variables, $\mathbf{F}$ and $\mathbf{G}$ are the flux vectors in x and y directions, and $\mathbf{S}$ is the source term. In detail the terms are

$$\mathbf{G} = \begin{bmatrix} Hv \\ Hvu \\ Hv^2 + \dfrac{1}{2}gh^2 + ghh \end{bmatrix}$$

(10)

where y_C denotes the dispersion terms of the continuity equation and y_P and y_Q represent the non-hydrostatic contributions in the momentum equations.

The vectors $\mathbf{F}$ and $\mathbf{G}$ are evaluated based on a finite volume formulation. This requires reconstruction of the variables to the cell interfaces and the solution of a Riemann problem at each interface in each time step. We utilize a two-dimensional 5th order polynomial reconstruction for low numerical dissipation based on the approach by Kim & Kim (2005) in combination with the HLLC approximate Riemann solver. This technique provides solutions for wet and/or dry cells and therefore accounts for moving boundaries in modeling wave runup and inundation. Since the higher-order polynomial reconstruction technique can result in spurious oscillations near the moving boundary, the reconstruction is reduced to 2nd order in the two wet cells adjacent to a dry cell. The dispersion terms in the source term, $\mathbf{S}$, are discretized using a 2nd order central difference technique based on the variables at the cell centroids.

The time integration in *BOSZ* is based on a 2nd or optionally 3rd or 4th order Runge-Kutta method with variables time step size for efficient and robust computation. The scheme is stable up to a Courant number of 0.5, which is the default value in *BOSZ*. BM 1 and 2 were computed with 2nd order accuracy in time, whereas BM5 used 4th order integration. The continuity equation can be explicitly solved and it directly provides the term H_t for the momentum equations in Eq. (8).
The evolution variables in the momentum equations contain information from both flux and dispersion. In the *x*-direction the evolution variable is

$$P = (Hu)_t + H\left\{ z_{aM1}\left[h_x G(u_{tx} + v_{ty}) + G_x(h_x u_t + h_y v_t) + G(h_x u_t + h_y v_t)_x \right] + \frac{1}{2}z_{aM2}\left\{ G(u_{tx} + v_{ty}) \right\} \right\}_x \quad (11)$$

The term $y_P = z_{aM1}\left[h_x G(u_x + v_y) + \left(G(h_x u + h_y v) \right)_x \right] + \frac{1}{2}z_{aM2}\left[G(u_x + v_y) \right]_x$ in Eq. (8) arises from the product rule of the conserved variable formulation.

As the flux and dispersion quantities are moved together in time, the flow speed has to be extracted at the end of each time step through the solution of a linear system of equation. Though Eq. (9) contains xy cross-derivatives, the systems of equations for the time-evolution of the variables Hu and Hv only depend on either the x or y components respectively. Therefore, the time derivative in the terms with mixed time and xy-space derivatives such as v_{txy}, for example, can be solved

independently through first-order upwinding based on the solutions from the current and previous time steps (David *et al.*, 2014). The two systems of equations are tri-diagonal with data dependency only in direction of the particular derivatives. This favors the use of standard solvers such as the Thomas algorithm with straightforward parallelization.

4   Benchmark Problem Comparisons

4.1 Benchmark Problem #1: Steady Flow over Submerged Obstacle

The *BOSZ* setup for BM 1 uses the original bathymetry provided in combination with the recommended water depth of 0.054 m. Both upstream and downstream boundaries use an open radiation boundary condition for long waves. The steady stream is initiated by slowly adding mass to the upstream boundary. The model picks up the discharge and adjusts the mass input by checking the computed flow speed near the boundary. Once the steady free stream has reached the pre-defined speed of 0.115 m/s, the mass input remains constant. Since friction balances the discharge, a small gradient in the free surface becomes apparent. The difference between the recommended water depth and the actual water depth of the steady stream is determined in a test run and then subtracted from the initial water depth. We tested several grid configurations between 0.01 m and 0.03 m in 0.005 m increments (with $\Delta x = \Delta y$). Regarding the frictional dissipation, a range of Manning's n coefficients between 0.01 and 0.025 s/m$^{1/3}$ in increments of 0.005 s/m$^{1/3}$ was tested. As requested, the model was also run with zero frictional drag to get a feeling for the dissipation of the numerical scheme.

We found that *BOSZ* is only marginally sensitive to the examined numerical meshes for this BM test and convergence is reached around $\Delta x = \Delta y = 0.02$ m. The results vary most significantly with friction. Among the tested Manning's n values, 0.02 s/m$^{1/3}$ resulted in the most reasonable agreement with the laboratory data. However, this "best match" is subjective and it was solely determined by qualitative judgment. In general, the vortex structure behind the cone does not evolve properly for $n < 0.01$ s/m$^{1/3}$. In fact, zero friction does not lead to converging and physically meaningful solutions as some small poorly defined vortices develop downstream of the cone but then get trapped in the vicinity of the lateral boundaries. This indicates that the internal diffusivity of the numerical scheme is not sufficient to generate the vortex instability as observed in the experiments and other diffusive or dissipative mechanisms are necessary. Since *BOSZ* uses the bottom friction for dissipation, starting from $n = 0.01$ s/m$^{1/3}$ the vortex street becomes more elaborate and a structured oscillatory pattern arises for $n = 0.015$-0.02 s/m$^{1/3}$. With increasing friction, the vortex strength decreases. A uniform grid spacing of 0.015 m in combination with a realistic friction coefficient of $n = 0.02$ s/m$^{1/3}$ provide reasonable agreement with the data for both amplitude and wavelength of the velocity oscillations. The model was not tuned with other particular configurations and hence the results do not necessarily represent an optimum scenario. It should be noted that dispersive effects indeed are important in this BM problem even though the initial setting appears to exhibit a fairly hydrostatic flow regime. With the flow moving over and around the submerged cone, nonlinear effects become important, which in turn are balanced by dispersion. Using the same input conditions, a purely hydrostatic solution mainly leads to a mismatch in wavelength compared to a solution from the dispersive governing equation. The lack of dispersion has a similar effect to using the full set of dispersive equations in combination with a larger roughness value or a coarser grid. The largest discrepancy between *BOSZ*'s results and the

156

laboratory data can be seen in the *u*-velocity at gauge 1, where the model underestimates the recorded data. This is similar to the solutions provided by other depth-integrated models.

Figure 34. Experimental data (dots) and numerical simulation (solid line, not shown) for a) U velocity component at time series location 1, b) V velocity component at time series location 1, c) U velocity component at time series location 2, and d) V velocity component at time series location 2.

4.2 Benchmark Problem #2: Tsunami Currents in Hilo Harbor

BM 2 considers tsunami transformation and induced currents in Hilo Bay. Since the provided bathymetry lacked accuracy along the shoreline, we substituted the topography from a high resolution NGDC data set. The bathymetry, reef structure and breakwater remained unmodified. The setup used the recommended Manning roughness of $n = 0.025$ s/m$^{1/3}$. A numerical model provided the input wave signal for the boundary condition. Consequently, we first validated *BOSZ* for its capability to correctly generate the input waveform in the domain. The bathymetry was set to constant 30 m deep and a mass source along the Northern boundary modulated the inflow volume according to the time series of the tsunami signal. The process is similar to the input in BM 1. The free surface elevation observed at the offshore control point agrees near perfectly with the input signal. The same input was then applied along the Northern boundary of the actual irregular bathymetry. Comparing the computed free surface time series at the control point with the input time series, discrepancies in amplitude become evident. Since the model successfully propagates an input waveform through a domain of uniform depth, it is believed that these

differences are due to reflections and nonlinear interactions of the input wave with the local bathymetry and breakwater. Also, we applied the input signal only along the northern boundary, whereas the original tsunami model, which is the source of the input time series, covered an area well beyond the BM bathymetry with waves approaching from all open ocean boundaries. These limitations should be taken into account for evaluating the model performance for this test.

The results show very small variations of the free surface with grid spacing (i.e., *BOSZ* provides converging waveforms even with a 20 m grid). The grid resolution has a more significant impact on the velocities measured at the two ADCP locations. However, given the constraints associated with the input wave conditions, it is difficult to judge which grid resolution provides the best basis for matching the ADCP data.

Figure 35. Measured data (dashed line) and numerical simulation (solid line) at the harbor tide gage (top), HA25 ADCP (middle), and HA26 ADCP (bottom).

Figure 36. Maximum predicted fluid speed during entire duration of the 10-m resolution simulation.

4.3 Benchmark Problem #5: Solitary Wave Propagation over a Complex Shelf

BM5 covers a solitary wave transforming over a shelf-reef relief model. For the results shown in Fig. 4 and 5, *BOSZ* uses a uniform grid of $\Delta x = \Delta y = 0.10$ m and a Manning's $n = 0.013$ s/m$^{1/3}$. A detailed description of the hydraulic processes including figures can be found in Roeber & Cheung (2012). A summary is provided here:

The solitary wave breaks at the apex of the reef flat at $t = 5.1$ sec and the resulting surge completely overtops the cone at $t = 6.6$ sec. The refracted waves from the two sides of the cone and the diffracted waves converge in the back at $t = 8.6$ sec. While the refracted waves continue to wrap around as trapped waves, the diffracted waves radiate from the back of the cone. During this process, the flux gradients in the x and y directions trigger the threshold to deactivate dispersion along the breaking wave front and the model is stable during this critical period of the computation. The diffracted wave on the leeside of the cone propagates up the slope reinforcing the refracted waves from the reef edge. The flow is partially reflected by the back wall of the wave basin and recedes on the beach slope over small imperfection in the concrete surface. The drawdown then generates a bore, which collides with the reflection from the wavemaker over the reef flat around $t = 17$ sec and part of which is trapped around the cone as shown in the panel at $t = 21.2$ sec. After

159

about 45 sec, small vortices are generated in the vicinity of the reef edge and are transported around the conical island. Fig 4 compares the computed and recorded surface elevations over 90 sec. The model reproduces the recorded surface elevations in front of the cone and the collapse of the bore behind the cone. As shown in Fig. 5, the model matches the cross- and longshore components of the velocity reasonably well. It should be noted that the velocities in the physical model were measured near the surface whereas *BOSZ* computes the vectors close to mid-depth.

Since most of the hydraulic processes are fairly hydrostatic, simulations with a coarser grid of up to $\Delta x = 0.20$ m still account for the main flow structure and provide very reasonable agreement with the laboratory data - especially along the bore front. Therefore it is not surprising that the dispersive processes are of secondary importance in this BM. In fact, even if dispersion was ignored over the entire domain past the moment of initial wave breaking, the agreement between model and data would be very close to what is shown in Fig 4 and 5. Variations in roughness can lead to significant changes in flow speed over the dry beach where the flow depth is small. The choice of the appropriate roughness coefficient is critical in this test. Generally, $n < 0.01$ m/s$^{1/3}$ leads to an overestimation of flow speed and volume during runup and subsequently to a small mismatch in amplitude and phase at the wave gauges during the drawdown stage. With $n > 0.02$ m/s$^{1/3}$ the volume of the upsurge and, consequently, the flow speed would be underestimated.

The overall agreement between the computed and recorded data demonstrates the validity of *BOSZ* in handling multiple hydraulic processes, transitions from hydrostatic to dispersion–dominated flows as well as a variety of wave breaking scenarios in the two-dimensional horizontal plane with a moving boundary.

Figure 37. Free surface elevation at the wave gauges for 90 min of computation. Blue line denotes results from *BOSZ*, black circles indicate data from laboratory experiment.

Figure 38. Flow speed at the ADV locations for 90 min of computation. Blue line denotes results from *BOSZ*, black circles indicate data from laboratory experiment. Note that the non-dimensionalization shows the flow speed in terms of the Froude number.

5   Conclusions

We have performed benchmark problems 1, 2, and 5 with the numerical model *BOSZ*. In all three tests, *BOSZ* computes flow velocities, vortex patterns, as well as runup and inundation with good accuracy. Benchmark problem 1 includes low Reynolds number flows with vortex structures sensitive to the surface roughness. *BOSZ* shows little grid diffusivity and hence responds adequately to realistic bottom friction values. Test 2 examines long period oscillations and vortex shedding over a real bathymetry at full scale. The model provides converging solutions for the three required grid spacings. Benchmark test 5 involves energetic breaking waves with overtopping, vortex formation and runup/sheet flow, where *BOSZ* provides stable and accurate solutions for free surface and velocities.

In general, *BOSZ* does not require case-specific tuning or adjustment and provides accurate and reasonable solutions for complex flow problems with detailed vortex structures. The only user-defined parameter is the Manning roughness coefficients, which should be set according to

162

recommended values for site-specific terrains or surface properties. The low internal grid diffusivity enables the *BOSZ* model to respond realistically to the predefined roughness values.

References

1. Bricker, J.D., Gibson, S., Takagi, H. and Imamura, F., "On the Need for Larger Manning's Roughness Coefficients in Depth-Integrated Tsunami Inundation Models", *Coastal Engineering Journal.* In press, (2015).

2. Bricker, J.D. and Roeber, V., "Mechanisms of Damage During Typhoon Haiyan: Storm Surge, Waves, and "Tsunami-like" Surf Beat". *Proceedings of the 36th IAHR World Congress*, The Hauge, Netherlands (2015).

3. David, C.G., Roeber, V., Goseberg, N., "Introducing a pressure term for ship-induced waves into a Boussinesq-type model". *Chinese‐ German Joint Symposium on Hydraulic and Ocean Engineering* (CGJOINT). Paper Nr. 96, Franzius Institute, Hanover, Germany (2014).

4. Gobbi, M.F., and Kirby, J.T., "Wave evolution over submerged sills: tests of a higher-order Boussinesq model". *Coastal Engineering*, **37**(1), 57-96 (1999).

5. Heitmann, T.W., V. Roeber, Cheung, K.F., "Near-shore currents in fringing reef environments". *Proceedings of the 34th International Conference on Coastal Engineering*. Seoul, Korea (2014).

6. Kim, K.H. and Kim, C., "Accurate, efficient and monotonic numerical methods for multi-dimensional compressible flows Part II: Multi-dimensional limiting process". *Journal of Computational Physics*, **208**, 570-615 (2005).

7. Li, N., Roeber, V., Y. Yamazaki, T.W. Heitmann, Y. Bai, K.F. Cheung, "Integration of coastal inundation modeling from storm tides to individual waves". *Ocean Modelling*, 83, 26-42 (2014).

8. Nwogu, O., "An alternative form of the Boussinesq equations for nearshore wave propagation". *Journal of Waterway, Port, Coastal, and Ocean Engineering*, **119**(6), 618-638 (1993).

9. Roeber, V., and Bricker, J.D., "Destructive tsunami-like wave generated by surf beat over coral reef during Typhoon Haiyan". *Nature Communications*, 6:7854doi: 10.1038/ncomms 8854.

10. Roeber, V., Cheung, K.F., "Boussinesq-type model for energetic breaking waves in fringing reef environments". *Coastal Engineering*, **70**(1), 1-20 (2012).

11. Roeber, V., Cheung, K.F. and Kobayashi, M.H., "Shock-capturing Boussinesq-type model for nearshore wave processes". *Coastal Engineering*, **57**(4), 407-423 (2010).

12. Toro, E.F., *Shock-capturing methods for free-surface shallow flows*. Wiley, New York, (2001).

NEOWAVE Benchmark Results

Yefei Bai, [a] Yoshiki Yamazaki, [a] Kwok Fai Cheung [a]

[a]University of Hawaii, School of Ocean and Earth Science and Technology, Department of Ocean and Resources Engineering, Holmes Hall 402, 2540 Dole Street, Honolulu, Hawaii, USA 96822

Abstract. NEOWAVE is a depth-integrated non-hydrostatic model with a shock-capturing scheme for modeling of long-wave propagation, breaking, and inundation. The code is being applied for mapping and modeling under NTHMP and research of megafault rupture and tsunami processes. Numerical dissipation, which is crucial for vortex generation, is derived primarily from upwind approximations of flux and advection in the finite difference solution. This report includes results from Benchmarks #1, #2, and #5 with each computed at three grid resolutions. The measurements from Benchmark #1 capture vortex formation and shedding. A sensitivity study shows an increase in the grid size leads to growth in flow speed and reduction in the oscillation period. The measurements from Benchmarks #2 and #5 do not reveal vorticity structures of the flow and their comparison with model results are less conclusive. The overall model results do show strong correlation between the grid resolution and the size and intensity of vortices.

Address all correspondence to: Kwok Fai Cheung, University of Hawaii, School of Ocean and Earth Science and Technology, Department of Ocean and Resources Engineering, Holmes Hall 402, 2540 Dole Street, Honolulu, Hawaii, USA 96822; Tel: +1 808-956-3485; Fax: +1 808-956-3498; E-mail: cheung@hawaii.edu

1   Model Background

NEOWAVE stands for Non-hydrostatic Evolution of Ocean Wave. The initial motivation of its development is to have a long-wave model that can describe hydraulic processes over steep slopes and their abrupt transition to insular shelves or reef flats in tropical island environments. The model builds on the nonlinear shallow-water equations with a vertical velocity term for flows over steep slopes and a shock-capturing scheme for bore formation and propagation (Yamazaki *et al*., 2009, 2011a). These model features were tested at the 2009 Inundation Science and Engineering Cooperative Workshop sponsored by the National Science Foundation. NEOWAVE reproduces the energetic breaking waves and hydraulic processes over complex reef systems in the Tsunami Wave Basin at Oregon State University. In addition, NEOWAVE has been validated against the benchmarks put forth by the National Tsunami Hazard Mitigation Program for use in tsunami inundation mapping (Yamazaki *et al*., 2012a). NTHMP member states or territories using NEOWAVE include Hawaii, American Samoa, Guam, Puerto Rico, and the Gulf coast.

The vertical velocity term in NEOWAVE facilitates modeling of tsunami generation from time-dependent seafloor displacement and accounts for dispersion at the source and in the far field. The near-field waveforms are intrinsically related to the coseismic deformation and propagate at much lower speed than rupture expansion and seismic waves. These attributes are effective in sensitivity analysis of rupture processes through a combination of geophysical and tsunami data. NEOWAVE has been used with finite-fault inversion methods to iteratively reconstruct the source mechanisms of the 2010 Mentawai, 2011 Tohoku, 2012 Haida Gwaii, 2013 Santa Cruz Islands, and the 2014 Iquique earthquakes (Bai *et al*., 2014; Lay *et al*., 2011, 2013a, 2013b; Yamazaki *et al*. 2011b; Yue *et al*., 2014). In most cases, the near-field tsunami records were used in iterative reconstruction of the earthquake source, and the far-field data from Hawaii was used for validation. For example,

Cheung *et al.* (2013) is able to reproduce tide gauge, DART, and ADCP measurements along the Hawaiian Islands using a finite-fault model of the 2011 Tohoku tsunami from Yamazaki *et al.* (2011b).

2   Model Equations

While NEOWAVE is written in spherical coordinates, it can be transformed into the Cartesian coordinate system (*x*, *y*) with simple modifications (Yamazaki *et al.* 2011a). Let *g* denote the gravitational acceleration; ρ the water density; and (τ_x, τ_y) the bottom friction. The evolution of the flow in time *t* and over varying depth *h* follows the continuity and momentum equations as

$$\frac{\partial \zeta}{\partial t} + \frac{\partial (UD)}{\partial x} + \frac{\partial (VD)}{\partial y} = 0 \tag{1}$$

$$\frac{\partial U}{\partial t} + U\frac{\partial U}{\partial x} + V\frac{\partial U}{\partial y} = -g\frac{\partial \zeta}{\partial x} - \frac{1}{2}\frac{1}{\rho}\frac{\partial q}{\partial x} - \frac{1}{2}\frac{q}{D\rho}\frac{\partial}{\partial x}(\zeta - h) - \tau_x \tag{2}$$

$$\frac{\partial V}{\partial t} + U\frac{\partial V}{\partial x} + V\frac{\partial V}{\partial y} = -g\frac{\partial \zeta}{\partial y} - \frac{1}{2}\frac{1}{\rho}\frac{\partial q}{\partial y} - \frac{1}{2}\frac{q}{D\rho}\frac{\partial}{\partial y}(\zeta - h) - \tau_y \tag{3}$$

$$\frac{\partial W}{\partial t} = \frac{q}{\rho D} \tag{4}$$

where (*U*, *V*, *W*) is the depth-averaged velocity, *q* is the non-hydrostatic pressure, ζ is the surface elevation, and $D = h + \zeta$ is the flow depth. If the non-hydrostatic pressure $q = 0$, the governing equations reduces to the nonlinear shallow-water equations.

The governing equations do not contain physical viscosity. The only physical dissipation arises from bottom friction, which is given by

$$\tau_x = n^2 \frac{g}{D^{1/3}} \frac{U\sqrt{U^2 + V^2}}{D} \tag{5}$$

$$\tau_y = n^2 \frac{g}{D^{1/3}} \frac{V\sqrt{U^2 + V^2}}{D} \tag{6}$$

where *n* is the Manning number. Dissipation due to wave breaking is modeled as flow discontinuities in the numerical solution.

3   Numerical Solution Method

The numerical solution is semi-implicit with second-order time integration. A finite difference scheme first integrates the continuity equation (1) for ζ and the hydrostatic components of the horizontal momentum equations (2) and (3) for *U* and *V*. A first-order upwind scheme approximates the flux terms through extrapolation the surface elevation, while taking on the average water depth from the two adjacent cells to avoid errors from depth extrapolation. The momentum-conserving advection scheme of Stelling and Duinmeijer (2003) is adapted with this upwind scheme to provide the advection speed that captures shock-related processes such as bores

or hydraulic jumps. The vertical momentum equation (4) is approximated by a linear distribution of W over the water column and expressed in terms of the kinematic boundary conditions at the free surface and seabed as

$$W_\zeta = \frac{\partial \zeta}{\partial t} + U \frac{\partial \zeta}{\partial x} + V \frac{\partial \zeta}{\partial y} \tag{7}$$

$$W_h = -U \frac{\partial h}{\partial x} - V \frac{\partial h}{\partial y} \tag{8}$$

The terms associated with the bottom and surface slopes in equations (7) and (8) are generally negligible, but may strongly influence local dispersion at shelf breaks and around large seamounts and canyons. The non-hydrostatic pressure q is then determined from the vertical momentum equation (4) via a Poisson equation. The last step is to update (U, V) from integration of the non-hydrostatic components of the momentum equations (2) and (3) and ζ from the continuity equation (1). The model allows up to five levels of two-way nested grids to describe multi-scale processes without external data transfer.

Energetic wave breaking introduces numerical instability through the dispersion terms. NEOWAVE tracks the flow speed every time step and switches off the non-hydrostatic terms at grid points reaching the breaking initiation criterion:

$$\sqrt{U^2 + V^2} > 0.5\sqrt{gD} \tag{9}$$

The governing equations locally and momentarily reduce to the nonlinear shallow-water equations, while the rest of the computational domain remains dispersive. The non-hydrostatic terms are reactivated when

$$\sqrt{U^2 + V^2} < 0.15\sqrt{gD} \tag{10}$$

This hybrid scheme allows the shock-capturing scheme to treat breaking waves as bores and account for energy dissipation without predefined mechanisms. The model keeps track of the interface between wet and dry cells at the beginning of each time step. A marker first detects retreat of the waterline by updating the wet-dry status of each cell based on the flow depth. The surface elevation from the wet cells along the interface is then extrapolated onto the dry region to determine any advancement of the waterline. The non-hydrostatic pressure is set to be zero at the wet cells along the wet-dry interface to conform with the solution scheme of the non-hydrostatic model. The moving waterline scheme is robust and non-dissipative as has been verified through comparison with analytical solutions (Yamazaki *et al.*, 2012a). The primary source of numerical dissipation comes from the first-order upwind approximation of the flux and advection speed. The implementation of the shock-capturing scheme improves the stability of flow advection. Numerical dissipation, which stems from the upwind approximation and shock-capturing scheme, varies with grid resolution and provides a mechanism for vortex generation and propagation.

4 Benchmark Problem Comparisons

4.1 Benchmark Problem #1: Steady Flow over Submerged Obstacle

The flume experiment, case SB4_02, of Lloyd and Stansby (1997) reveals a complex flow structure with periodic vortex shedding in the wake of a submerged conical island. We setup a two-dimensional domain in the horizontal plane for the flume and island and model the non-hydrostatic free-surface flow to reproduce key features captured in the experiment. The use of three sets of grid spacing, 1, 2, and 4 cm, enables a sensitivity analysis of the model results and an investigation of the numerical dissipation mechanism in relation to the physical process. The respective time steps of 0.0025, 0.005, and 0.01 s maintain the same Courant number for the three tests. The manning coefficient $n = 0.01$ s/m^3 as specified in the experiment is applied throughout the domain. A steady subcritical flow of 11.5 cm/s at the upstream boundary elevates the water surface along the flume. We lower the initial water level by 0.96 cm to reach the specified water depth of 5.4 cm around the island. An open boundary condition is implemented at the downstream end to allow exit of the flow. Output velocity vectors are compared with the laboratory measurements at two PTVs (Particle Tracking Velocimetry) and two-dimensional flow fields over a 5-min elapse time are analyzed for the vortex generation and shedding.

The PTV measurements at two locations immediate downstream of the island show periodic oscillations of the horizontal flow velocity due to vortex shedding. The measurements also show unsteady components that might be associated with vertical turbulent mixing over the apex of the conical island. NEOWAVE, which are based on depth-integrated governing equations, are not amenable to the three-dimensional turbulent flow structure, but is able to reproduce main features of the free-stream flow. Numerical viscosity is essential for modeling of recirculating flow under high shear stress. Our sensitivity study indicates an increase of the grid size leads to growth in the flow speed and reduction in the oscillating period. The time step size has little effect as long as the CFL condition is satisfied. Additional tests with the manning coefficient $n = 0$ show little effects on the results. The results from the 2-cm grid presented in figure 1 give the best match to the measurements. The stream-wise component u_1 is affected the most by the three-dimensional wake. The model can reproduce the short-period oscillations but not the amplitude nor the mean flow. The agreement is much better for the span-wise component v_1. The unsteady component abates at location 2, where the computed time series demonstrate reasonable agreement with the measurements in terms of velocity amplitude, period, and phase.

Figure 39. Experimental data (dots) and numerical simulation (solid line, not shown) for a) U velocity component at time series location 1, b) V velocity component at time series location 1, c) U velocity component at time series location 2, and d) V velocity component at time series location 2.

4.2 Benchmark Problem #2: Tsunami Currents in Hilo Harbor

The 2011 Tohoku tsunami propagated across the Hawaiian Islands causing no significant inundation, but triggered energetic and persistent surges over insular shelves, nearshore reefs, and harbors (Cheung *et al.*, 2013). Strong currents driven by the surges were recorded at the semi-enclosed Hilo Harbor by two NOAA ADCPs at 6-min sampling intervals that together with the local tidal gauge provide the benchmark dataset. We implemented NEOWAVE with five levels of nested grids to reconstruct the tsunami from the source to Hilo bay and provided the surface elevation time series over a 6-hour elapsed time at the designated control point to all participants as boundary conditions for their models. The resolution ranges from 2 acrmin across the Pacific to 10 m at Hilo Bay and the tide level was specified at 0.13 m below MSL around the time of tsunami arrival. As part of the benchmark study, we develop a separate north-south oriented rectangle grid over the 1/3-arcsec topography and bathymetry of the bay. The north boundary of the grid is in-line with the control point, where the incident waves are imposed. The remaining boundaries with the ocean are treated as impermeable walls and the moving waterline is enabled for inundation computation. It is worth noting that the benchmark setup favors inter-comparison of model results. Model validation with the measurements becomes secondary. The computational domain is

discretized into 1401 × 1029, 701 × 515, and 351 × 258 grids at 5, 10, and 20 m resolution for sensitivity analysis of numerical dissipation. Temporal resolution varies accordingly to maintain the same Courant number among the three tests. A Manning coefficient of $n = 0.025$ accounts for the bottom friction.

The input shallow-water waves propagate southward and enter the harbor through a wide entrance, where ADCP HA1125 was located in the middle. The waves refract and diffract around the breakwater-reef complex to reach HA1126 and the tide gauge. Reflected waves interact with subsequent arrivals to produce an intricate wave field in Hilo Bay. The three model grids give nearly the same surface elevations at the tide gauge and very similar velocity vectors at the two ADCPs. We illustrate the model results from the 10-m grid in the figure 2, where the u and v velocity components are positive in the east and north directions. In comparison to the tide gauge measurement, NEOWAVE reproduces the timing of the leading waves and slightly overestimates the amplitude. The computed flow speed at HA1125 is higher, but appears to be in phase with the measurements. The flow field around HA1126 is subject to vortices generated at the tip of the breakwater. It requires velocity measurements with a higher sampling rate for a meaningful comparison with numerical model results. Although negligible differences are found at the two ADCPs with respect to the three grids, velocity variations exist over areas with high vorticity concentration. Besides the breakwater, protruding headlands also generate vortices locally with high flow speed as seen in Figure 3. As grid size increases, the vortex strengthens and expands due to increasing numerical viscosity. The flow speed increases and the area with strong flow grows. When we correlate the computed flow field with physical processes, areas with strong vorticity should be explained cautiously since numerical effects are no longer negligible.

Figure 40. Measured data (dashed line) and numerical simulation (solid line) at the harbor tide gage (top), HA25 ADCP (middle), and HA26 ADCP (bottom).

Figure 41. Maximum predicted fluid speed during entire duration of the 10-m resolution simulation.

4.3 Benchmark Problem #5: Solitary Wave Propagation over a Complex Shelf

This benchmark deals with currents induced by breaking and overtopping of a solitary wave on a complex shelf. The laboratory experiment was conducted at the large wave basin in O.H. Hinsdale Wave Research Laboratory, Oregon State University. The setup involves a triangular shelf with steep drop-offs to a compound slope in front of a flat backshore area. A 0.45 m high cone is placed on the shelf to enhance vortex formation. An initial solitary wave of 0.39 m amplitude propagates over uniform water depth of 0.78 m before transforming over the shelf system and inundating the backshore area. Both the incident and receding waves wrap around the cone and the subsequent opposing flows provide a vortex generation mechanism. Nine wave gauges were placed over the shelf to measure surface elevation. Four of them, the first group, are deployed in the onshore-offshore direction along the centerline of the shelf system. Another four, the second group, are aligned parallel to the centerline with a 5 m offset. The remaining one has another 5 m offset from the gauge nearest to the waterline. Two ADVs (Acoustic-Doppler Velocimeters) are collocated with the front and back gauges and a third one has a 5-m offset to the right of the back gauge. We reproduce the experiment using 5, 10, and 25 cm grid spacing and the corresponding time steps of 0.002, 0.003, and 0.01 s. A Manning coefficient of $n = 0.012$ is applied to account for the subgrid roughness of the finished concrete surface. The experiment involves energetic wave breaking. The non-hydrostatic terms in NEOWAVE are switched off locally, when the computed speed exceeds

172

one half of the shallow-water celerity, to allow modeling of breaking waves as bores through the shock-capturing scheme.

Accurate modeling of the wave process is a prerequisite for studies of the vortex-induced currents. Figure 4 compares the measured surface elevations at the nine gauges with the model results from the three grids. The grid spacing only slightly modifies the bore speed and height with minimal effect on the overall time series. The model captures shoaling, refraction, and diffraction of the solitary wave and gives reasonable predictions on bore propagation at the gauges. Discrepancies occur at the two gauges immediately behind the island because of the model cannot capture the three-dimensional turbulent flow from overtopping of the island. The ADVs can record three-dimensional velocity vector at a single point. Given the depth-integrated governing equations of NEOWAVE, we only select the cross-shore and long-shore components (U, V) for comparison. We observed strong vortices symmetrical to the centerline behind the island in the numerical experiment. However, figure 5 shows the spatial resolution or numerical dissipation plays a minor role in the flow velocity. The flow at the three ADVs, which were placed along the centerline or away from the island, is not strongly affected by the vortices. Overall the cross-shore components are reasonably reproduced despite some mismatches in the phase. The weak long-shore signals recorded at the centerline are possibly introduced by offsets of instrument locations in the laboratory experiment. The model reproduces the dominant cross-shore flow reasonably well in contrast to the long-shore component, which is an order of magnitude smaller.

Figure 4. Surface elevation comparison between experimental data (black line) and modeling solutions across nine gesture gauges. The first and second group is outlined by dashed rectangle. Measured data (black line), 5-cm (red line), 10-cm (green line), and 20-cm (blue line).

Figure 5. Velocity component comparison between experimental data (black line) and modeling solutions at three ADVs. Measured data (black line), 5-cm (red line), 10-cm (green line), and 20-cm (blue line).

5   Conclusions

Numerical dissipation has strong influence on the flow field in the presence of vortices. This is illustrated by Benchmark #1, in which the grid size plays a significant role in vortex formation and shedding downstream of an obstacle. An increase in the grid size leads to growth in the flow speed and reduction in the oscillating period. The grid dependence is also evident in the computed flow field in Benchmark #2 especially over areas with high vorticity concentration. The model results at the ADCPs, however, are less sensitive to the grid size due to either the ADCP locations away from the main vorticity sources or the low sampling interval. In Benchmark #5, the model results show formation of vortices behind the island that might not be captured by the ADVs placed along the centerline and at a large offset. Hence the model results of the advection-dominated flow at the gauges are also not sensitive to the grid size.

NEOWAVE is able to reproduce the open channel flow in Benchmark #1 and the flux-dominant flows induced by the weakly dispersive, nonlinear shallow-water waves in Benchmarks #2 and #5.

Implementation of the shock capturing and hybrid schemes allows the model to approximate breaking waves as hydraulic jumps and bores with reasonable accuracy for transition between sub- and super-critical flows. Numerical viscosity from the upwind approximations of flux and advection in the finite difference solution facilitates formation of vortices along protruding boundaries and subsequent shedding comparable to observations. The grid spacing, which is a determining factor of the numerical viscosity, allows tuning of the model to match the physical vortical processes. However, we need to understand the relationships between physical and numerical viscosity as well as the resulting vortices to reliably model nearshore currents adjacent to protruding boundaries or underwater features.

References

1. Bai, Y., K. F. Cheung, Y. Yamazaki, T. Lay, and L. Ye (2014), Tsunami surges around the Hawaiian Islands from the 1 April 2014 North Chile Mw 8.1 earthquake, Geophys. Res. Lett., 41, 8512–8521, doi:10.1002/2014GL061686.

2. Cheung, K. F., Y. Bai, Y. Yamazaki (2013), Surges around the Hawaiian Islands from the 2011 Tohoku tsunami. J. Geophys. Res. Ocean, 118, 5703-5719.

3. Lay, T., C. J. Ammon, H. Kanamori, Y. Yamazaki, K. F. Cheung, and A. R. Hutko (2011), The 25 October 2010 Mentawai tsunami earthquake (Mw 7.8) and the tsunami hazard presented by shallow megathrust ruptures, Geophys. Res. Lett., 38, L06302, doi: 10.1029/ 2010GL046552.

4. Lay, T., L. Ye, H. Kanamori, Y. Yamazaki, K. F. Cheung, K. D. Koper, and K. Kwong (2013a), The October 28, 2012 Mw 7.8 Haida Gwaii underthrusting earthquake and tsunami: Slip partitioning along the Queen Charlotte Fault transpressional plate boundary, Earth Planet. Sci. Lett., 375, 57-70.

5. Lay, T., L. Ye, H. Kanamori, Y. Yamazaki, K. F. Cheung, and C. J. Ammon (2013b), The February 6, 2013 Mw8.0 Santa Cruz Islands earthquake and tsunami, Tectonophysics, 608, 1109–1121.

6. Lloyd, P.M., P.K. Stansby (1997), Shallow water flow around model conical island of small slope. II: Submerged, J. Hydraul. Eng., ASCE 123 (12), 1068-1077.

7. Stelling, G.S., S.P.A., Duinmeijer (2003), A staggered conservative scheme for every Froude number in rapidly varied shallow water flows, Int. J. Numer. Meth. Fl., 43(12), 1329-1354.

8. Yamazaki, Y., Z. Kowalik, K.F. Cheung (2009), Depth-integrated, non-hydrostatic model for wave breaking and runup, Int. J. Numer. Meth. Fl., 61(5), 473-497.

9. Yamazaki, Y., K.F. Cheung, Z. Kowalik (2011a), Depth-integrated, non-hydrostatic model with grid nesting for tsunami generation, propagation, and run-up, Int. J. Numer. Meth. Fl., 67(12), 2081-2107.

10. Yamazaki, Y., T. Lay, K.F. Cheung, H. Yue, H. Kanamori (2011b), Modeling near-field tsunami observations to improve finite-fault slip models for the 11 March 2011 Tohoku earthquake, Geophys. Res. Lett., 38, L00G15, doi: 10.1029/2011GL049130.

11. Yamazaki, Y., K. F. Cheung, Z. Kowalik, T. Lay, and G. Pawlak (2012b), Chapter 7. NEOWAVE, Proceedings and Results of the 2011 NTHMP Model Benchmarking Workshop, NOAA, Galveston, Tex.

12. Yue, H., T. Lay, L. Rivera, Y. Bai, Y. Yamazaki, K. F. Cheung, E. M. Hill, K. Sieh, W. Kongko, and A. Muhari (2014), Rupture process of the 2010 Mw 7.8 Mentawai tsunami earthquake from joint inversion of near-field hr-GPS and teleseismic body wave recordings constrained by tsunami observations, J. Geophys. Res. Solid Earth, 119, 5574–5593, doi:10.1002/ 2014JB011082.

TSUNAMI3D Benchmark Results

Alyssa Pampell-Manis,[a] Juan Horrillo[a]

[a]Texas A&M University at Galveston, Tsunami Research Group, Offshore and Coastal System Engineering, 200 Seawolf Parkway, Galveston,TX, 77553

Abstract. In order to help produce accurate and consistent maritime hazard products, according to the new FY13-17 National Tsunami Hazard Mitigation Program (NTHMP) Strategic Plan, this paper discusses the results of two benchmark problems to validate the numerical model TSUNAMI3D. The tests are designed to understand the relative importance of physical versus numerical dissipation and effects of spatial variability between different model resolutions on the flow structure and velocities and the evolution of features such as eddies. The numerical model TSUNAMI3D is a 3D Navier-Stokes (NS) model which is optimized for tsunami problems and solves transient fluid flow with free surface boundaries based on the volume of fluid (VOF) method. For the two benchmark problems, we use a first or second order method for the nonlinear terms as well as a bottom friction formulation based on the logarithmic law of the wall. Overall, for both problems, this model produces results in good agreement with the experimental and observational data, matching expected velocity magnitudes and periodicity as well as flow structure. The good results suggest that a 3D model is essential to capture some of the features of tsunami-induced currents, including vortex-shedding and currents in harbors.

Address all correspondence to: Juan Horrillo, Texas A&M University at Galveston, Tsunami Research Group,Offshore and Coastal System Engineering, 200 Seawolf Parkway, Galveston,TX, 77553; Tel: +1 409-740-4465; Fax: +1 409-741-7153; E-mail: horrillj@tamug.edu

1   Model Background

TSUNAMI3D is a 3D Navier-Stokes (NS) model which is optimized for tsunami problems and is based on the computational fluid dynamics (CFD) model originally developed at Los Alamos National Laboratory (LANL) during the 1970s, following early work by Hirt and Nichols (1981). It solves transient fluid flow with free surface boundaries based on the concept of the fractional volume of fluid (VOF) method using an Eulerian mesh of rectangular cells of variable size in all directions. The fluid equations solved are the finite difference approximation of the full NS equations in Cartesian coordinates and the incompressibility condition equation which results from the continuity equation when the density is constant. The basic mode of operation is for a single fluid phase having multiple free surfaces. However, TSUNAMI3D also can be used for calculations involving two fluid phases separated by a sharp or diffusive interface, for instance, water and landslide material. In either case, both fluids are considered incompressible and treated as Newtonian. Internal obstacles, e.g., topography, walls, etc., are defined by blocking out, fully or partially, any desired combination of cells in the domain.

TSUNAMI3D has led to very good agreement (Horrillo et al., 2013) with the standard provided by the National Tsunami Hazard Mitigation Program (NTHMP) for validation and verification of tsunami model inundation, report OAR-PMEL-135 (Synolakis et al., 2007). Results from validation and verification of the model can be also found in the NTHMP's Workshop Proceedings (NTHMP 2012) and Horrillo, et al. (2014). The interested reader is referred to Horrillo (2006) and Horrillo et al. (2013) for more detailed information about the 3D NS model.

2   Model Equations

The governing equations for TSUNAMI3D are the incompressibility condition of the continuity equation

$$\frac{\partial u}{\partial x} + \frac{\partial v}{\partial y} + \frac{\partial w}{\partial z} = 0$$

and the non-conservative equation of momentum given by:

$$\frac{\partial u_i}{\partial t} + u_j \frac{\partial u_i}{\partial x_j} = -\frac{1}{\rho}\left(\frac{\partial p}{\partial x_i} + \frac{\partial q}{\partial x_i}\right) + \frac{\partial}{\partial x_j}\left[\frac{\mu}{\rho}\left(\frac{\partial u_i}{\partial x_j} + \frac{\partial u_j}{\partial x_i}\right)\right] + g_i, \qquad i,j = 1,2,3$$

where $\boldsymbol{u} = [u(x,y,z,t), v(x,y,z,t), w(x,y,z,t)]$ are the velocity components along the coordinate axes $\boldsymbol{x} = [x,y,z]$ at time t. The kinematic viscosity μ/ρ, defined as the ratio of the molecular viscosity μ to the water density ρ, can be adjusted in the model for internal friction. The acceleration due to gravity is given by $\boldsymbol{g} = [0,0,-g]$. The total pressure $p_{tot} = p + q$ is divided into the hydrostatic pressure p and the dynamic or non-hydrostatic pressure q. The hydrostatic pressure is given by

$$p = \rho g(\eta - z)$$

such that $\partial p/\partial z = -\rho g$. Here, z is the elevation measured from the vertical datum to the cell center and η is the water free surface elevation, also measured from the vertical datum.

3   Numerical Solution Method

The fluid equations are solved using standard finite difference schemes. All variables are treated explicitly except for the non-hydrostatic pressure q which is solved for implicitly. The nonlinear terms in the momentum equations are solved using a first order upwind/downwind scheme or, alternatively, a second order conservative scheme which includes a flux limiter to maintain monotonicity of the velocities. Artificial viscosity in the model arises mainly from the truncation error of the scheme used for the nonlinear terms. The non-hydrostatic pressure q is calculated through the pressure Poisson equation by using the incomplete Cholesky conjugate gradient method to solve the resulting linear system of equations.

The free surface elevation η is traced using the simplified VOF method based on the scalar function F and the donor-acceptor algorithm of Hirt and Nichols (1981). The method is based on the so-called fraction function F, in which F is defined as the fraction of fluid in the control volume cell (namely, volume of a computational grid cell). F is a discontinuous function, its value varying from 0 to 1 depending of the fluid interface location. That is, when the cell is empty, the cell has no fluid inside and the value of F is zero; in contrast, when the cell is full, $F = 1$. When the fluid's interface is within the cell, $0 < F < 1$, which defines the location of the free surface. Integration

of individual cell fluxes determines the change in F within a cell, and thus, the change in sea level at the surface.

4   Benchmark Problem Comparisons

4.1 Benchmark Problem #1: Steady Flow over Submerged Obstacle

The computational domain used is 4.75m by 1.52m by 0.054m in the x, y, and z directions, respectively. Cell sizes are 0.01m in both x and y and 0.0027m in z. This results in a total of 2,056,824 computational cells. Estimated CPU time required was 20 hours per 100 seconds of simulation time using 8 CPUS. The inflow boundary condition is $u_{(west)} = 0.115$ ms^{-1} applied at the entire west domain boundary. The outflow boundary condition at the east of the domain is defined as

$$u_{(east)} = \eta \sqrt{\frac{g}{D}} + 0.115 \text{ ms}^{-1}$$

where $u_{(east)}$ is the outflow velocity including the contribution due to wave reflection out of the domain and D is the total water depth along the east wall boundary. A second order finite difference scheme is used for the nonlinear terms in the momentum equations for this problem. This is done in order to reduce numerical friction and improve accuracy in this relatively small grid size. However, near the free surface, when the second order method encounters two surface cells, a first order method is used. Bottom friction is implemented according to the logarithmic law of the wall for a hydraulically smooth flow, and friction is calculated automatically based on the shear velocity for the flow at the bottom of the domain, outside the laminar sublayer. This approach gives a maximum bottom friction factor similar to that determined by assuming shear velocity according to the methodology of turbulent diffusivity in a channel using a Manning coefficient of 0.01. The model results proved to be insensitive to changes in eddy viscosity less than 10^{-6} m^{2}s^{-1}.

Overall, we find quite good agreement between the experimental data and numerical model results in both velocity magnitude and period for both gage locations. The good agreement in period even with the presence of bottom friction is attributed to the higher order method used for the nonlinear terms; implementing a first order method resulted in a phase lag in all velocity measurements similar to that seen in the 3D model results in Lloyd and Stansby (1997). Some variability in the expected approximately 10 second period is seen especially in the v velocity component at gage 1, but this variability is not significant relative to that seen in the experimental data. The magnitude of the u velocity component at gage 1 is slightly less than the measured data, with the mean calculated to be 26% lower than that in the experiment, but this difference is about half of that seen in the results from the 3D model used in Lloyd and Stansby (1997). Spurious oscillations, seen particularly in the velocity field at gage 2, are a result of the second order method used for this problem, as well as possibly the change between second and first order methods near the free surface.

Figure 42. Experimental data (dots) and numerical simulation (solid line, not shown) for a) U velocity component at time series location 1, b) V velocity component at time series location 1, c) U velocity component at time series location 2, and d) V velocity component at time series location 2.

4.2 Benchmark Problem #2: Tsunami Currents in Hilo Harbor

The computational domain [in geographic coordinate system (Longitude/Latitude)] has been converted to Universal Transverse Mercator coordinate system (UTM). The approximate dimension of the computational domain is 6782m by 7113m by 33m in the x, y, and z directions, respectively. Cell sizes are 9.69m in x, 10.31m in y and 0.2-2m (variable) in the z direction. This results in a total of 702x692x47 = 22,831,848 computational cells. Estimated CPU time required was 120 hours for 6 hours of simulation time using 32 CPUS.

The boundary condition at the north side of the domain is given as a function of time; however, the inflow is combined with the outflow wave signals to radiate reflected waves traveling out as indicated in the following equation:

$$v_{(north)} = \eta_{(north)}(t)\sqrt{\frac{g}{D(t)}} + v_{(north-1)}$$

Here, $\eta_{(north)}(t)$ is the given sealevel (measured from the still water level) at the boundary at time t, $D(t)$ is the total water depth at time t, $v_{(north)}$ is the depth-averaged (column-wise) water particle velocities along the north wall boundary and $v_{(north-1)}$ is the corresponding depth-averaged particle velocities one cell away (south) from the north boundary. $v_{(north-1)}$ velocities bring the information of the outgoing waves (reflected waves) generated by the domain coastal/bathymetry morphology. The east wall boundary radiates out the out-going signal in a similar fashion as indicated below:

$$u_{(east)} = \eta_{(east-1)}\sqrt{\frac{g}{D}}$$

Bottom friction is implemented merely using the no-slip condition $(\partial \boldsymbol{u}/\partial z) \neq 0$ and the internal friction (effective eddy viscosity) has been set to $O(10^{-4})$ m^{2}s^{-1}.

Despite the use of a first order upwind/downwind treatment for the nonlinear terms in the momentum equations, we find again a good agreement between the data and model results; i.e., at the control point numerical gage, harbor tide gage, and the two ADCPs (HA1125 and HA1126). At the ADCP HA1126, a very good agreement is obtained for the first peak y-direction averaged velocity, indicating, perhaps, that 3D numerical model structure is important to reproduce well field velocities in harbors. Using a lower spatial resolution of 20m in x and y did not give any significant differences in results.

Figure 43. Measured data (dashed line) and numerical simulation (solid line) at the harbor tide gage (top), HA25 ADCP (middle), and HA26 ADCP (bottom).

Figure 44. Maximum predicted fluid speed during entire duration of the 10-m resolution simulation.

5   Conclusions

Overall, we find quite good agreement between the data and model results in both benchmark problems. In Benchmark Problem #1, good agreement in period and velocity magnitude is attributed to the higher order method used for the nonlinear terms; implementing a lower order method resulted in a phase lag in all velocity measurements, similar to that seen in the 3D model results in Lloyd and Stansby (1997). The magnitude of the u velocity component at gage 1 is slightly less than the measured data, but the difference is less than that obtained from the 3D model used in Lloyd and Stansby (1997). These results suggest the higher order method treatment of the nonlinear terms is essential to overcome the numerical/artificial viscosity for this scale of problem replicating an experimental setup. The good match in velocity period for all of the gages suggests that the 3D structure of the vortices produced by eddy shedding is important, and 3D models provide a unique capability to accurately capture the timing and evolution of such features.

In Benchmark Problem #2, despite the use of a first order upwind/downwind treatment for the nonlinear terms, we find again a good agreement between the data and model results. The lower order method is sufficient for this problem given the large domain and relatively large cell size. At the ADCP HA1126, a good agreement is obtained for the first peak y-direction averaged velocity, indicating, perhaps, that 3D model structure is important to reproduce well tsunami-induced field

velocities in harbors. In addition, while a simple no-slip condition was used to account for bottom friction in this problem, a second test is currently underway using the logarithmic law of the wall for a hydraulically smooth flow, similar to that used for Benchmark Problem #1. Initial results suggest the simulated velocities are much improved using this approach, though further investigation is needed to run the full problem simulation for confirmation. It is also worth noting that a higher resolution result for problem #2 was not possible due to the computational constraints of the 3D model for this size of domain; however, minimal difference was seen in the results using a lower resolution (20m) and those presented here for 10m resolution, so significant differences would not be expected for a higher resolution simulation.

6 Acknowledgments

References

1. Lloyd, P.M., and Stansby, P.K. (1997) "Shallow Water Flow around Model Conical Island of Small Slope. II: Submerged." Journal of Hydraulic Engineering, 123, 1068-1077.

2. Hirt, C. W., and B. D. Nichols (1981). Volume of fluid method for the dynamics of free boundaries, J. Comput. Phys., 39, 201–225.

3. NTHMP (2012). ''National Tsunami Hazard Mitigation Program. Proceedings and Results of the 2011 NTHMP Model Benchmarking Workshop''. NOAA-NTHMP, Boulder: U.S. Department of Commerce/NOAA/NTHMP; (NOAA Special Report), 436 pp.

4. Horrillo, J. (2006). Numerical Method for Tsunami calculations using Full /Navier–Stokes equations and the Volume of Fluid method. Ph.D. thesis. University of Fairbanks.

5. Horrillo, J., Wood A., Kim, G.-B., A. Parambath A., (2013). A simplified 3-D /Navier–Stokes numerical model for landslide tsunami: Application to the Gulf of Mexico. J. Geophys. Res. Oceans, 118, 6934–6950, doi:10.1002/2012JC008689.

6. Horrillo, J., Grilli, S.T., Nicolsky, D., Roeber, V. and Zhang J. (2014). Performance Benchmarking Tsunami Models for NTHMP's Inundation Mapping Activities. Pure Appl. Geophys. Published online: DOI 10.1007/s00024-014-0891-y

7. Synolakis, C.E., Bernard, E.N., Titov, V.V., Kanoglu, U., Gonzalez, F.I., (2007). OAR PMEL-135 Standards, criteria, and procedures for NOAA evaluation of tsunami numerical models. Technical Report NOAA Tech. Memo. OAR PMEL-135. NOAA/Pacific Marine Environmental Laboratory, Seattle, WA.

SCHISM Benchmark Results

Y. Joseph Zhang[a]

[a]Virginia Institute of Marine Science, College of William & Mary, Center for Coastal Resource Management, 1375 Greate Road, Gloucester Point, VA 23062-1346, USA

Abstract. We present the model results (SCHISM) obtained at the NTHMP tsunami current benchmark workshop held in February 2015. Our results from the first two benchmark tests show that the model is able to accurately capture the variability of the current field with a moderate computational cost. For the 1st test which is inherently 3D in nature, the model captures both the amplitude and phase of the velocity variation at all stations.

Address all correspondence to: Joseph Zhang, Virginia Institute of Marine Science, College of William & Mary, Center for Coastal Resource Management, 1375 Greate Road, Gloucester Point, VA 23062-1346, USA; Tel: +1 804-684-7466; Fax: +1 804-684-7179; E-mail: yjzhang@vims.edu

1 Model Background

SCHISM (Semi-implicit Cross-scale Hydroscience Integrated System Model; Zhang et al. submitted) is a derivative product of SELFE (Semi-implicit Eulerian-Lagrangian Finite Elements, Zhang and Baptista 2008a) and is a general purpose model for geophysical fluid dynamics grounded on *unstructured grids*. The model has been extensively benchmarked and applied to many real systems of the world, in the context of general circulation (Burla et al. 2010; Brovchenko et al. 2011; Zhang et al. 2015), tsunami inundation (Zhang et al. 2011), storm surge (Bertin et al., 2012), ecology (Rodrigues et al. 2009), sediment transport (Pinto et al. 2012), oil spill (Azevedo et al. 2014), and water quality studies. Previously the model has been validated with the inundation benchmark tests during the NTHMP workshop (NTHMP 2012). The SCHISM modeling system has been fully parallelized using domain decomposition and MPI to further boost efficiency. As an open-source community supported model, SCHISM currently has 160 registered user groups around the world; more information can be found at www.schism.wiki.

2 Model Equations

At its hydrodynamic core, SCHISM solves Reynolds-averaged Navier-Stokes equations in either hydrostatic or non-hydrostatic form. For tsunami related applications, we typically use the hydrostatic option with the following equations in 3D:

Momentum equation:
$$\frac{D\mathbf{u}}{Dt} = \frac{\partial}{\partial z}\left(\nu\,\frac{\partial \mathbf{u}}{\partial z}\right) - g\nabla\eta + \mathbf{F}, \tag{1}$$

Continuity equation:

$$\frac{\partial \eta}{\partial t} + \nabla \cdot \int_{-h}^{\eta} \mathbf{u}\,dz = 0, \tag{2}$$

$$\nabla \cdot \mathbf{u} + \frac{\partial w}{\partial z} = 0, \tag{3}$$

Transport equations:

187

$$\frac{\partial C}{\partial t} + \nabla \cdot (\mathbf{u}C) = \frac{\partial}{\partial z}\left(\kappa \frac{\partial C}{\partial z}\right) + F_h + Q, \tag{4}$$

where

∇	$\left(\dfrac{\partial}{\partial x}, \dfrac{\partial}{\partial y}\right)$
(x,y)	horizontal Cartesian coordinates
z	vertical coordinate, positive upward
t	time
$\eta(x,y,t)$	free-surface elevation
$h(x,y)$	bathymetric depth
$\mathbf{u}(x,y,z,t)$	horizontal velocity, with Cartesian components (u,v)
w	vertical velocity
F	other forcing terms in momentum (baroclinicity, horizontal viscosity, Coriolis, earth tidal

potential, atmospheric pressure, radiation stress)

g	acceleration of gravity, in [ms^{-2}]
C	tracer concentration (e.g., salinity, temperature)
ν	vertical eddy viscosity, in [m^{2}s^{-1}]
κ	vertical eddy diffusivity in [m^{2}s^{-1}]
F_h	horizontal diffusion
Q	mass source/sink

For tsunami applications, the transport equation (4) is usually omitted (assuming the water is of constant density), and we typically use 1 vertical layer in the vertical, i.e. the 2D depth-averaged version of SCHISM. However, this is not the case in Problem 1 below.

Eqs. (1-4) are completed by a turbulence closure (we use the generic length-scale model of Umlauf and Burchard 1993), and proper initial and boundary conditions for each differential equation. Of particular relevance to the current benchmark tests is the bottom friction formulation, for which we use the turbulent boundary layer (logarithmic profile) in the 3D part of the grid and Manning's formulation in 2D part of the grid. In other words, the flexibility of the coordinate systems inside SCHISM allows us to use mixed 1D/2D/3D grid in different parts of the domain. At the moment the effects of wave breaking are not modeled.

3   Numerical Solution Method

SCHISM admits very flexible use of grids in both horizontal and vertical dimensions. Mixed triangular and quadrangular grids can be used in the horizontal. A new type of hybrid coordinate system called LSC^2 (Localized Sigma Coordinate with Shaved Cell) was recently introduced and shown to significantly improve accuracy near steep bottom slopes (Zhang et al. 2015). Once the domain is discretized, Eqs. (1-2) are first solved *simultaneously* for the unknown elevation defined at each node, with a Galerkin Finite-Element Method (FEM) together with Eulerian-Lagrangian Method (ELM). A semi-implicit time evolution scheme is used so as to bypass the stringent CFL criterion (Zhang and Baptista 2008a). The horizontal velocity is then solved from Eq. (1) with a

FEM along each vertical direction at side centers of each element. The vertical velocity is obtained from Eq. (3) as a diagnostic variable at element centroids using a Finite Volume Method (FVM) for volume conservation over each prism. Finally, the transport equations are solved with a FVM (with a TVD scheme for advection) at prism centers. The combination of implicit treatment of gravity waves and pressure, ELM and unstructured grids has proved powerful in addressing problems that traverse many spatial scales, as large time steps can be used with high resolution.

The default options in the model result in 2nd-order accuracy in space and time, but higher-order ELM can lead to 4th-order accuracy for the momentum equation. Since the main source of the numerical dissipation in the model comes from the ELM part, the higher-order ELM helps to keep the numerical dissipation low. The model also includes wetting and drying as a natural part of its algorithm and the latter cannot be disabled (Zhang et al. 2011). For tsunami applications, a shoreline tracking algorithm at each time step (Zhang and Baptista 2008b) is able to accurately simulate the wetting and drying process.

4   Benchmark Problem Comparisons

4.1 Benchmark Problem #1: Steady Flow over Submerged Obstacle

We used the untuned bottom drag coefficient of C_D=0.006 as in Lloyd and Standby (1997). A uniform grid size of 1.2cm in both *x* and *y* directions was adopted in the horizontal plane, and 11 terrain-following σ levels was used in the vertical grid. The time step was set at 0.05s. Turbulence closure scheme of k-ε was used to calculate the eddy viscosity and diffusivity.

Figure 45. Experimental data (dots) and numerical simulation (solid line, not shown) for a) U velocity component at time series location 1, b) V velocity component at time series location 1, c) U velocity component at time series location 2, and d) V velocity component at time series location 2.

4.2 Benchmark Problem #2: Tsunami Currents in Hilo Harbor

Since one of the goals of this test is to look at the convergence of numerical results, we generated mostly uniform grids with resolution varying between 20m, 10m and 5m as stipulated. The 10-m and 5-m grids were generated by splitting each element of the 20m grid by 4 and 16. As an example, the 5m-resolution grid has 775677 nodes and 1547200 triangles. The open boundary is curved close to the control point so we can impose the boundary condition there more precisely. For this test, we used only 1 vertical layer and the standard choice of Manning's n=0.025. With a time step of 1.5s, the model finished the 6-hour simulation in 36 minutes on 100 CPUs (Intel Xeon cluster).

Figure 46. Measured data (dashed line) and numerical simulation (solid line) at the harbor tide gage (top), HA25 ADCP (middle), and HA26 ADCP (bottom).

Figure 47. Maximum predicted fluid speed during entire duration of the 10-m resolution simulation.

5   Conclusions

We showed that SCHISM model is able to accurately capture current variability in both lab and field cases, whether these cases are 2D or 3D in nature. The results are also consistent with those from other benchmarks and field applications published elsewhere, including tides, surges and wave-current interactions. Therefore we believe the model can be effectively used to study multi-hazard problems.

6   Acknowledgments

192

References

1. Azevedo, A., Oliveira, A., Fortunato, A.B., Zhang, Y. and Baptista, A.M. (2014) A cross-scale numerical modeling system for management support of oil spill accidents, Marine Pollution Bulletin, 80, 132-147.

2. Bertin, X., Bruneau, N., Breilh, J.-F., Fortunato, A.B. and Karpytchev, M. (2012) Importance of wave age and resonance in storm surges: The case Xynthia, Bay of Biscay, Ocean Modelling, 42(0), 16-30.

3. Burla, M., Baptista, A.M., Zhang, Y. and Frolov, S. (2010) Seasonal and interannual variability of the Columbia River plume: A perspective enabled by multiyear simulation databases, J. Geophys. Res., 115, C00B16.

4. Brovchenko I., Maderich, V. and Terletska, K. (2011) Numerical simulations of 3D structure of currents in the region of deep canyons on the east coast of the Black Sea. International Journal for Computational Civil and Structural Engineering , 7 (2): 47-53.

5. Lloyd, P.M., Stansby, P.K., 1997. Shallow water flow around model conical island of small slope. II: Submerged. Journal of Hydraulic Engineering, ASCE 123 (12), 1068-1077.

6. NTHMP (2012) Proceedings and results of the 2011 NTHMP model benchmarking workshop. Boulder: US Depart. of Commerce/NOAA/NTHMP, NOAA Special Report 436p.

7. Rodrigues M., Oliveira, A., Queiroga, H., Fortunato, A.B. and Zhang,m Y. (2009) Three-dimensional modeling of the lower trophic levels in the Ria de Aveiro (Portugal), Ecological Modelling, 220(9-10),1274-1290.

8. Umlauf, L. and Burchard, H. (2003) A generic length-scale equation for geophysical turbulence models. J. Mar. Res., 6, 235-265.Zhang, Y., and Baptista, A.M. (2008a) SELFE: A semi-implicit Eulerian–Lagrangian finite-element model for cross-scale ocean circulation, Ocean Modelling, 21(3–4), 71-96.

9. Zhang, Y., and Baptista, A.M. (2008b) An efficient and robust tsunami model on unstructured grids. Part I: inundation benchmarks, Pure and Applied Geophysics, 165(11), 2229-2248.

10. Zhang, Y., Witter, R.C. and Priest, G.R. (2011) Tsunami–tide interaction in 1964 Prince William Sound tsunami, Ocean Modelling, 40(3–4), 246-259.

11. Zhang, Y., Ateljevich, E., Yu, H-S., Wu, C-H., and Yu, J.C.S. (2015) A new vertical coordinate system for a 3D unstructured-grid model, Ocean Modelling, 85, 16-31.

12. Zhang, Y., Ye, F., Stanev, E.V., and Grashorn, S. (submitted), Seamless cross-scale modelling with SCHISM, Ocean Modelling.